WESTERN SYDNEY
UNIVERSITY

Synthesis of Amino Acid-Derived Ligands and Investigation of their Metal Binding Properties and Biological Applications

David J. Western

Master of Research Thesis 2018

Presented to Western Sydney University in Fulfilment of the Requirements for the Degree of Master of Research

Supervisory Panel: Dr Feng Li and Dr Christopher E. Jones

Forward

The following dissertation is written by David James Western from Western Sydney University (WSU) as a part of the WSU Master of Research program. The Master of Research program extends to one year and nine months with the intent of one year of coursework followed by a nine-month period of laboratory work and thesis writing. This thesis project is new to both the Feng Li and Christopher Jones groups and has been written here in the style of ‘thesis by publication’.

Acknowledgements

Firstly, I would like to thank my supervisors Dr Feng Li and Dr Christopher Jones for all their support, patience and commitment towards myself, this project and the development of this thesis report. Special mention to Daniel Fanna to whom has been an industrious and crucial mentor to me over the last two years and taught me much of all I know in regards to this project.

Special thanks to the Feng Li group including Daniel 'Dan Fan' Fanna, Kyle 'Kylie' Howard-Smith, Alexander 'Sandman' Craze, Matthew 'One pot' Wallis, Xavier 'Fossil' Fuhrer and Adrian 'Scooter' Colussi for their acceptance, friendship and (lack of) knowledge over the past few years. All of who have in some way contributed to this thesis report.

Thank you to the Christopher Jones group, notably Katerina Christofides and Resmi Menon of who have taught me a plethora about cellular biology and assisted me with cell culturing and fluorescent microscopy.

I would like to personally thank Dr Richard Wuhrer of the Advanced Materials Characterisation Facility (AMCF), Dr Laurel George (AMCF), Dr Meena Mikhael (MS Facility) Dr Mohan Bhadbhade (UNSW), Dr Christopher Marjo (UNSW) and Dr Scott Willis (NMR Facility) for their time in training and allowing me access to the various instruments I used throughout this degree. I would also like to thank Assoc. Prof Jack Clegg (UQ) and the Australian Synchrotron for allowing me to train and use the MX1 beamline.

Furthermore, I would like to acknowledge Western Sydney University, University of New South Wales, University of Queensland and the Australian Synchrotron. Special mention to Western Sydney University where I have conducted both my undergraduate and postgraduate degrees. This research was supported by the Western Sydney University Master of Research stipend.

Last but not least, a special thank you to both the Western family and my lovely partner Annabel Newman. All of whom have all been very tolerant to me in kindness and love throughout the stress that is writing a thesis. Well now I'm set free!.. For now…

Statement of Authenticity

I declare that this thesis report is conducted by myself, David James Western. All other contributors have either been includes as co-authors or have been acknowledged within this report and lists of references have been sourced. This work has not been submitted for any other degree or diploma at any other institution other than where acknowledged.

Publication and Conference Presentations

Conference Presentations

David J. Western, Christopher E. Jones and Feng Li. (**2018**). The 10th Annual International Symposium on Nano & Supramolecular Chemistry (ISNSC), July, Dresden, Germany.

David J. Western, Christopher E. Jones and Feng Li. (**2018**). Royal Australian Chemical Institute (RACI) NSW Inorganic Symposium, November, Sydney, Australia.

Manuscripts in this Thesis

David J. Western, Alexander R. Craze, Mohan M. Bhadbhade, Christopher E. Marjo Christopher E. Jones and Feng Li. *L-Tryptophan-Derived, Water-Soluble Schiff Base as a Blue-Shift Fluorescent Sensor for Detecting Al^{3+} in Aqueous Solutions and Intracellular Environments*. (Manuscript in preparation)

David J. Western, Adrian Colussi, Christopher E. Jones and Feng Li. *The Metal Binding and Anticancer Properties of Lanthanides upon Complexation of a New Schiff Base Ligand*. (Manuscript in preparation)

David J. Western, Christopher E. Jones and Feng Li. *A Selective 'Turn-on' Fluorescent Sensor for Detecting Al^{3+} in Aqueous Solutions and Intracellular Environments*. (Manuscript in preparation)

Table of Abbreviations

Aβ	Amyloid beta
AD	Alzheimer's Disease
CD	Circular Dichroism
CFSE	Crystal Field Stabilisation Energy
ctDNA	Calf Thymus Deoxyribose Nucleic Acid
ctDNA-EB	Calf Thymus Deoxyribose Nucleic Acid – Ethidium Bromide
DMEM	Dulbecco's Modified Eagle Medium
DMSO	Dimethyl Sulfoxide
DNA	Deoxyribose Nucleic Acid
EB	Ethidium Bromide
EC	Effective Concentration
ESI-HRMS	Electrospray Ionisation - High Resolution Mass Spectrometry
FBS	Fetal Bovine Serum
FRET	Förster Resonance Energy Transfer
FT-IR	Fourier Transform - Infrared
GSH	Glutathione
GSSG	Glutathione disulphide
HOMO	Highest Occupied Molecular Orbital
HSAB	Hard-Soft Acid-Base
LoD	Limit of Detection
LoQ	Limit of Quantification
LUMO	Lowest Unoccupied Molecular Orbital
MRI	Magnetic Resonance Imaging
MT	Metallothionein
MTT	3-(4,5-dimethylthiazol-2-yl)-2,5-diphenyltetrazolium bromide
NADH	Nicotinamide Adenine Dinucleotide
NMR	Nuclear Magnetic Resonance

PBS	Phosphate Buffered Saline
PET	Photo-induced Electron Transfer
P-XRD	Powder - X-ray Diffraction
ROS	Reactive Oxygen Species
RPMI	Rosewell Park Memorial Institute
rt	Room Temperature
SC-XRD	Single Crystal - X-ray Diffraction
SOD	Superoxide Dismutase
STA	Simultaneous Thermal Analysis
STD	Standard Deviation
UV	Ultra-violet
UV-vis	Ultra-violet - visible
WSU	Western Sydney University

Abstract

In this thesis, two different potential fluorescent probes for metal ions and four potential anticancer drugs have been designed, synthesised, characterised and studied for their metal binding properties and biological applications.

This report aims to design and synthesise amino acid-derived ligands as potential metal ion sensors in biological and aqueous systems. Metal ions play many pivotal roles in biological systems such as catalysing biochemical reactions and creating action potentials allowing for the movement of organisms. Dysfunction of such metals can contribute to the development of diseases such as Alzheimer's disease (AD) and Wilson's disease. As a result, the biological roles of metal ions are of great intrigue to many scientists in multiple fields. These researchers depend upon the development of more ideal fluorescent sensors for metal ions to conduct their investigations. Unfortunately, current fluorescent probes for metal ions have limitations such as poor selectivity to their analyte, weak fluorescence intensity, and are often unsuitable for biological application due to poor water solubility, and high cytotoxicity. Therefore, the development of new probes is important to enhance the knowledge of metal ions in biology and medicine.

The fluorescent sensors synthesised in this thesis report that undergo cell viability assays with low effective concentration (EC) values are declared inappropriate for biological metal sensing. Their high cytotoxicity is therefore explored as potential anticancer agents when bound to lanthanides. Cancer constitutes to the top three of the total world's deaths. Platinum-based anticancer drugs have been the focal point of many chemotherapies used to treat cancer-related illnesses, however, are limited with intrinsic resistance and have negative side-effects due to a lack of cell selectivity. Other metal-based therapies, such as lanthanides-based therapies, have come of intrigue as potential substitutes for platinum-based drugs due to their unique properties. Despite the potential of lanthanide complexes as alternative anticancer therapies, this area of research has not received much attention.

Contents

List of Figures

List of Tables

Chapter 1 - Introduction

1.1 Supramolecular Chemistry

Jean-Marie Lehn, a joint 1987 Nobel Prize winner in chemistry with Donald J. Cram and Charles J. Pederson, for their 'development and use of molecules with structure-specific interactions of high selectivity', defined supramolecular chemistry as the 'chemistry of molecular assemblies and intermolecular bonds'. More colloquially supramolecular chemistry is frequently described as 'chemistry, beyond the molecule'.[1] This field of chemistry is predominately concerned with the study of host-guest interactions between molecules. This is where a 'host' molecule encapsulates a 'guest' molecule or ion, forming a more complex 'super' molecule, hence the term 'supramolecular chemistry'.[1-3] These host-guest interactions can occur synthetically, for example with some complexes of crown ethers. Conversely, many structures can spontaneously assemble into more distinctive architectures such as helicates and coordination cages. These naturally forming larger, more complex assemblies are more thermodynamically favourable than basic host-guest interactions. These complicated structures have been observed in biology notably in the double helix structure of deoxyribonucleic acid (DNA), protein folding and aggregation, as well as micelle and phospholipid bilayer formations.[4-6] This process by which molecules spontaneously assemble into complex three-dimensional structures is referred to as 'self-assembly'.[7,8] In supramolecular chemistry, the assemblies of such molecules are frequently held together by weak intermolecular bond formations including hydrogen bonding, hydrophobic forces, π-π stacking and Van der Waals forces.[1,2,9] In metallo-supramolecular chemistry, a branch of supramolecular chemistry, these molecules are held together by not just intermolecular forces but also, coordinate covalent bonds. Coordinate covalent bonds exist where a metal ion acts as a Lewis acid and a donor atom acts as a Lewis base, donating two electrons to its corresponding Lewis acid to form coordination bonds.[10]

Due to its interdisciplinary nature, supramolecular chemistry is prevalently studied in multiple fields of science such as chemistry, physics, biology, biochemistry material and natural science. Within the last few decades, supramolecular chemistry has provided many developments and supramolecular assemblies have incorporated much interest to scientists in

many different fields for their magnetic, electrochemical, optical, medical and chemosensory properties.[4,11,12]

1.1.1 Metallo-Supramolecular Chemistry

Metallo-supramolecular chemistry involves the host-guest interaction between an organic ligand and a metal ion. As previously mentioned, this is where an inorganic metal ion acts as a Lewis acid and donor atom(s) from the organic compound act as a Lewis base donating two electrons to the Lewis acid in a coordinate covalent bond.[10] Therefore, the organic molecule is coined as the 'host' molecule and the metal ion as the 'guest' molecule. The result is a supramolecular assembly formed from ligand and metal with a variety of different stoichiometry and coordinate geometries depending on molecules involved, the states of the molecules, as well as other reaction conditions. These supramolecular assemblies may be simple in structure, however, can result in the formation of more complicated macromolecules such as coordination cages and metal helicates resulting in a variety of applications and enhancing the understanding of multiple fields.[13,14]

1.1.1.1 Hard-Soft Acid-base (HSAB) Theory

Supramolecular molecules are carefully designed and synthesised for specific purposes. It is therefore essential to consider multiple different basic inorganic chemistry concepts including the hard-soft acid-base (HSAB) theory. The HSAB theory simply states that a hard Lewis acid prefers to coordinate with a hard Lewis base. Conversely a soft Lewis acid prefers a soft Lewis base. The terms 'hard' and soft' refer to the polarisability of the metal ion and ligand. Hard acids are metals with a high charge density and are therefore weakly polarisable and so prefer to coordinate to weakly polarisable bases. Hard acids typically consist of a multivalent charge as this increases charge density. Monovalent metals are often hard acids if they exhibit a small atomic radius which also increases charge density. Soft metals however, are highly polarisable metals with a low charge density. They are typically monovalent and exhibit large atomic radii. Soft acids prefer to coordinate to soft bases as soft bases too are typically highly polarisable.[15-18] Table 1.1 lists a range of some hard and soft, Lewis acids and bases including intermediates which are borderline hard or soft.

Table 1.1 Examples of some common hard, soft and intermediate Lewis acid and bases.[18,19]

	Lewis Acid	**Lewis Base**
Hard	Li^+, Na^+, Mg^{2+}, Al^{3+}, K^+, Ca^{2+}, Cr^{3+}, Mn^{2+}, Fe^{3+}, Co^{3+}, Zn^{2+}	F^-, Cl^-, H_2O, ROH, NH_3, RNH_2, $[CO_3]^{2-}$, $[NO_3]^-$, $[PO_4]^{3-}$, $[SO_4]^{2-}$, $[ClO_4]^-$
Intermediate	Fe^{2+}, Co^{2+}, Ni^{2+}, Cu^{2+}, Pb^{2+}	Br^-, $[NO_2]^-$, $[SCN]^-$, $[SO_3]^{2-}$
Soft	Cu^+, Pd^{2+} Ag^+, Cd^{2+}, Pt^{2+} Au^+, Hg^{2+}	H^-, I^-, RSH, R_2S, $[CN]^-$

The HSAB theory is generally a rule of thumb as there are many documented cases of hard acids coordinating to soft bases and vice versa. This is because other factors affect the bond strength between donor and acceptor atoms including atomic size, charge, electronegativity and orbital overlap.[18] Generally, when a hard acid is coordinated to a hard base and soft acid to a soft base, metallic complexes have a tendency to exhibit greater stability. Therefore, HSAB theory is frequently considered by supramolecular chemists when designing ligands for their specific applications.

1.1.1.2 Irving-William's Series

The Irving-William's series explains the binding stability of divalent *d*-block metals from manganese to zinc. In 1953 Harry Irving and Robert Williams investigated the stability of divalent *d*-block metals where they concluded that stability increase across the periodic table from manganese until copper where stability peaks. Irving and William's then proposed the following series:

$$Mn^{2+} < Fe^{2+} < Co^{2+} < Ni^{2+} < Cu^{2+} >> Zn^{2+}$$

From manganese to zinc, the atomic radii decreases resulting in an enhancement of stability explaining the increased stability for *d*-block metals from left to right of the periodic table. Crystal field stabilisation energy (CFSE) increases from manganese and peaks at nickel and so, therefore, it would be predicted that nickel would form the most stable complexes of the six different divalent *d*-block metals. However, as octahedral Cu^{2+} complexes exhibit Jahn-Teller distortion, the stability of octahedral Cu^{2+} is greater than that of Ni^{2+}, explaining

the results found by Irving and Williams.[18-20]

1.2 Metals in Biology

Metal biochemistry plays pivotal roles to the health and function of living organisms and ecosystems. Inorganic chemistry has enhanced a greater understanding and development of biochemical and medicinal practices. Metals in biological systems have been of great interest to scientists in multiple fields and methods that contribute to greater understandings of the roles metals play in biology are sought. Although metal ions are essential for regular function, imbalances, dysregulation and environmental changes (both micro and macro) can alter the function of such metals potentially leading to toxicity. Metals are found in every cell. It has been found that as many as a third of all proteins and half of all enzymes in the human proteome require metals for catalytic function and/or to maintain their structures.[21,22]. There are 22 essential elements for life, 10 of which are metals. This, however, includes chromium which is often debated as to whether it is an essential element to life (Fig. 1.1).[23,24]

H																	He
Li	Be											B	C	N	O	F	Ne
Na	Mg											Al	Si	P	S	Cl	Ar
K	Ca	Sc	Ti	V	Cr	Mn	Fe	Co	Ni	Cu	Zn	Ga	Ge	As	Se	Br	Kr
Rb	Sr	Y	Zr	Nb	Mo	Tc	Ru	Rh	Pd	Ag	Cd	In	Sn	Sb	Te	I	Xe
Cs	Ba	Ln*	Hf	Ta	W	Re	Os	Ir	Pt	Au	Hg	Tl	Pb	Bi	Po	At	Rn
Fr	Ra	Ac*															

Figure 1.1 Periodic table indicating the biologically essential elements. Essential elements for most forms of life are shown in red with the exception of chromium (Cr), which is shown in yellow. Essential elements that are restricted for some forms of life are shown in amber. Not shown are the *f*-block elements: lanthanides and actinides (asterisk after lanthanum (La) and actinium (Ac)).[23, 24]

Calcium, sodium, potassium and magnesium are metals coined as macrominerals. They exhibit weak to intermediate binding affinities to biological ligands such as peptides and proteins, however, are highly mobile and perform a wide range of different biological functions such as behaving as charge carriers and are responsible for generating movement as well as sensation from external stimuli. An excess of such metals can result in cells to become hypertonic due to osmotic pressure and can develop into diseases such as hypernatremia and hyperkalaemia which results in cardiovascular diseases and potential death.[23,25,26] Elements such as manganese, iron, copper, zinc and molybdenum are scarcely abundant and yet are essential elements. They typically have strong binding affinities for biological ligands; however, have lower mobility than the macrominerals. They perform many vital biological roles such as acting as Lewis acids and redox catalysts in enzymes and essential vitamins. Dysregulation of metals such as iron, copper and zinc has been closely linked to neurological disorders such as AD.[23,26,27] There are other metals which play minor, non-essential roles in biological functions. Most of these metals are innocuous in trace amounts whilst some can be excreted naturally. Heavy metal poisoning often results from generally non-prevalent minerals such as gold and silver accumulating in vital organs such as the liver with no method of renal excretion, potentially resulting in organ failure.[28] Other heavy metals such as mercury can cause severe neurodegeneration when coordinated to organic biomolecules allowing for diffusion across the blood-brain barier.[29] Metals such as cadmium can mimic and competitively inhibit the functions of essential elements such as calcium due to having comparably similar atomic size and charge. This has been associated with such diseases as osteomalacia and osteoporosis.[30] Metals such as aluminium do not account for a significant portion of biological elements, however, exist in a high abundance of the Earth's crust. Minor alterations to pH or mismanagements of ecosystems can result in disastrous effects on wildlife either directly or indirectly due to biomagnification.[31,32]

Aluminium is the most abundant metal element in the lithosphere accounting to 8.3% of the total mass in the Earth's crust and is the ninth most abundant metal found in humans.[33,34] Its cytotoxicity towards organisms is of intrigue to scientists in multiple disciplines. Aluminium has a wide range of applications commonly used in households around the world for cookware, foil, antiperspirants, building equipment, pharmaceutical drugs such as antacids and is even found at high concentrations in tea. This accounts to a great exposure of the metal to both the community and environment.[35-37] According to the Government of Western Australian, Department of Agriculture and Food, just 2-5 ppm

aluminium is toxic to the roots of sensitive plants and greater than 5 ppm is toxic to tolerant species. Acidic soils and waterways can develop within regions of close proximity to industrial and mining sites due to acid rain formation. In acidic environments and due to the oxyphilic nature of aluminium, aluminium is easily oxidised to aluminium ions where it is readily soluble in water, encouraging naturally occurring aluminium oxides to readily be absorbed into soils and waterways. This is a major issue for the ecosystem as high concentrations of aluminium is toxic to plants, fish, algae and other aquatic organisms.[31,38,39] Much research has indicated that aluminium plays a major role in the development of neurodegenerative diseases such as AD.[40] There are counterarguments for this claim of aluminium causing AD, however, the debate is still ongoing.[41,42] As a result, there is currently much medical research investigating the potential biological and medical roles aluminium plays and therefore the development of new aluminium sensors is of great importance to the enhancement of research such as the aluminium and AD debate.[43]

1.2.1 Alzheimer's Disease and the 'Metal Hypotheses'

AD is a complex, multifaceted neurological disorder and is the most common cause of dementia in the western world. According to Dementia Australia, it is estimated that in 2018 there are 436, 366 people in Australia living with AD. Due to an aging population, this is expected to more than double in the next fifty years. AD is also the second leading cause of death in Australia accounting for 5.4% of all deaths in males and 10.6% of deaths in females. The pathogenesis of AD is associated with the development of neurofibrillary tangles and senile plaque formation. The aggregation of amyloid-beta (Aβ) peptides accounts for the development of senile plaques.[44] Commonly found within these senile plaques are coordinated metals such as iron, copper, and zinc. Such metals have been affiliated with encouraging the development of Aβ aggregation, particularly when bound to the methionine residue 35 (Met-35) of Aβ 1-42.[45] Iron, copper, and zinc have gained increasing amounts of interest in the study of AD due to their roles in provoking oxidative stress in the brain as well as affecting gene expression and increasing neurological inflammation.[46] In AD, iron and copper play significant roles in the development of oxidative stress contributing to the pathogenesis of AD.[47, 48] Fe^{2+} and Cu^{+} can be oxidised by molecules commonly found within a healthy brain such as oxygen and hydrogen peroxide. This, in turn, leads to the development of reactive oxygen species (ROS) such as the hydroxyl radical (OH•; Fig. 1.2).

These ROS can then react with biomolecules such as lipids, proteins and nucleic acids within the brain contributing to the neurodegeneration affiliated with AD.[47]

$$Fe^{2+} + H_2O_2 \rightarrow Fe^{3+} + OH\bullet + OH^-$$
$$Cu^{+} + H_2O_2 \rightarrow Cu^{2+} + OH\bullet + OH^-$$

Figure 1.2 Oxidation of Fe^{2+} and Cu^{+} with hydrogen peroxide yielding the hydroxyl radical, hydroxyl anion and Fe^{3+} and Cu^{2+} respectively.

The brain is particularly susceptible to oxidative stress as it consumes 20% of the body's total oxygen despite accounting to just 2% of its total mass. Normally, naturally occurring antioxidants such as catalase and superoxide dismutase (SOD) prevent the generation of oxidative stress, however, as we age this is believed to be less tightly regulated. The brain is also a rich source of lipids which can readily react with ROS.[49] Intracellularly, hyperphosphorylation of tau proteins, which form neurofibrillary tangles, is associated with oxidative stress.[48] Hence, there is significant importance for conducting studies which assist in the understanding of iron and copper trafficking and their contribution to oxidative stress intracellularly. Zinc is a redox-inert metal, with a high binding affinity for proteins, particular those consisting of amino acid residues with sulphur donor groups. The majority of biological zinc exists within metalloproteins and enzymes such as metallothioneins (MT), zinc finger proteins and carbonic anhydrase which are responsible for many vital roles involving inflammation, gene expression and metabolism.[50,51] The brain consists of the highest content of zinc compared with any other organ and so in a healthy brain, zinc is tightly regulated.[52] Oxidative stress induced neurodegeneration may potentially alter zinc metabolism in neuronal cells. Glutathione (GSH) is a reducing agent present in up to 5 mM within live cells and is primarily responsible for breaking intermolecular disulphide bonds in proteins.[53,54] In an oxidising environment GSH is oxidised to glutathione disulphide (GSSG).[53] GSSG has been shown to liberate zinc from MT (which is a major source of storage for zinc), as well as other zinc binding proteins, resulting in a drastic influx of labile zinc.[52] Due to its strong binding affinity to methionine residues, zinc readily coordinates to Aβ proteins resulting in the development of Aβ aggregates, neurotoxicity and ultimately AD.[44,55,56]

1.2.2 Biomedical Inorganic Chemistry

Organic molecules can enhance the medical properties of useful metals. Metals such as copper and silver are frequently coordinated to organic molecules which enhances their natural antimicrobial properties.[57] Complexes of gadolinium are used as contrast agents in magnetic resonance imaging (MRI).[58] Large, inert metals such as ruthenium and platinum have shown great success in DNA binding and ultimately functioning as anticancer drugs.[59] Perhaps the most renowned metal-based drug used for medical applications is cisplatin. Cisplatin is a complex of platinum bound in a square planer geometry to two chlorine and two amine donor groups with a *cis* stereochemistry. Cisplatin enters cells where the chlorine donors are exchanged for water donor groups. This complex can enter the nucleus where it binds to N7 nitrogens of the guanine base on a DNA strand creating a kink and prevent the transcription and replication of DNA, ultimately resulting in apoptosis via the p53 pathway in rapidly proliferating cells such as cancer cells.[60,61] Despite the success of cisplatin and other platinum-based anticancer drugs, platinum-based chemotherapies have limitations due to their adverse side-effects and intrinsic resistance. Therefore, the development of alternative organic and inorganic anticancer drugs is imperative to the enhancement of safer, more cancer-specific forms of chemotherapy.[62,63] Lanthanides have been of great intrigue to scientists for their magnetic and phosphorescent properties. Their high coordination number and strong binding capabilities allow lanthanides to adopt many different coordination geometries which can remain intact even after excretion from the human body.[58,64] Despite their vast uses in medical imaging, recent research suggests mild toxicity of lanthanides towards organisms.[64,65] Many research advancements have exploited the properties of lanthanides to enhance medical imaging. However, minimal medical research has delved into the potential of lanthanides for their application in other medical practices such as anticancer agents. This is despite the unique properties which may make complexes of lanthanides ideal DNA binders and hence, anticancer drugs.[65] In general, new developments in biomedical inorganic chemistry are currently in demand. Inorganic chemistry provides a plethora of different applications in medicinal chemistry within fields that have significant limitations which require addressing.

1.3 Design of a Fluorescent Sensor

In order to design the ideal fluorescent sensor for metal cations, it is important to

understand and exploit key concepts of fluorescent chemistry. Fluorescence is a phenomenon where a molecule is excited by an external source of light followed by an emission of a photon due to the excitation of an electron within such a molecule. The mechanisms of fluorescence are best described in a Jabłonski diagram also known as the electronic transition diagram (Fig. 1.3).

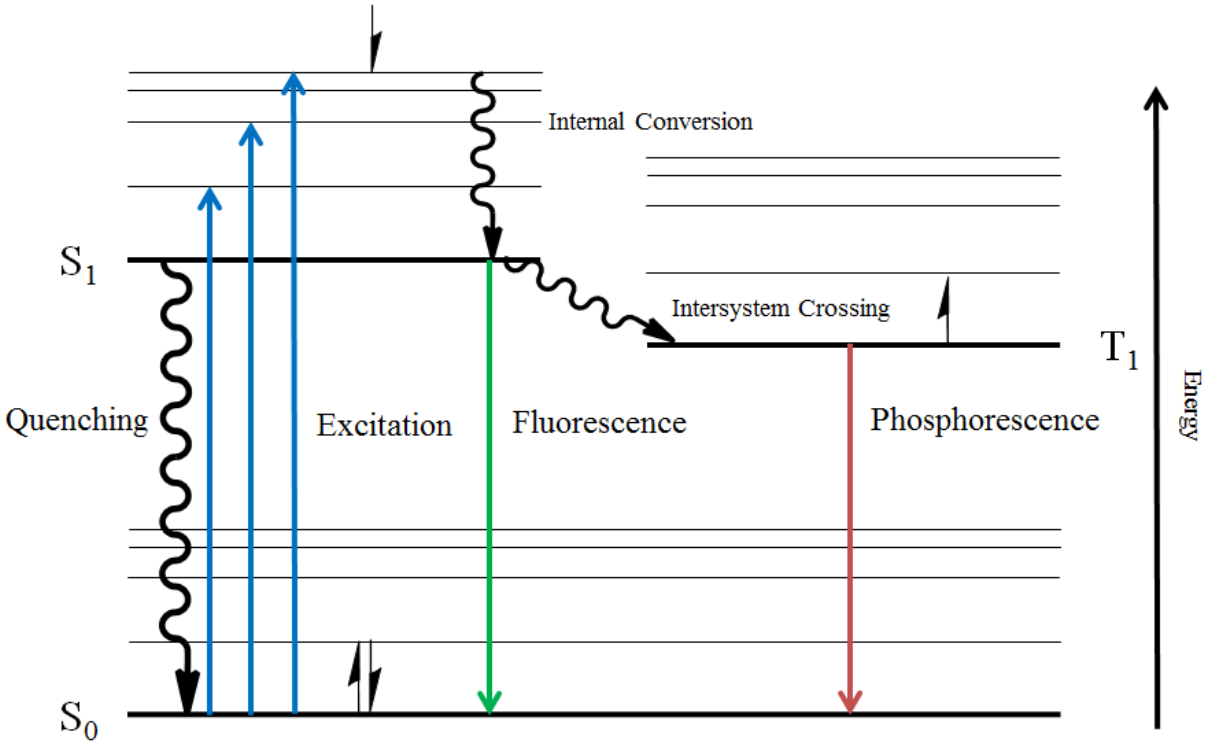

Figure 1.3 Jabłonski diagram indicating the quantum processes involved in absorbance, fluorescence and phosphorescence. Wavy lines indicate non-radiative processes. S_0 and S_1 are the ground and excited singlet states respectively, where electrons remain in a spin up and spin down state. T_1 indicates the excited triplet state where both electrons are in the spin up state. Excited singlet states beyond S_1 (ie. S_n; $n = >1$) are not shown.[66]

As a molecule absorbs photons it induces an electron passage from the singlet ground electronic level (S_0) to an excited state (S_n, $n = \geq 1$) and will return to the ground S_0 state via the lowest excited state (S_1). Some energy is thereby lost in the form of thermal energy to the surrounding environment via internal conversion. The electron then transitions from the S_1 back to the most thermodynamically stable S_0 state by four possible mechanisms:

1. Intersystem crossing reoccurs where energy is lost by the molecule in the form of non-radiative heat.
2. The excited molecule releases its energy to a nearby molecule resulting in the quenching of fluorescence. This typically occurs in the presence of paramagnetic metals such as Fe^{3+}, Co^{2+} and Cu^{2+}.
3. The energy is emitted as a photon (fluorescence) at a lower energy wavelength compared to that of the wavelength that excited the molecule as some energy is always lost as heat due to internal conversion.
4. Intersystem crossing to the triplet (T_1) state occurs. T_1 is a lower energy state than S_1, however, is meta-stable and long-lived as triplet state transitions are spin-forbidden and thereby the emission of photons has a longer lifetime comparatively to that of fluorescence. This phenomenon is referred to as phosphorescence and typically occurs in lanthanides such as europium.[67,68]

1.3.1 Photo-Induced Electron Transfer (PET)

Photo-induced electron transfer (PET) is a commonly exploited mechanism of action which many fluorescent probes exhibit.[69] PET is a quenching process which involves reduction and oxidation between the fluorophore and the receptor of a molecule. In PET, electrons from the fluorophore are unable to be excited from the highest-occupied molecular orbital (HOMO) to the lowest unoccupied molecular orbital (LUMO). This is due to the energy level of the HOMO of the receptor being in-between that of the HOMO and LUMO of the fluorophore. This results in the oxidation of the receptor, donating an electron to the reduced fluorophore. Ultimately, electrons from the fluorophore are unable to return to the ground state as ground state electrons are paired and no fluorescence is produced. When an analyte binds to the receptor, the energy of the HOMO of the receptor may then decrease below that of the HOMO of the fluorophore. Therefore, fluorescence is re-enabled as no reduction occurs and electrons from the fluorophore are able to relax again (Fig. 1.4).[70-72]

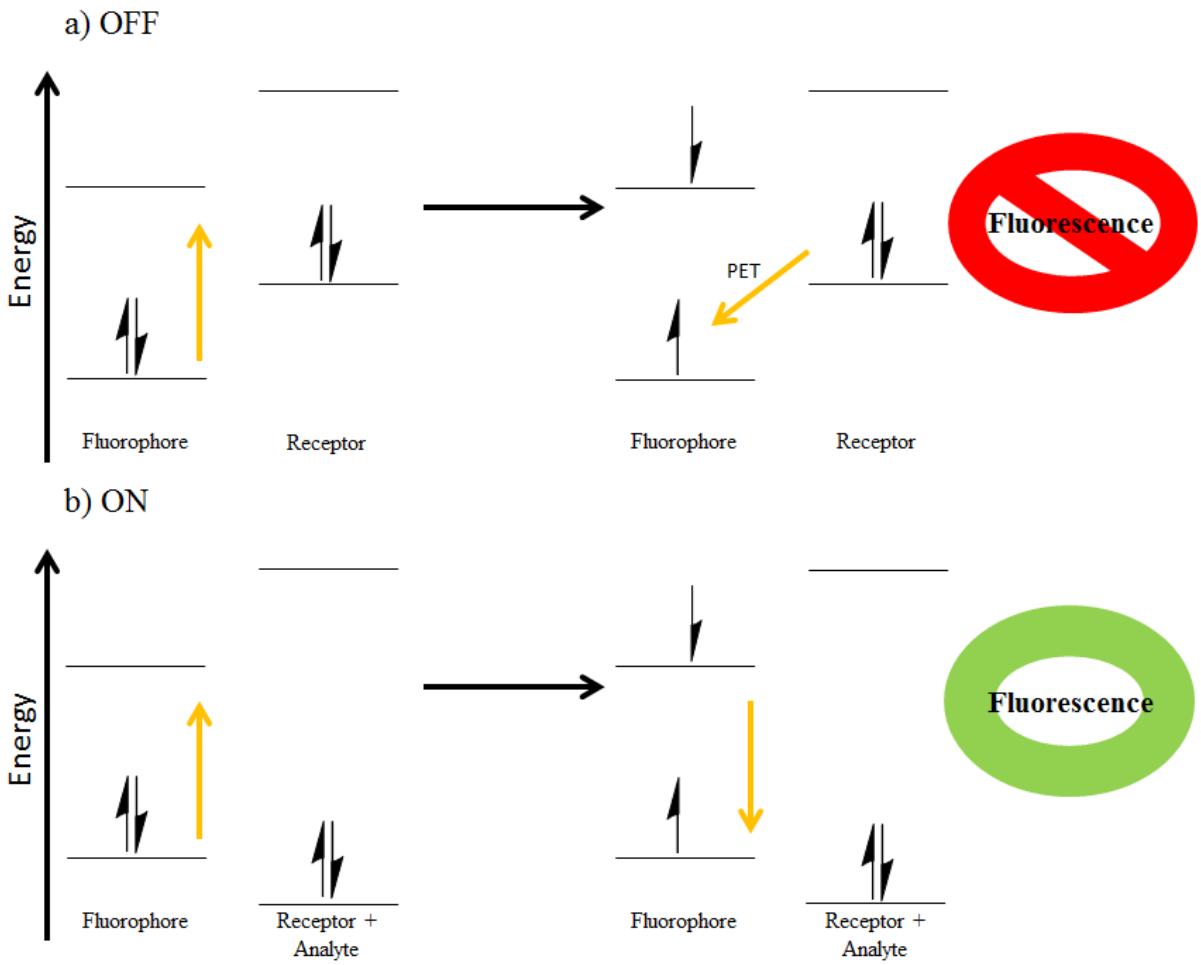

Figure 1.4 (a) Electron diagram of the 'OFF' state and the (b) 'ON' state of a fluorescent probe exploiting PET as a means of emitting fluorescence when bound to its analyte. Amber arrows indicate the movement of electrons.[72]

1.3.2 Förster Resonance Energy Transfer (FRET)

Förster resonance energy transfer (FRET) is a type of energy transfer which occurs within close proximity to an electron donor and acceptor resulting in either fluorescence or quenching. FRET can occur when the emission band of the donor and the acceptor's excitement band overlap. The acceptor may, in turn, fluoresce at a lower energy wavelength than that of the donor. FRET occurs when a donor molecule is initially excited by an external photon when within 1-10 nm of the acceptor. The donor transfers its excited electron to the acceptor via a non-radiative transfer where it can relax back to the ground state emitting a

photon at a lower energy wavelength. This is the primary mechanism in which most ratiometric probes function, as one fluorophore acts as a donor, emitting light at shorter wavelengths to that of the acceptor fluorophore. Quenching can potentially occur if energy is lost by the acceptor as heat due to internal conversion (Fig. 1.5).[71,73,74]

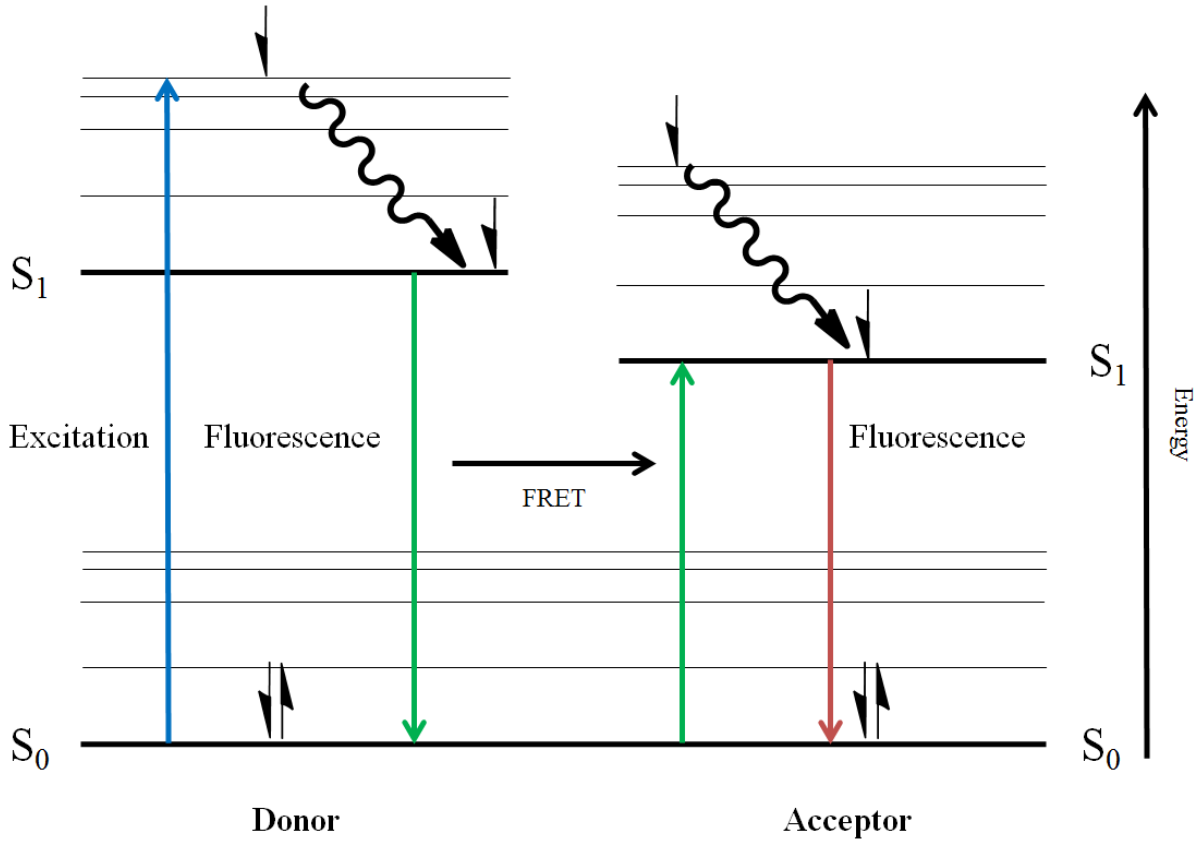

Figure 1.5 Jabłonski diagram representing the mechanism of FRET between two fluorophores. Colours of the arrows indicate the approximate wavelengths between each excitation and fluorescence.[74]

1.4 Characteristics of Ideal Fluorescent Sensors in Biological Systems

Different applications of fluorescent sensors alter the specific characteristics which deem the sensor to be 'ideal'. For the sake of this thesis, the applications of the fluorescent sensors are designed to sense metal ions that are of intrigue to scientists for their potential roles in AD (notably Al^{3+}, Fe^{3+}, Cu^{2+}, and/or Zn^{2+}). These sensors will, therefore, have to be suitable for cellular studies using fluorescent microscopy and those that sense metals such as

aluminium and iron, which also effect the environment, will have to be able to detect such metals in different water systems. When designing fluorescent sensors, there are specific considerations which make them more practical and therefore more desirable for real-world applications. Some of these are listed below:

1. Financial Suitability

The metal sensors being designed are ideally needed to be suitable for mass production. Therefore precursors are required to be inexpensive and synthetic pathways need to be short, simple and produce high yields.[75]

2. Biologically Innocuous

As these sensors are to be required for biological practices, they need to be innocuous to living organisms. Molecules are also further desired if the precursors are biologically innocuous in case degradation occurs.

3. Water Solubility yet Membrane Permeable

As the environment of living organisms is always aqueous, it is essential for fluorescent sensors to be water soluble whilst also being able to cross the phospholipid bilayer of the cellular membrane. With animal cells which do not consist of a cell wall, this can be achieved by designing organic molecules consisting of hydrophilic moieties such as amines, hydroxyls and carboxylic acids. Otherwise, when molecules are dissolved in dimethyl sulphoxide (DMSO) they can become permeabilised, however, high concentrations of DMSO are cytotoxic.

4. Selectivity

Sensors must have selectivity towards the analyte they are detecting, at least at the emission wavelength it is detecting it at. This can be achieved by using binding groups that are specific to the analyte it is designed to sense. This is not always easily achievable as binding groups will have many different binding partners which compete with the desired analyte. This can result in an insufficient amount of fluorescence enhancement, quenching of

fluorescence or even multiple different analytes creating a similar fluorescent response. The analyte also needs to have a high binding affinity towards the probe to ensure they do not competitively bind with biomolecules such as GSH.

5. Observable Amount of Fluorescent Output

The change in fluorescence, either by a shift in emission or fluorescent enhancement, needs to be sufficient enough to be distinguishable from the unbound probe. The brightness of the probe also needs to be able to be distinguished from background noise and in fluorescent microscopy, reduce the intensity of the laser power which can potentially be harmful to cells. The quantum yield (ϕ) can be measured from comparing the amount of light absorbed to the amount of light emitted to indicate the efficiency of the probe. Quantum yield can then determine brightness which commonly occurs between 10^3 - 10^5 M^{-1} cm^{-1} for fluorescent sensors.

6. Excitation at Lower Energy Wavelengths

Fluorescent probes that excite at lower energy wavelengths are ideal to reduce damage to DNA and proteins in cells as well as reduce auto-fluorescence due to near ultraviolet (UV) excitation of fluorescent biomolecules such as tryptophan, flavins and nicotinamide cofactors (eg. NADH).[76,77]

7. Photostability

It is essential that fluorescent probes are less prone to degradation that may occur due to the high-intensity lasers used to excite the sensor. Great photostability increases the time experimentation can occur and ensures that fluorescent intensity is consistently high enough to evoke sufficient detection.

8. Sufficient Difference in Excitation and Emission Wavelength

Self-quenching can occur when there is an overlap between the excitation and emission bands due to re-absorbance of emitted light by neighbouring molecules. A larger

difference in energy between the excited to emission band (Stokes shift) is therefore preferred as self-quenching can limit the detection of the analyte at high concentrations (Fig. 1.6).

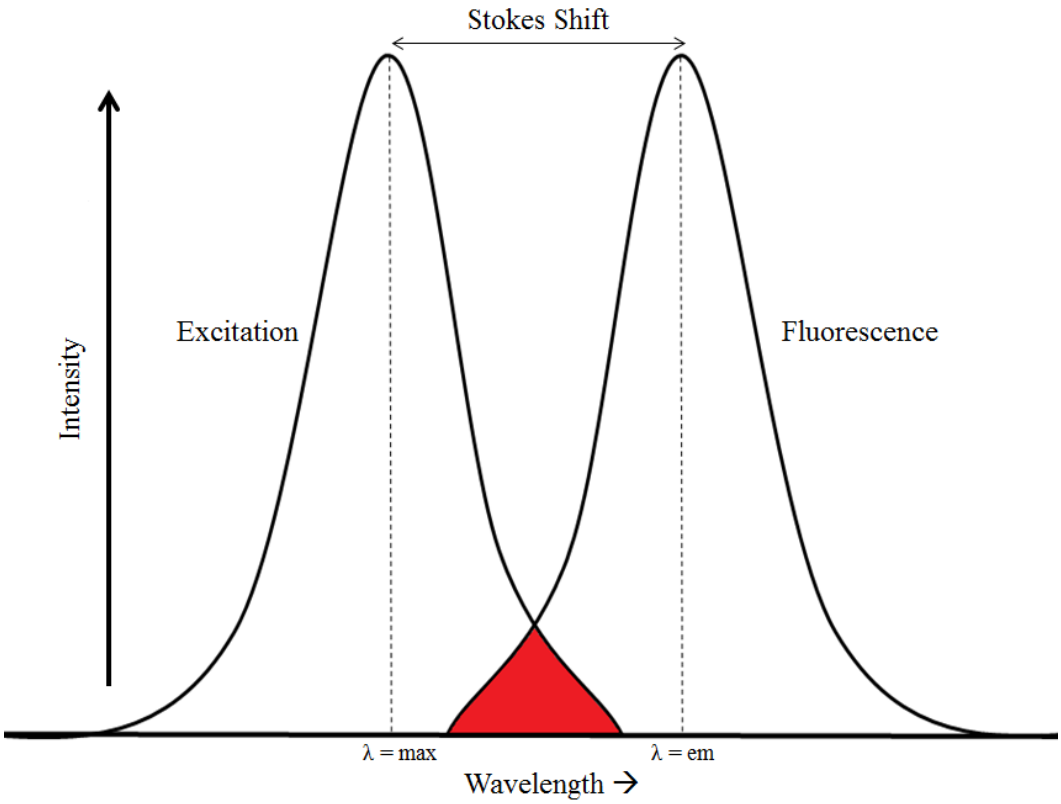

Figure 1.6 Representation of excitation and fluorescence bands overlapping (indicated in red) where self-quenching can occur. [77]

9. Ratiometric

The most desired fluorescent sensors give responses that are ratiometric. This is where the probe alone emits at a specific wavelength of light different to that of the analyte bound to the probe. Therefore the analyte can potentially be quantified by comparing the fluorescent intensity from the emission of the probe compared to that of the emission intensity of the analyte bound to the probe. Ratiometric probes are also able to be tracked as to whether and where they migrate intracellularly. This is important as organelles such as the cell nucleus, mitochondria and chloroplasts are enclosed by a membrane. If a probe is unable to enter into all compartments of cells then it may not be able to sense its desired analyte.

1.5 Choice of Ligands

1.5.1 Schiff Bases as Fluorescent Sensors for Detecting Metal Ions

A Schiff base condensation reaction results with the deamination of a primary amine by a carbonyl, yielding water and a Schiff base with an imine moiety (Fig. 1.7). Schiff base condensation reactions are frequently conducted by chemists, especially among supramolecular chemists, because of their ease of synthesis, high yields, strong coordinative ability and a vast amount of applications to various scientific fields including medicine as anticancer and antimicrobial agents.[78-80]

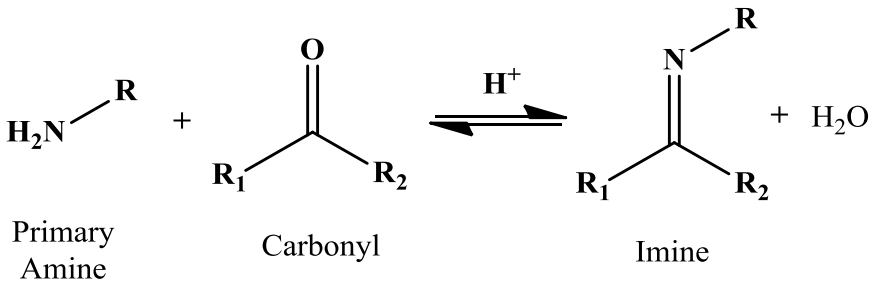

Figure 1.7 Schiff base condensation reaction. R and R_1 groups denote to carbon substituent. R_2 can be either a carbon substituent (forming a ketone) or hydrogen (forming an aldehyde).[80]

Among their many applications, Schiff bases have been widely recognised as exceptional chemosensors. Schiff bases are frequently used as selective 'turn-on' fluorescent probes with a large amount of fluorescent output, especially for metals such as aluminium and zinc ions. Such Schiff base probes often incorporate PET as a mechanism of fluorescent enhancement due to the resonance of the lone pair electrons upon the imine moiety.[81-83] Schiff bases are also frequently found as fluorescent enhancement as well as quenching probes in the presence of copper and iron ions.[82,84,85] These four metals (Al, Fe, Cu and Zn) are of immense intrigue due to their roles in developing the neurodegeneration associated with AD. Schiff bases decompose in aqueous solutions due to hydrolysis. Studies have however indicated that decomposition is halted by the coordination of metal ions, resulting in stable complexes not only in water but also in high-intensity light. Regardless, when designing Schiff bases for biological applications considerations should be made to ensure non-toxicity of not only the Schiff base, but also the precursor

molecules. With this in mind, Schiff bases have been successfully used for biological purposes and have had little effect on cell viability.[1,2,79,86] Due to the relative ease of synthesis, strong coordinative ability, photostability and ability to selectivity sense biological metal ions with high fluorescent intensity, Schiff bases make the ideal design for a practical fluorescent probe.

1.5.2 The Chosen Ligands

The chosen ligands in this thesis report that will be analysed in chapters two, three and four, respectively are $H_2\mathbf{L}^{I}$, $H_3\mathbf{L}^{II}$ and $H_3\mathbf{L}^{III}$.

$H_2\mathbf{L}^{I}$ is a promising PET induced Al^{3+} fluorescent enhancer with ideal applications for confocal studies due to its high sensitivity, non-toxicity and significant blue-shift in fluorescence when bound to its analyte. $H_2\mathbf{L}^{I}$ is easily synthesised via a Schiff base condensation reaction between L-tryptophan and 4-diethylamino salicylaldehyde and coordinates to aluminium at a 1:2 ligand-to-metal stoichiometry.

$H_3\mathbf{L}^{II}$ and its lanthanide complexes $[Ln(\mathbf{L}^{II})_2]^{3-}$ (where Ln = either Eu^{3+}, Gd^{3+} or Dy^{3+}) display great potential as anticancer drugs. $H_3\mathbf{L}^{II}$ also has some potential as a Zn^{2+} fluorescent sensor, however, due to its low half maximal effective concentration (EC_{50}), is not ideal as a fluorescent sensor. Thereby, $H_3\mathbf{L}^{II}$ is coordinated to trivalent lanthanides to observe the potential use of $H_3\mathbf{L}^{II}$ and its lanthanide complexes as anticancer agents upon an array of different cell lines. Cell viabilities of $H_3\mathbf{L}^{II}$ are compared to the lanthanide complexes to evaluate the suitability of lanthanide complexes as anticancer drugs. $H_3\mathbf{L}^{II}$ and its complexes are further studied using spectral techniques to demonstrate their ability to bind to calf thymus DNA (ctDNA). $H_3\mathbf{L}^{II}$ is synthesised from L-ornithine and two equivalents of 2-hydroxy-1-naphthaldehyde via a Schiff base condensation reaction and its lanthanide complexes are synthesised forming 2:1 ligand-to-metal stoichiometry.

$H_3\mathbf{L}^{III}$ demonstrates great potential as a fluorescent enhancement probe for Al^{3+}. $H_3\mathbf{L}^{III}$ binds to Al^{3+} in a 1:1 stoichiometry resulting in a high amount of sensitivity. $H_3\mathbf{L}^{III}$ is also very photostable, has a very low limit of detection (LoD) and has strong immunity to hydrolysis in aqueous conditions. $H_3\mathbf{L}^{III}$ is synthesised from the Schiff base condensation reaction between L-cysteine and 2-hydroxy-1-naphthaldehyde.

1.6 Aims and Scope

This project aimed to design and synthesise amino acid-derived Schiff base ligands for the purpose of detecting metal ions implicated in the pathogenesis of AD. Initially the ligands were designed, synthesised and characterised. The ligands then underwent fluorescent and colourimetric assessments to determine if they could act as metal sensors. Ligands that were selective to biometals were then screened for their biocompatibility using cell viability assays. Ligands with little or no effect on cell viability were then further investigated for their potential application as fluorescent sensors whereas ligands with high cytotoxicity were coordinated to lanthanide ions and studied for further anticancer and DNA binding potential (Fig. 1.8).

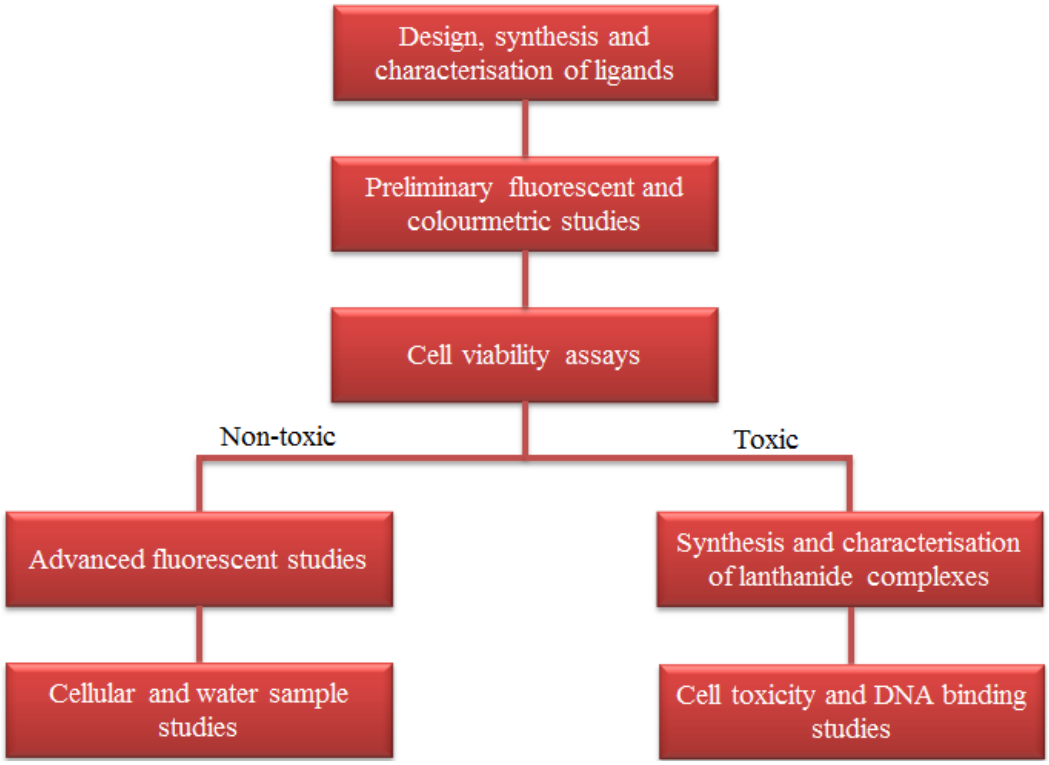

Figure 1.8 Flowchart of the steps that were conducted in order to present the research in this thesis report.

1.7 Reference List

1. J. W. Steed & J. L. Atwood. *Supramolecular Chemistry*. (John Wiley & Sons, 2009).
2. J. W. Steed, D. R. Turner & K. J. Wallace. *Core Concepts in Supramolecular Chemistry*. (John Wiley & Sons, 2007).
3. J.-M. Lehn. *Supramolecular Chemistry: Concepts and Perspectives*. (VCH, 1995).
4. M.-X. Wang. Supramolecular chemistry: defined. *Supramol. Chem.* **28,** 1–3 (2016).
5. R. Langridge, D. A. Marvin, W. E. Seeds & H. R. Wilson. The Molecular Configuration of Deoxyribonucleic Acid. *J. Mol. Biol.* **2,** 38–64 (1960).
6. J. L. Atwood & Jonathan W. Steed. *Encyclopedia of Supramolecular Chemistry*. **1,** (Marcel
Dekker Inc., 2004).
7.H. Engelkamp, S. Middelbeek & R. J. M. Nolte. *Science* **284,** 785–788 (1999).
8. B. Hasenknopf, J.-M. Lehn, B.O. Kneisel, G. Baum & D. Fenske. Self-Assembly of a Circular Double Helicate. *Angew. Chem. Int.* **35,** 1838–1840 (1996).
9. F. Gandara *et al.* 2D and 3D Supramolecular Structures via Hydrogen Bonds and π-Stacking
Interactions in Arylsulfonates of Nickel and Cobalt. *Inorg. Chem.* **45,** 9680–9687 (2006).
10. R. Crabtree. *The Organometallic Chemistry of the Transition Metals*. (John Wiley & Sons,
2009).
11. M.-X. Wang. Supramolecular chemistry: defined. *Supramol. Chem.* **28,** 1–3 (2016).
12. H.-J. Schneider. *Applications of Supramolecular Chemistry*. (CRC Press, 2012).
13. L. Li *et al.* Direct monitoring of spin transitions in a dinuclear triple-stranded helicate iron(II) complex through X-ray photoelectron spectroscopy. *Dalton Trans.* **47,** 2543–2548 (2018).
14. S. R. Seidel & P. J. Stang. High-Symmetry Coordination Cages via Self-Assembly. *Acc. Chem. Res.* **35,** 972–983 (2002).
15. R. G. Pearson. Hard and Soft Acids and Bases. *J. Am. Chem. Soc.* **85,** 3533–3539 (1963).
16. S. Ahrland, J. Chatt & N. R. Davies. The relative affinities of ligand atoms for acceptor molecules and ions. *Q. Rev. Chem. Soc.* **12,** 265–276
17. S. Hati & D. Datta. Hardness: A concept in inorganic chemistry. Some aspects. *Proc. Indian*
Acad. Sci. **3,** 143–158 (1996).
18. C. E. Housecroft. *Inorganic Chemistry*. (Pearson Education Limited, 2008).
19. J. J. R. Frausto da Silva & R. J. P. Williams. *The Biological Chemistry of the Elements: The*
Inorganic Chemistry. (International Union of Biochemistry and Molecular Biology, Inc., 2001).
20. H. Irving & R. J. P. Williams. The stability of transition-metal complexes. *J. Chem. Soc.* **0,**
3192–3210 (1953).
21. D. J. Hare, E. J. New, M. D. de Jonge & G. McColl. Imaging metals in biology: balancing sensitivity, selectivity and spatial resolution. *Chem. Soc. Rev.* **44,** 5941–5958 (2015).
22. F. P. Guengerich. Thematic Minireview Series: Metals in Biology 2014. *Journa Biol. Chem.*
289, 28094 (2014).
23. W. Maret. The Metals in the Biological Periodic System of the Elements: Concepts and Conjectures. *Int. J. Mol. Sci.* **17,** 1–8 (2016).
24. D. R. Williams. Metals, Ligands, and Cancer. *Chem. Rev.* **72**, 203–213 (1972).

25. E. J. Hoorn, M. G. H. Betjes, J. Weigel & R. Zietse. Hypernatraemia in critically ill patients:
too little water and too much salt. *Nephrol. Dial. Transplant.* **23,** 1562–1568 (2008).
26. R. R. Crichton. *Biological Inorganic Chemistry : A New Introduction to Molecular Structure*
and Function. (Elsevier, 2012).
27. A. I. Bush. Metals and neuroscience. *Curr. Opin. Chem. Biol.* **4,** 184–191 (2000).
28. H. J. Johnston *et al.* A review of the in vivo and in vitro toxicity of silver and gold particulates: Particle attributes and biological mechanisms responsible for the observed toxicity.
Crit. Rev. Toxicol. **40,** 328–346 (2010).
29. F. Zahir, S. J. Rizwi, S. K. Haq & R. H. Khan. Low dose mercury toxicity and human health. *Environ. Toxicol. Pharmacol.* **20,** 351–360 (2005).
30. L. Järup. Cadmium overload and toxicity. *Nephrol. Dial. Transplant.* **17,** 35–39 (2002).
31. B. O. Rosseland, T. D. Eldhuset & M. Staurnes. Environmental effects of aluminium. *Environ. Geochem. Health* **12,** 17–27 (1990).
32. E. D. Burton, R. T. Bush & L. A. Sullivan. Sedimentary iron geochemistry in acidic waterways associated with coastal lowland acid sulfate soils. *Geochim. Cosmochim. Acta* **70,** 5455–5468 (2006).
33. K. Mal *et al.* Dihydroindeno[1,2-b]pyrroles: new Al3+ selective off–on chemosensors for bio-imaging in living HepG2 cells. *Org Biomol Chem* **16,** 5920–5931 (2018).
34. C. Exley. A biogeochemical cycle for aluminium? *J. Inorg. Biochem.* **97,** Journal of Inorganic Biochemistry (2003).
35. K. Tennakone, S. Wickramanayake & C. A. N. Fernando. Aluminium contamination from
fluoride assisted dissolution of metallic aluminium. *Environ. Pollut.* **49,** 133–143 (1988).
36. X. Shi-Gang, S. Li-Xin, Z. Rong-Gen & H. Xing-Fang. Properties of aluminium oxide coating on aluminium alloy produced by micro-arc oxidation. *Surf. Coat. Technol.* **199,** 184 188 (2005).
37. K. R. Koch, M. A. Pougnet, S. de Villiers & F. Monteagudo. Increased urinary excretion of
Al after drinking tea. *Nature* **12,** 122 (1988).
38. S. J. Zheng. Crop production on acidic soils: overcoming aluminium toxicity and phosphorus deficiency. *Ann. Bot.* **106,** 183–184 (2010).
39. S. J. Carr, G. S. P. Ritchie & W. M. Porter. A soil test for aluminium toxicity in acidic subsoils of yellow earths in Western Australia. *Aust. J. Agric. Res.* **42,** 875–892 (1991).
40. V. B. Gupta *et al.* Aluminium in Alzheimer's disease: are we still at a crossroad? *Cell. Mol.*
Life Sci. **62,** 143–158 (2005).
41. A. Campbell. The potential role of aluminium in Alzheimer's disease. *Nephrol. Dial. Transplant.* **17,** 17–20 (2002).
42. J. P. Landsberg, B. McDonald & F. Watt. Absence of aluminium in neuritic plaque cores in
Alzheimer's disease. *Nature* **360,** 65–68 (1992).
43. T. P. Flaten. Aluminium as a risk factor in Alzheimer's disease, with emphasis on drinking
water. *Brain Res. Bull.* **55,** 187–196 (2001).
44. C. J. Maynard, A. I. Bush, C. L. Masters, R. Cappai & Q.-X. Li. Metals and amyloid-β in Alzheimer's disease. *Int J Exp Path* **86,** 147–159 (2005).
45. D. A. Butterfeild. Amyloid b-peptide (1–42)-induced Oxidative Stress and

Neurotoxicity: Implications for Neurodegeneration in Alzheimer's Disease Brain. A Review. *Free Radic. Res.* **36,** 1307–1313 (2002).
46. M. Loef, N. von Stillfried & H. Walach. Zinc diet and Alzheimer's disease: a systematic review. *Nutr. Neurosci.* **15,** 2–12 (2012).
47. W.-J. Huang, X. Zhang & W.-W. Chen. Role of oxidative stress in Alzheimer's disease (Review). *Biomed. Rep.* **4,** 519–522 (2016).
48. A. Gella & N. Durany. Oxidative stress in Alzheimer disease. *Cell Adhes. Migr.* **3,** 88–93 (2009).
49. D. G. Smith, R. Cappai & K. J. Barnham. The redox chemistry of the Alzheimer's disease amyloid β peptide. *Biochim. Biophys. Acta* **1768,** 1976–1990 (2007).
50. A. S. Prasad. *Biochemistry of Zinc*. (Springer Science & Business Media, 2013).
51. M. P. Cuajungco & G. J. Lees. Zinc Metabolism in the Brain: Relevance to Human Neurodegenerative Disorders. *Neurobiol. Dis.* **4,** 137–169 (1997).
52. S. Vasto *et al.* Inflammation, genes and zinc in Alzheimer's disease. *Brain Res. Rev.* **58,** 96
105 (2008).
53. H. Sies. Glutathione and its Role in Cellular Functions. *Free Radic. Biol. Med.* **27,** 916–921
(1999).
54. H. Y. Au-Yeung, E. J. New & C. J. Chang. A selective reaction-based fluorescent probe for
detecting cobalt in living cells. *Chem Commun* **48,** 5268–5270 (2012).
55. M. S. Zaman *et al.* Protein kinase CK2 regulates metal toxicity in neuronal cells. *Metallomics* **8,** 82–90 (2016).
56. M. C. McCord & E. Aizenman. The role of intracellular zinc release in aging, oxidative stress, and Alzheimer's disease. *Front Aging Neurosci* **6,** 1–16 (2014).
57. R. B. Thurman, C. P. Gerba & G. Bitton. The molecular mechanisms of copper and silver ion disinfection of bacteria and viruses. *Crit. Rev. Environ. Sci. Technol.* **18,** 295–315 (1989).
58. P. Caravan, J. J. Ellison, T. J. McMurry & R. B. . Lauffer. Gadolinium(III) Chelates as MRI
Contrast Agents: Structure, Dynamics, and Applications. *Chem Rev* **99,** 2293−2352 (1999).
59. N. Muhammad & Z. Guo. Metal-based anticancer chemotherapeutic agents. *Curr. Opin. Chem. Biol.* **19,** 144–153 (2014).
60. A. L. Pinto & S. J. Lippard. Binding of the Antitumour Drug cis
Diamminedichloroplatinum(II) (Cisplatin) to DNA. *Biochim. Biophys. Acta BBA - Rev. Cancer*
780, 167–180 (1985).
61. B. Lippert. *Cisplatin: Chemistry and Biochemistry of a Leading Anticancer Drug*. (John Wiley & Sons, 1999).
62. I. Kostova. Lanthanides as Anticancer Agents. *Curr. Med. Chem. - Anti-Cancer Agents* **5,** 591–602 (2005).
63. P. C. A. Bruijnincx & P. J. Sadler. New trends for metal complexes with anticancer activity.
Curr. Opin. Chem. Biol. **12,** 197–206 (2008).
64. P. Tai, Q. Zhao, D. Su, P. Li & F. Stagnitti. Biological toxicity of lanthanide elements on algae. *Chemosphere* **80,** (2010).
65. Z.-Q. Xu *et al.* Synthesis, characterization and anticancer activities of two lanthanide(III) complexes with a nicotinohydrazone ligand. *J. Mol. Struct.* **1102,** 86–90 (2015).
66. Von A. JabtoJisk. Uber den Mechanismus der Photolumineszenz yon Farbstoffphosphoren.

Z. Für Phys. **94,** 38–64 (1935).
67. C. E. Housecroft & A. G. Sharpe. *Inorganic Chemistry*. (Pearson Education Limited, 2012).
68. J. R. Albani. *Principles and Applications of Fluorescence Spectroscopy*. (John Wiley & Sons, Incorporated, 2008).
69. A. P. de Silva, T. S. Moody & G. D. Wright. Fluorescent PET (Photoinduced Electron Transfer) sensors as potent analytical tools. *Analyst* **134,** 2385–2393 (2009).
70. J. R. Lakowicz. *Principles of Fluorescence Spectroscopy*. (Springer Science and Business Media, 2013).
71. A. P. Demchenko. *Introduction to Fluorescence Sensing*. (Springer, 2015).
72. D. Escudero. Revising Intramolecular Photoinduced Electron Transfer (PET) from First Principles. *Acc Chem Res* **49,** 1816−1824 (2016).
73. Y. Hu, J. Wang, L. Long & X. Xiao. A ratiometric fluorescence sensor for Fe3+basedonFRETandPETprocesses. *Luminescence* **31,** 16–21 (2016).
74. A. Hussain. An Introduction to Fluorescence Resonance Energy Transfer (FRET). (2009).
75. S. Kim *et al.* Salicylimine-Based Fluorescent Chemosensor for Aluminium Ions and Application to Bioimaging. *Inorg Chem* **51,** 3597–3602 (2012).
76. L. Yuan, W. Lin, K. Zheng, L. He & W. Huang. Far-red to near infrared analyte-responsive
fluorescent probes based on organic fluorophore platforms for fluorescence imaging. *Chem Soc*
Rev **42,** 622--661 (2013).
77. L. D. Lavis & R. T. Raines. Bright Ideas for Chemical Biology. *ACS Chem Biol* **3,** 142–155
(2018).
78. W. Qin, S. Long, M. Panunzio & S. Biondi. Schiff Bases: A Short Survey on an Evergreen
Chemistry Tool. *Molecules* **18,** 12264–12289 (2013).
79. D. R. Klein. *Organic Chemistry*. (John Wiley & Sons, 2015).
80. M. Li. *Organic Chemistry of Drug Degradation*. (RSC Publishing, 2012).
81. J. Zhu *et al.* A simple turn-on Schiff base fluorescence sensor for aluminium ion. *Tetrahedron Lett.* **57,** 3535–3539 (2016).
82. Y. W. Choi *et al.* A single Schiff base molecule for recognizing multiple metal ions: A fluorescence sensor for Zn(II) and Al(III) and colorimetric sensor for Fe(II) and Fe(III). *Sens. Actuators B* **194,** 343–352 (2014).
83. K. B. Kim *et al.* A cap-type Schiff base acting as a fluorescence sensor for zinc(II) and a colorimetric sensor for iron(II), copper(II), and zinc(II) in aqueous media. *Dalton Trans.* **42,** 16569–16577 (2013).
84. L. Yang, W. Zhu, M. Fang, Q. Zhang & C. Li. A new carbazole-based Schiff-base as fluorescent chemosensor for selective detection of Fe 3+ and Cu 2+. *Spectrochim Ica Acta Part*
Mol. Biomolecu Lar Spect Rosco Py **109,** 186–192 (2013).
85. M. Shellaiah, Y.-H. Wu, A. Singh, M. V. R. Raju & H.-C. Lin. Novel pyrene- and anthracene-based Schiff base derivatives as Cu2+ and Fe3+ fluorescence turn-on sensors and for
aggregation induced emissions. *J Mater Chem A* **1,** 1310–1318 (2013).
86. A. C. W. Leung & M. J. MacLachlan. Schiff Base Complexes in Macromolecules. *J. Inorg.*
Organomet. Polym. Mater. **17,** 57–89 (2007).

Chapter 2 – L-Tryptophan-Derived, Water-Soluble Schiff Base as a Blue-Shift Fluorescent Sensor for Detecting Al^{3+} in Aqueous Solutions and Intracellular Environments

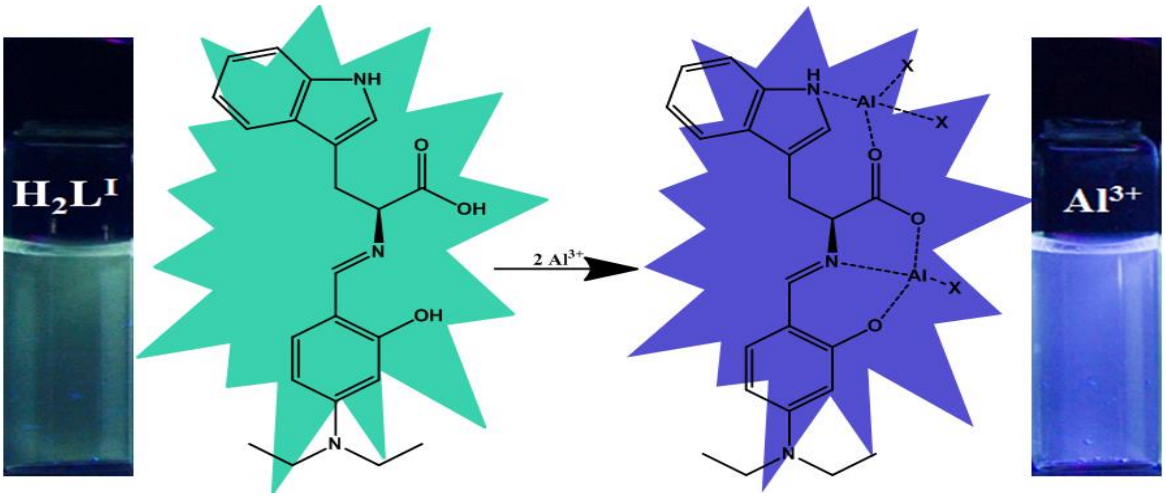

2.1 Abstract

Aluminium is the most abundant metallic element in the Earth's crust. Within acidic environments, oxyphilic aluminium forms into aluminium oxides where it is readily solubilised in water and potentially toxic to many lifeforms. Recent studies have correlated aluminium with the development of Alzheimer's disease (AD); however, much research has also contradicted these claims. Due to such reasons, much research is currently investigating the roles aluminium plays in biological systems. Fluorescent sensors provide an imperative tool in investigating the roles of metals (such as aluminium) in biological systems. However, current fluorescent probes of aluminium exist with major limitations including negative effects on cell viability and a general lack of biological analysis. Herein, ligand ($H_2\mathbf{L}^{I}$) is synthesised and characterised via a Schiff base condensation reaction between L-tryptophan (a fluorescent amino acid) and 4-diethylamino salicylaldehyde to a yield of ~70%. Water-soluble $H_2\mathbf{L}^{I}$ exhibits a blue-shift from 533 nm to 405 nm when bound to its Al^{3+} analyte which is detectable even in the presence of other potentially interfering metal ions. $H_2\mathbf{L}^{I}$ exhibits a limit of detection (LoD) of 61.5 nM and a 1:2 ligand-to-metal stoichiometry is determined. $H_2\mathbf{L}^{I}$ is observed to be non-toxic from up to 500 µM and is able to sense for Al^{3+} within 1321N1 astrocytoma cells as well as in different water samples.

2.2 Introduction

Aluminium constitutes to 8.3% of the lithosphere by mass and is the ninth most abundant metal in humans.[1,2] Its toxicity towards agriculture and humans is of immense intrigue to scientists in environmental and medical fields. Aluminium is prevalent in utensils within common workplaces and households, it is also abundantly found in pharmaceuticals such as antacids, as well as in cosmetics such as antiperspirants. These factors result in a high exposure of aluminium to both humans and the environment.[3-5] Solid aluminium readily oxidises into aluminium oxides in acidic environments where it becomes highly water-soluble and toxic to wildlife within aqueous environments.[6-8] According to the Department of Agriculture and Food, Western Australian Government, a low 2-5 ppm of Al^{3+} is toxic to the roots of aluminium-sensitive plants. This is of particular concern to regions such as Western Australia where high levels of mining and agriculture coexist, resulting in a high exposure of toxic, water-soluble Al^{3+} to soils and crops due to acid rain formation.

Aluminium has recently gained much interest in the field of medicine due to its apparent effects on the development of AD.[9] Aluminium's role in AD is, however, frequently disputed and therefore the development of new research tools is imperative to augment the understanding of the biological behaviours and influences of the metal.[10-12] The use of fluorescent sensors have been abundantly used as effective tools in the study of different metal ions in biological systems. In biology, fluorescent sensors are favoured over other chemosensory techniques due to their significant sensitivity and ability to be detected through cellular membranes.[13,14] Current aluminium sensors come with significant limitations. For example, some have low selectivity for Al^{3+} and others often lack practicality due to complicated and expensive synthetic procedures, poor water solubility, poor fluorescence intensity and some are cytotoxic or decompose into cytotoxic compounds (Table 2.1).[15,16] Therefore, there is a great demand for the development of new fluorescent sensors with optimised characteristics and enhanced practicality for the detection of Al^{3+} in aqueous solutions for their potential biological applications.

Herein, ligand ($H_2\mathbf{L}^{I}$) is synthesised via a Schiff base condensation reaction between L-tryptophan and 4-diethylamino salicylaldehyde and characterised by ^{1}HNMR and ^{13}CNMR, Electrospray Ionisation - High Resolution Mass Spectrometry (ESI-HRMS), FT-IR, simultaneous thermal analysis (STA), powdered X-ray diffraction (P-XRD) and Single

crystal X-ray diffraction (SC-XRD). $H_2\mathbf{L}^I$ has been designed for its practicality as it is synthesised with a high yield by a simple one-step synthesis from biocompatible precursors. L-tryptophan is an essential amino acid commonly known as the precursor for the neurotransmitters melatonin and serotonin and is also used as a fluorescent biomarker for proteins.[17,18] 4-Diethylamino salicylaldehyde is another biologically derived precursor frequently sourced in metallo-supramolecular chemistry for its strong metal binding potential as well as colourimetric and fluorescent properties.[19-24]

In addition, $H_2\mathbf{L}^I$ is analysed for its potential application as a fluorescent sensor for the detection of Al^{3+} in different biological, environments. Fluorescent analysis is used to demonstrate the potential of $H_2\mathbf{L}^I$ as a sensor for Al^{3+} and determine its LoD. Cell viability assays determine the suitability of $H_2\mathbf{L}^I$ to be used in biological application. Finally, $H_2\mathbf{L}^I$ is then applied to an array of biological environments to demonstrate its application in cellular and aqueous samples using fluorescent microscopy.

Table 2.1 Recent literature examples of nanomolar Al^{3+} fluorescence detecting probes.

Media	Selective	LoD (nM)	Fluorescence Shift	Effects on Cell Viability	Sensing Al^{3+} in Aqueous Samples	Sensing Al^{3+} in Cells	Reference
DMSO/H_2O (2:8, v/v), HEPES buffer (pH = 7.4)	Yes	637	None	Below 50% viability at 100 µM	N/A	Yes, in HepG2 (human liver) cells	1.
EtOH	Yes	20	None	N/A	N/A	N/A	14.
EtOH	Yes	40	None	N/A	N/A	N/A	14.
MeOH/H_2O (1:1, v/v)	Some fluorescence with Ga^{3+}	N/A	None	N/A	N/A	Yes, in HeLa (cervical cancer) cells	15.
DMSO	Yes	N/A	None	N/A	N/A	N/A	16.
DMSO	Yes	N/A	None	N/A	N/A	N/A	16.
MeOH/H_2O (1:9, v/v) acetate buffer (pH = 4.5)	Some fluorescence with Zn^{2+} and Cd^{2+}	'100 level'	None	N/A	N/A	N/A	25.
Ethanol	Yes	100	None	N/A	N/A	N/A	26.
MeOH, Tris buffer (pH = 7.0)	Competitively inhibited by Cu^{2+}	100	None	N/A	N/A	Yes, in HeLa (cervical cancer) cells	27.
EtOH/H_2O (1:99, v/v), HEPES (pH = 7.4)	Yes, no spectra of the screening of metals is given	8.8	None	N/A	N/A	Yes, in K562 (human leukaemia) cells	28.
EtOH/H_2O (1:99, v/v)	Some fluorescence with Zn^{2+} and Cd^{2+}	7380	None	N/A	N/A	N/A	29.
MeOH	Some fluorescence with Gd^{3+}	47.9	None	N/A	N/A	N/A	30.
MeOH	Some fluorescence with Cr^{3+}	82.8	None	N/A	N/A	N/A	30.
EtOH	Yes	'100' level	None	N/A	N/A	N/A	31.
MeOH/H_2O (4:1, v/v)	Some fluorescence with Fe^{3+} and Cr^{3+}	122	None	No effect on cell viability up to 40 µM	N/A	Yes, in HepG2 (human liver) cells	32.
MeOH/H_2O (4:1, v/v)	Yes	299	None	No effect on cell viability up to 40 µM	N/A	Yes, in HepG2 (human liver) cells	32.
EtOH	Yes	3	None	N/A	N/A	N/A	33.
EtOH	Yes	5	None	N/A	N/A	N/A	33.
MeOH/H_2O (1:1, v/v), HEPES (pH = 7.4)	No	4870	None	N/A	N/A	Yes, in HaCaT (human skin) cells	34.
H_2O	Yes	N/A	N/A	~50% viability at 100 µM	N/A	Yes, in SiHa (human cervix) cells	35.
EtOH	Yes	'100' level	None	N/A	N/A	N/A	36.
H_2O, GSH, HEPES (pH = 7.4)	Yes	61.5	From 533 nm to 405 nm	No effect on cell viability up to 500 µM	Yes, with limitations	Yes, 1321N1 (human brain) astrocytoma cells	This Work

2.3 Results and Discussion

2.3.1 Synthesis and Structure of $H_2\mathbf{L}^I$

$H_2\mathbf{L}^I$ was synthesised from the condensation of L-tryptophan and 4-diethylamino salicylaldehyde under reflux for 24 h in ethanol upon the presence of a catalytic amount of glacial acetic acid (Fig. 2.1). It was then characterised via ^{1}H NMR and ^{13}CNMR, ESI-HRMS, FT-IR, STA and P-XRD. SC-XRD demonstrates that $H_2\mathbf{L}^I$ crystallises in the orthorhombic space group with cell dimensions of *a* = 10.0820 (19) Å, b = 12.490 (2) Å, c = 15.926 (2) Å and α, β, γ = 90°.

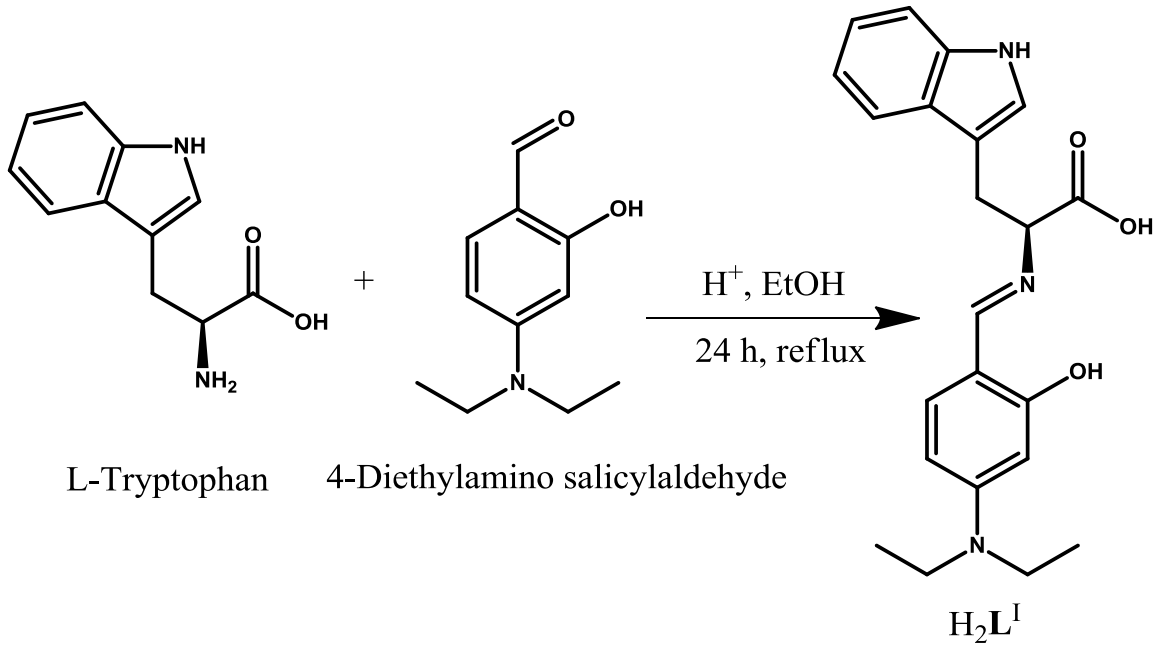

Figure 2.1 Synthesis of $H_2\mathbf{L}^I$.

2.3.2 Screening of Metal Cations

$H_2\mathbf{L}^I$ was initially characterised for its absorbance in a UV-visible (UV-vis) spectrophotometer spectrum indicating a peak maxima of 379 nm. $H_2\mathbf{L}^I$ was then scanned in the presence of various metal ions (2 eq.) indicating interaction with Al^{3+}, Fe^{3+}, Co^{2+}, Cu^{2+}, Zn^{2+} and Pb^{2+}. A fluorescent spectrum of $H_2\mathbf{L}^I$ was obtained when excited at 358 nm indicated a broad yet mild fluorescence peak at 533 nm (green) $H_2\mathbf{L}^I$ was then scanned in the

presence of various metal ions (2 eq.). A significant fluorescent enhancement response of ~24-fold is observed at 405 nm when $H_2\mathbf{L}^I$ is in the presence of Al^{3+} (2 eq.). A very weak fluorescent enhancement is also exhibited at 405 nm when in the presence of Zn^{2+} (2 eq.). Weak quenching of $H_2\mathbf{L}^I$ occurs at 533 nm when in the presence of Co^{2+} (2 eq.) and Fe^{3+} (2 eq.). Results demonstrate that $H_2\mathbf{L}^I$ has a significant and selective fluorescent response to Al^{3+} over other metal ions. $H_2\mathbf{L}^I$ also demonstrated its stability when bound to Al^{3+}. $H_2\mathbf{L}^I$ was observed slowly interacting with Al^{3+} as a function of time where fluorescence intensity plateaued at ~60 min and slowly depreciated likely due to damaged caused by the excitation source (Fig. 2.2).

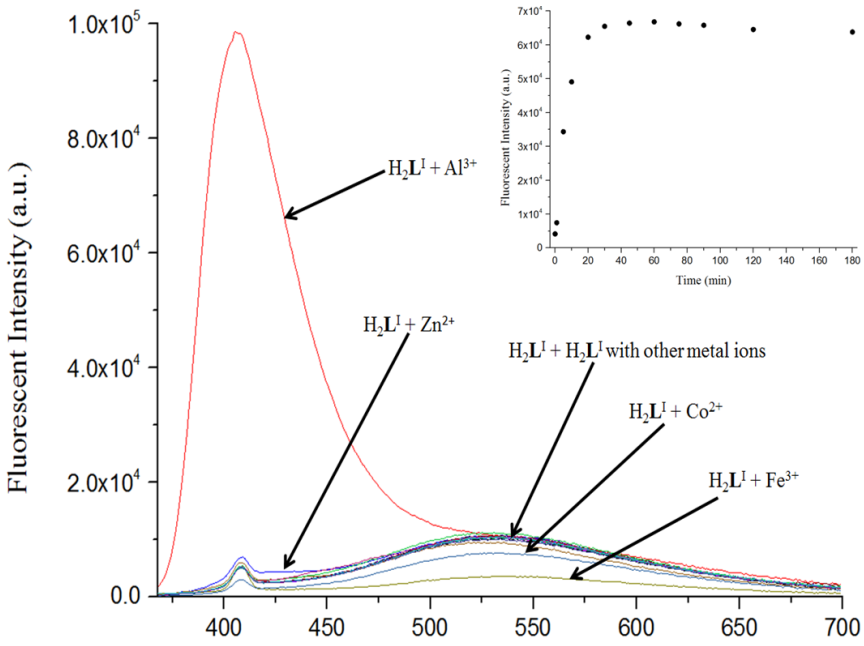

Figure 2.2 The fluorescence spectrum of $H_2\mathbf{L}^I$ (20 µM) in the presence of various metal ions (2 eq.) in 20 mM HEPES, 5 mM GSH water solution at pH = 7.4. Inset: A scatter plot of the fluorescence of $H_2\mathbf{L}^I$ (20 µM) in the presence of 2 eq. Al^{3+} in 20 mM HEPES, 5 mM GSH, Milli-Q water solution at pH = 7.4, as a function of time (0-180 min).

2.3.3 Naked Eye; Al^{3+} Detection

The contrast in colours between $H_2\mathbf{L}^I$, $H_2\mathbf{L}^I$ and Al^{3+}, and $H_2\mathbf{L}^I$ with other metal ions can be observed under the naked eye when excited with ultraviolet (UV) light. As observed $H_2\mathbf{L}^I$ emits light at a blue/ purple colour in the presence of Al^{3+} which is substantially different to the green colour emitted by $H_2\mathbf{L}^{I,}$ and $H_2\mathbf{L}^I$ in the presence of other metal ions

(Fig. 2.3). This pronounced fluorescent enhancement of $H_2\mathbf{L}^I$ at 405 nm when in the presence of Al^{3+} displays its high selectivity. It may be explained that the lone pair of electrons from the imine nitrogen atom of the Schiff base may evoke contributions to the photo-induced electron transfer (PET) phenomenon, which quench the fluorescence intensity of $H_2\mathbf{L}^I$. However, when $H_2\mathbf{L}^I$ chelates to the strongly bound, diamagnetic Al^{3+}, the quenching is inhibited and fluorescence is dramatically restored.[14,37-39]

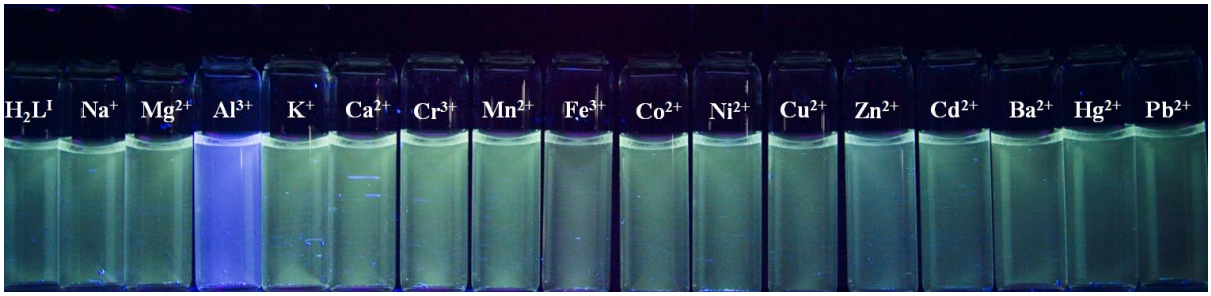

Figure 2.3 Detection of Al^{3+} by the naked eye using $H_2\mathbf{L}^I$ (20 μM) and $H_2\mathbf{L}^I$ in the presence of a series of metal cations (2 eq.) under UV light (365 nm) in 20 mM HEPES, 5 mM GSH, Milli-Q water solution at pH = 7.4

2.3.4 Competing Metal Ion

The fluorescence of $H_2\mathbf{L}^I$ and Al^{3+} in the coexistence of other metal ions was conducted in order to determine the ability of $H_2\mathbf{L}^I$ to sense Al^{3+} in the presence of potentially interfering ions. All samples were excited at 358 nm and fluorescent intensities were taken at 405 nm. $H_2\mathbf{L}^I$ and Al^{3+} in the coexistence of Cr^{3+}, Fe^{3+}, and Co^{2+} displayed some quenching, however, the fluorescent intensity was still increased by ~14-fold, ~3.2-fold and ~12.5-fold respectively, which are all still clearly detectable. All other metal ions observed very minimal or no quenching effects (Fig. 2.4).

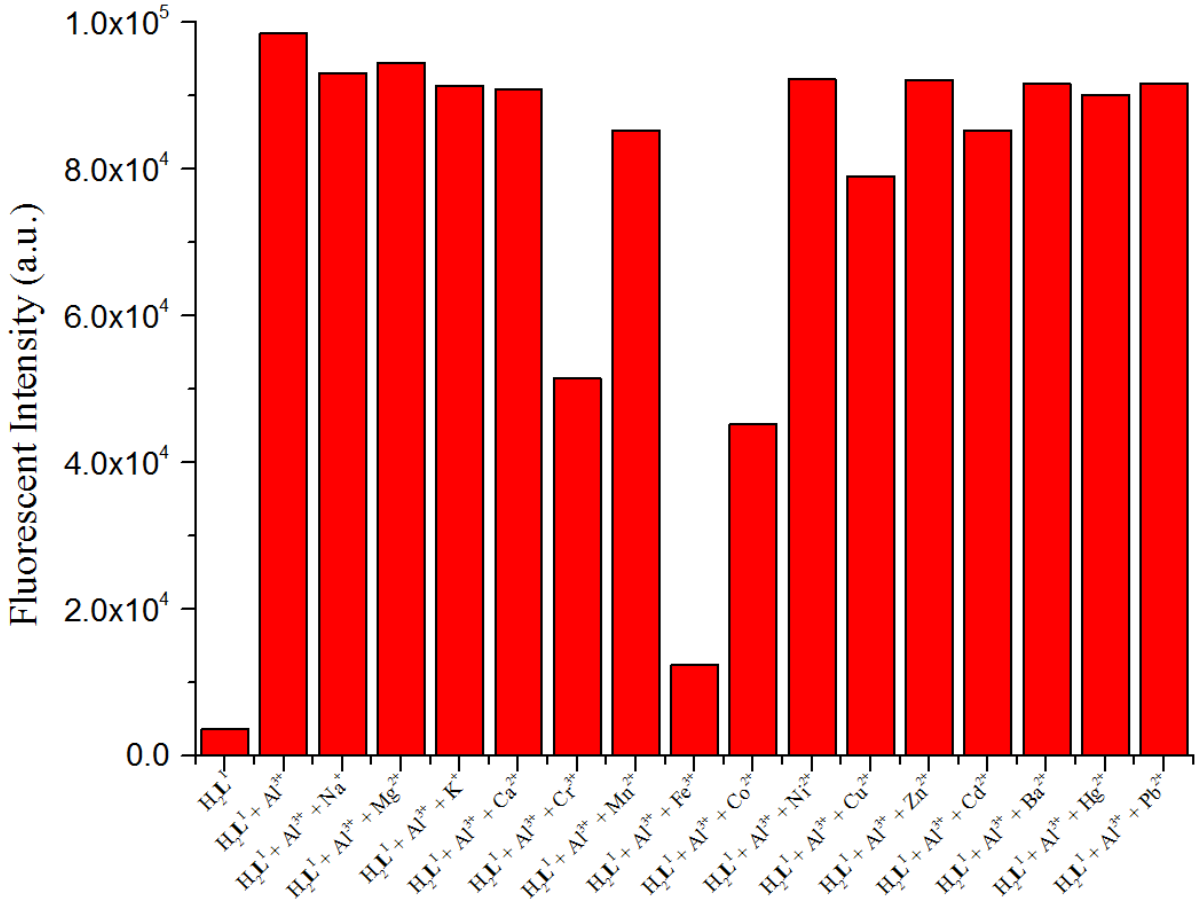

Figure 2.4 Fluorescence intensity of $H_2\mathbf{L}^I$ (20 µM) with Al^{3+} (2 eq.) under the coexistence of other metal cations (2 eq.) in 20 mM HEPES, 5 mM GSH, Milli-Q water solution at pH = 7.4. The samples were excited at 358 nm and fluorescent intensities were recorded at 405 nm.

2.3.5 Limit of Detection (LoD)

A metal titration of Al^{3+} into $H_2\mathbf{L}^I$ (20 µM) was conducted in methanol which determined the limit of detection (LoD) of $H_2\mathbf{L}^I$ where fluorescent intensities were recorded at 405 nm upon 358 nm excitation. Methanol was used alternately to the water, to reduce interference from the buffer solution, as well as, to prevent decomposition due to hydrolysis. Both of which would have inaccurately interfered with LoD and stoichiometry measurements. The titration determined a LoD of 61.5 nM and a limit of quantification (LoQ) of 204.9 nM determined by the equations 3σ/m and 10σ/m respectively. The metal titration also indicated a 1:2 ligand-to-metal stoichiometry (Fig. 2.5).

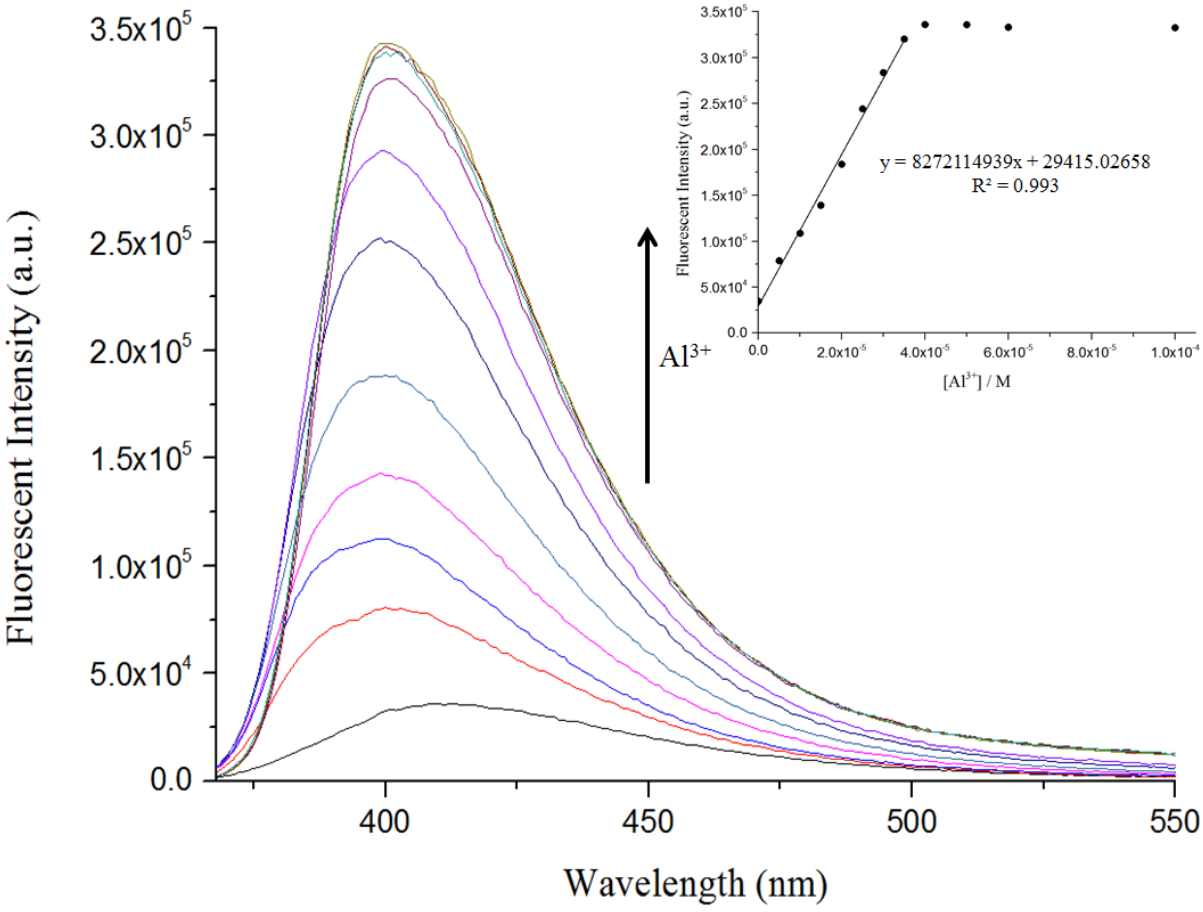

Figure 2.5 Fluorescence titration of $H_2\mathbf{L}^I$ upon addition of increasing amounts of Al^{3+} (0-5 eq.) in methanol. Inset: Fitting of the fluorescence titration curve of $H_2\mathbf{L}^I$ in methanol. LoD = 61.5 nM and LoQ = 204.9 nM determined by the following equations 3σ/m and 10σ/m respectively.

2.3.6 Job's plot

A Job's plot was conducted upon $H_2\mathbf{L}^I$ and Al^{3+} in methanol to a total concentration of 25 μM to determine the stoichiometry of the complex of $H_2\mathbf{L}^I$ with Al^{3+}. Fluorescent intensities were excited at 358 nm and recorded at 405 nm. The Job's plot molar intersect of 0.67 matched data from the MS and titration indicating a 1:2 ligand-to-metal stoichiometry (Fig. 2.6).

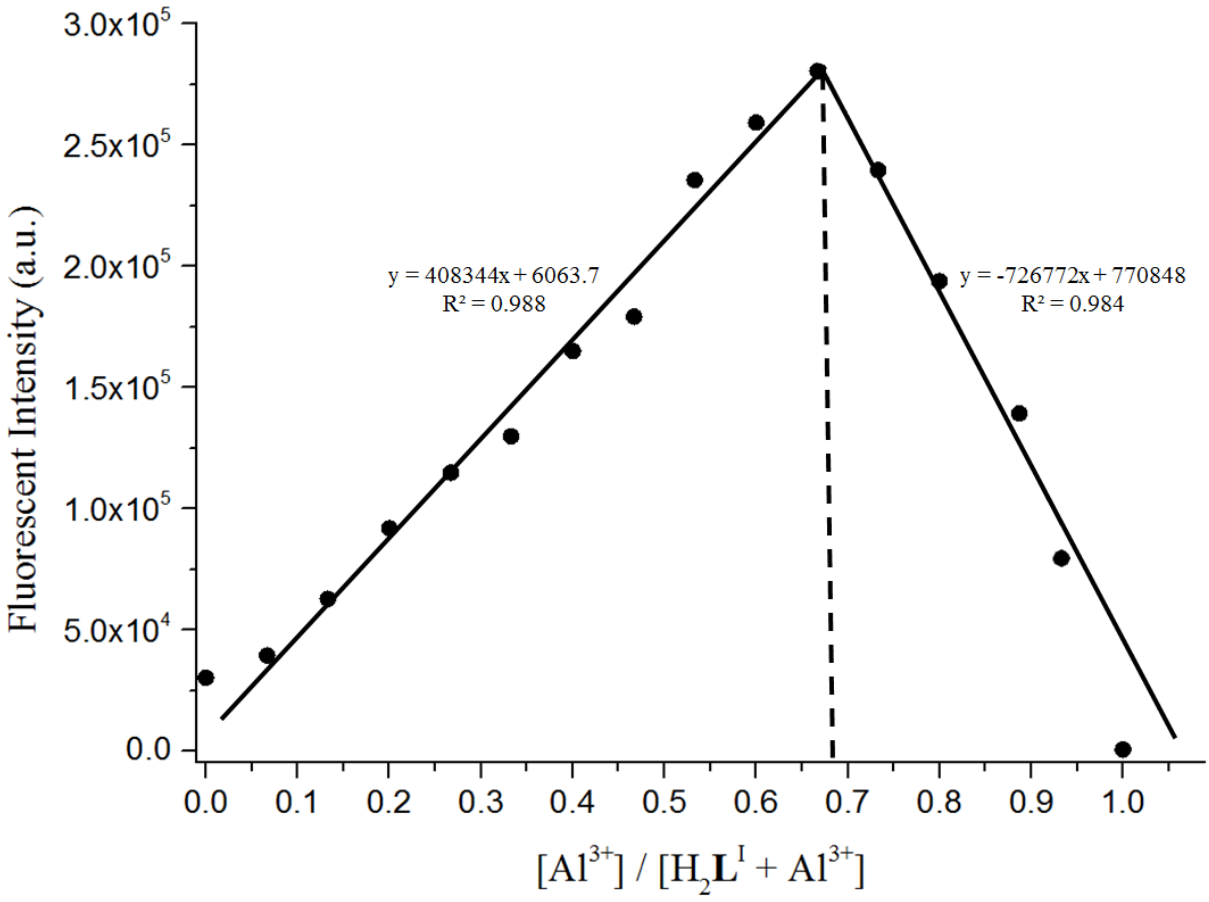

Figure 2.6 Job's plot of $H_2\mathbf{L}^I$ upon Al^{3+} in methanol at λ_{max} = 405 nm. Intersect of linear plots at molar fraction of 0.67, indicating a 1:2 ligand-to-metal stoichiometry.

2.3.7 Crystallographic Analysis

$H_2\mathbf{L}^I$ crystallises in the orthorhombic space group $P2_12_12_1$, with a single molecule present in the asymmetric unit (Fig. 2.7). Solution in a chiral space group indicates that only one isomer is present in the crystal lattice and upon inspection of the chiral carbon (C10) the S isomer was found to have solely crystallised. Intramolecular hydrogen bonding ($N_2\cdots O_3$ distance of 2.706 Å) between a protonated imine donor (N_2) and a phenolic acceptor (O_3) stabilises the phenolic, imine and carboxyl groups to lie in the same plane. The R-group of the L-tryptophan precursor is directed almost perpendicular to the plane mentioned above. This arrangement is stabilised by an extensive three-dimensional array of intermolecular hydrogen-bonding and edge-to-face π-π interactions (N1$\cdots$O1 – 2.930 Å, O1$\cdots$O3 – 2.510 Å and H00N$\cdots$C13-C14-C15-C16-C17-C18 centroid – 2.36 Å). (Fig. 2.8 and 2.9) Crystallographic details are also given. (Table 2.2)

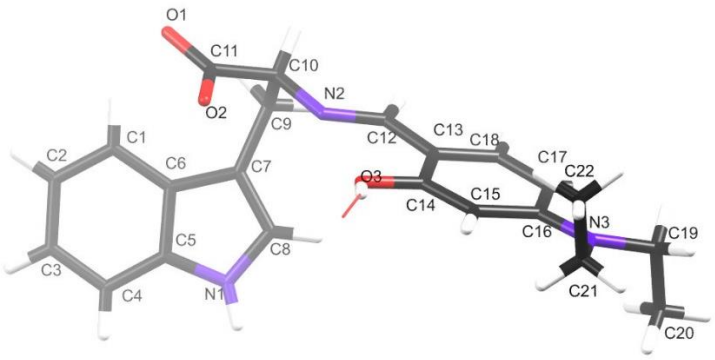

Figure 2.7 Schematic representation of the single S enantiomer present in the asymmetric unit of $H_2\mathbf{L}^{I}$ as observed by single crystal XRD experiments.

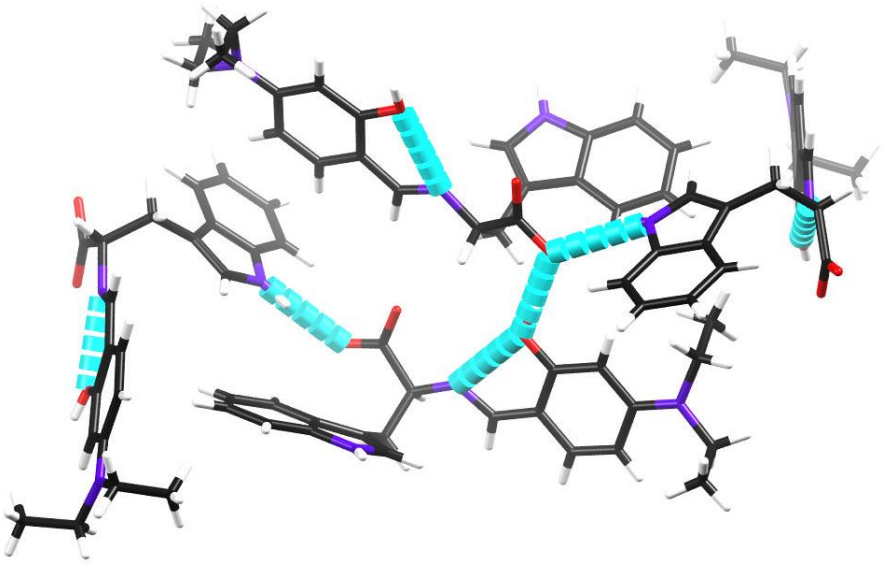

Figure 2.8 Schematic representation of the inter- and intramolecular hydrogen-bonding interactions present in the crystal lattice of $H_2\mathbf{L}^{I}$. Hydrogen-bonds are represented by blue thickened lines.

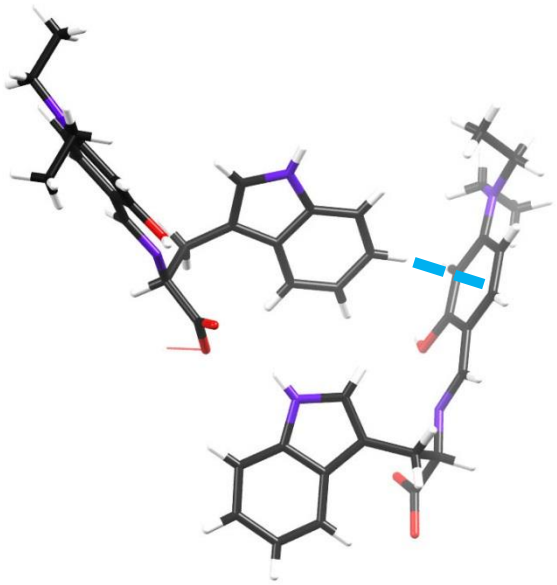

Figure 2.9 Schematic representation of the intermolecular edge-to-face π-π interactions present in the single crystal X-ray structure of $H_2\mathbf{L}^{I}$. Intramolecular contacts are represented by blue cut lines.

Table 2.2 Crystallographic details of $H_2\mathbf{L}^{I}$.

Empirical formula	$C_{22}H_{24}N_3O_3$
Formula weight	379.45
Temperature/K	100.55
Crystal system	orthorhombic
Space group	$P2_12_12_1$
a/Å	10.0820(19)
b/Å	12.490(2)
c/Å	15.926(2)
α/°	90
β/°	90
γ/°	90
Volume/Å^3	2005.5(6)
Z	4
ρ_{calc}g/cm^3	1.257
μ/mm^{-1}	0.085
F(000)	808.0
Radiation	MoKα (λ = 0.71073)
2Θ range for data collection/°	4.782 to 50.044
Index ranges	$-11 \leq h \leq 12$, $-14 \leq k \leq 14$, $-18 \leq l \leq 18$
Reflections collected	28096
Independent reflections	3530 [R_{int} = 0.1529, R_{sigma} = 0.0846]
Data/restraints/parameters	3530/0/257
Goodness-of-fit on F^2	1.070
Final R indexes [I>=2σ (I)]	R_1 = 0.0527, wR_2 = 0.1091
Final R indexes [all data]	R_1 = 0.0699, wR_2 = 0.1166
Largest diff. peak/hole / e Å^{-3}	0.43/-0.28
Flack parameter	-1(2)

2.4 Applications in Biological Systems

2.4.1 Detection of Al^{3+} in Different Water Samples

At a consistent concentration of $H_2\mathbf{L}^I$ (20 µM), water samples of Milli-Q, tap, Cattai Creek and Redbank Creek water were spiked with varying concentrations (0 - 200 µM) of Al^{3+} (Fig. 2.10). $H_2\mathbf{L}^I$ indicated strong fluorescent enhancement responses for Al^{3+} in Milli-Q at low concentration (10 – 20 µM), however, at higher concentrations (50 - 200 µM) this was reduced. This reduction of fluorescent intensity at higher concentrations may be due to self-quenching, interactions with the solvent or lower pH due to stock solutions of Al^{3+} being stored in acidic conditions to avoid oxide formation.[39] This same phenomenon occurs in tap, Cattai Creek and Redbank Creek at > 100 µM, 100 µM and 50 µM respectively. Overall, $H_2\mathbf{L}^I$ has the ability to sense for Al^{3+} in different water samples, despite some limitations which may be due to experimental error.

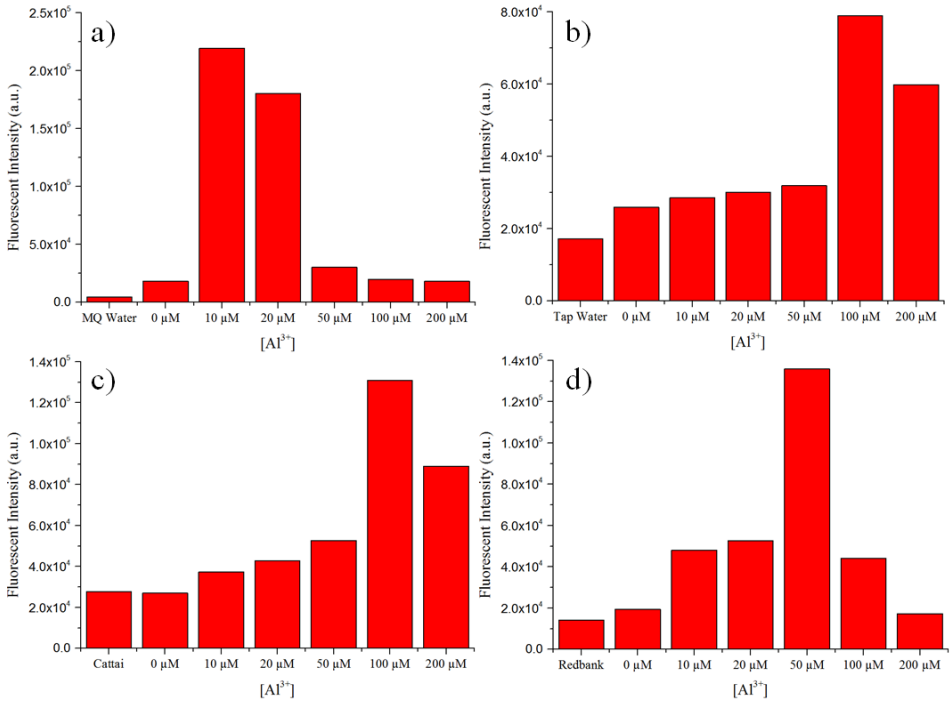

Figure 2.10 Fluorescent response of $H_2\mathbf{L}^I$ (20 µM) in the presence of different concentrations (0-200 µM) of spiked Al^{3+} in Milli-Q water (a.), tap water (b.), Cattai Creek water (c.) and Redbank Creek water (d.) as well as the fluorescence of the respective water samples with no treatment. The samples were excited at 358 nm and fluorescent intensities were recorded at 405 nm.

2.4.2 Cell Viability Assay

A cell viability assay of $H_2\mathbf{L}^I$ was conducted at varying concentrations using the MTT reductase method in 1321N1 astrocytoma cells to determine the suitability of $H_2\mathbf{L}^I$ for biological studies. Results indicated that up to 500 µM, $H_2\mathbf{L}^I$ exhibited no effect on cell viability implying the suitability of $H_2\mathbf{L}^I$ to potentially sense Al^{3+} in biological systems. Minor variations in cell viability are likely due to varying rates of cell growth and/ or pipetting error (Fig. 2.11).

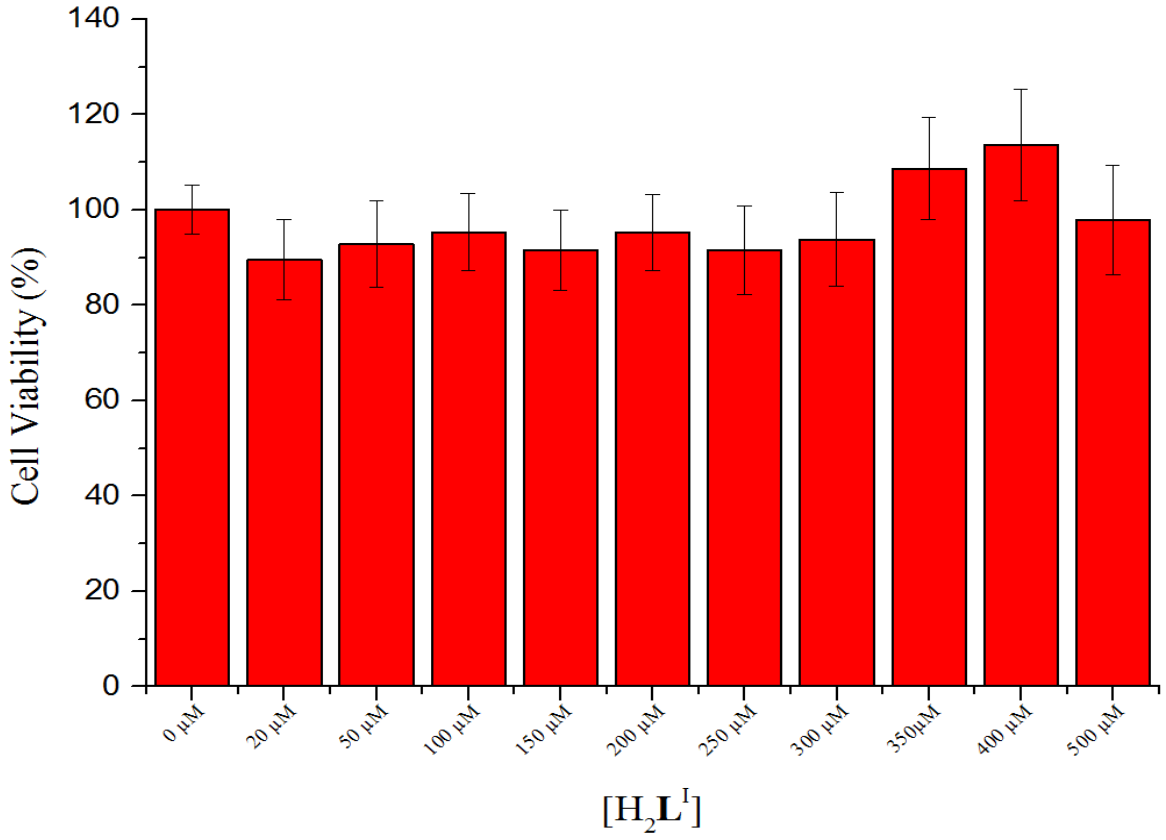

Figure 2.11 Percent (%) cell viability of 1321N1 astrocytoma cells treated with varying concentrations (0–500 µM) of $H_2\mathbf{L}^I$ for a 24 h incubation period, determined by an MTT reduction assay. Error bars = STD (n = 6).

2.4.3 Cellular Imaging

Fluorescent microscopy studies displayed the ability of $H_2\mathbf{L}^I$ to detect Al^{3+} in 1321N1 astrocytoma cells under UV light. In control groups of cells in 1: 6.67 (v/v) DMSO,

phosphate buffered saline (PBS) with no additional treatment, cells observed no fluorescent enhancement. Some fluorescence was observed in cells treated with $H_2\mathbf{L}^I$ (150 µM) 1:6.67 (v/v), however, this fluorescence was not significant. Upon addition of $H_2\mathbf{L}^I$ (150 µM), significant fluorescence enhancement occurs within the cell lines spiked with $AlCl_3$ (300 µM) 1: 6.67 (v/v). $H_2\mathbf{L}^I$ appears to detect Al^{3+} localised around the nuclear membrane of 1321N1 astrocytoma cells (Fig. 2.12).

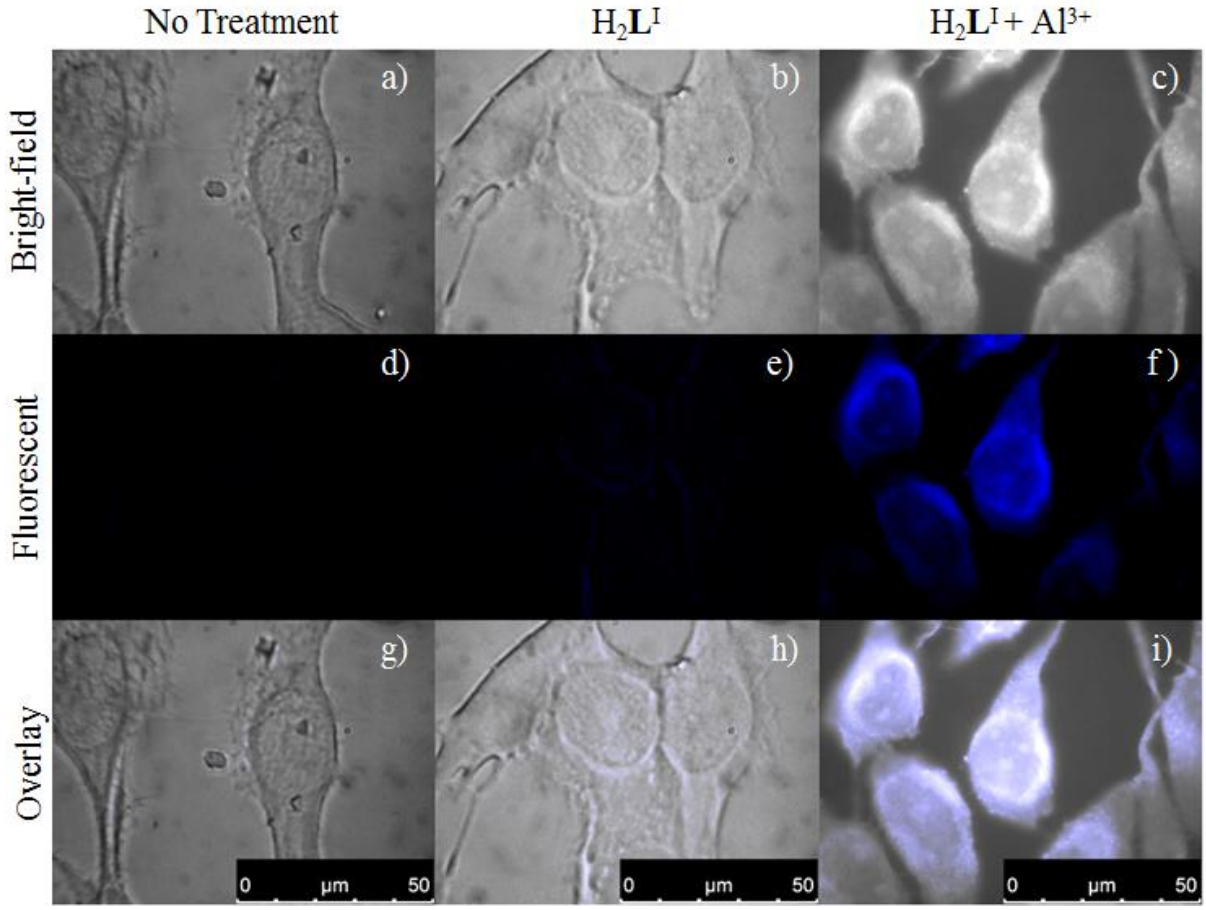

Figure 2.10 Fluorescent microscope images of 1321N1 astrocytoma cells. a), b) and c) indicate bright-field images of the cells. Images labelled d), e) and f) are the fluorescence images. Images g), h) and i) indicate overlay images. Cells labelled a), d) and g) are control groups of 1: 6.67 (v/v) DMSO, PBS buffer. Images b), e) and h) are cells spiked with 150 µM $H_2\mathbf{L}^I$ in 1: 6.67 (v/v) DMSO, PBS buffer. Images c), f) and i) indicate samples of 150 µM $H_2\mathbf{L}^I$ and 300 µM $AlCl_3$ in 1: 6.67 (v/v) DMSO, PBS buffer solution. All experiments were conducted under 100 x magnification and excited using UV light. Scale bars represents 50 µm.

2.5 Conclusion

$H_2\mathbf{L}^I$ was successfully synthesised and characterised. $H_2\mathbf{L}^I$ displayed a significant, selective, fluorescent enhancement response to Al^{3+} at 405 nm and $H_2\mathbf{L}^I$ itself indicated mild fluorescence at 533 nm. A stoichiometry of 1:2 ligand-to-metal ratio was indicated using metal titration, Job's plot as well as MS. The affinity of $H_2\mathbf{L}^I$ to Al^{3+} was tested in the coexistence of other metals and in different water samples indicating that $H_2\mathbf{L}^I$ can sense for Al^{3+} in various environments. Cell viability assays indicate that $H_2\mathbf{L}^I$ has no effect on cell viability and thus is suitable for cellular studies. $H_2\mathbf{L}^I$ was thereby tested for its potential fluorescent sensing capabilities in cellular conditions, using a fluorescent microscope. Here, $H_2\mathbf{L}^I$ indicated that it can sense intracellular Al^{3+} in 1321N1 astrocytoma cells.

$H_2\mathbf{L}^I$ was also compared to an array of different Schiff base fluorescent Al^{3+} sensors where it displayed significant specificity for detecting Al^{3+} in biological systems in contrast to other Schiff base sensors.

2.6 Experimental

2.6.1 Chemicals and Reagents

All chemicals, solvents and cell lines were purchased from commercial sources of commercial grade and used without further purification. All aqueous solutions were prepared with type I water from a Milli-Q water purification system. Metal standards were prepared from chloride (Na^+ , Mg^{2+}, Al^{3+}, K^+ , Ca^{2+}, Cr^{3+}, Mn^{2+}, Fe^{3+}, Co^{2+}, Ni^{2+}, Cu^{2+}, Zn^{2+}, Cd^{2+}, Ba^{2+} and Hg^{2+}) or nitrate (Pb^{2+}) salts of analytical grade, then standardised using literature complexometric titration methods with H_2Na_2EDTA.[40]

2.6.2 Instrumentations

Characterisation of $H_2\mathbf{L}^I$ was carried out using a range of techniques. ^1H and ^{13}C NMR spectra were measured on a Bruker DRX-300 NMR spectrometer. FT-IR measurements were conducted on a Bruker Vertex 70 spectrometer. Electrospray ionisation High-resolution mass spectra (ESI-HRMS) were collected using a Waters Xevo QToF quadrupole mass spectrometer with samples dissolved in methanol. Simultaneous thermal

analysis (STA) was undertaken on a Netzsch STA449 C Jupiter thermo-microbalance. An Edinburgh instruments FS5 Spectrofluorometer was used to conduct all fluorescent measurements. Agilent Cary 100 spectrophotometer was used to conduct the UV-vis experiments. Quartz cuvettes with a 1 cm optical path length were used for all fluorescent and colourmetric experiments. Fluorescent and colourimetric measurements, as well as cell viability assays, were graphed using Origin Pro 9.0. Scanning electron microscopy–electron dispersive spectroscopy (SEM-EDS) analysis was conducted on a Phenom XL instrument. Samples were run at 15 kV at medium vacuum without surface coating. Crystallographic data was collected using a Bruker kappa-II CCD diffractometer at 100 K, employing an IμS Incoatec Microfocus Source with Mo-Kα radiation. Data integration and reduction was undertaken with CrysAlisPro.40. The structures were solved by direct methods and the full-matrix least-squares refinements were carried out using a suite of SHELX programs via the Olex interface. Non-hydrogen atoms were refined anisotopically. Hydrogen atoms were included in idealised positions and refined using a riding model.

2.6.3 Synthesis of $H_2\mathbf{L}^I$

L-tryptophan (538 mg, 2.66 mmol) and 4-diethylamino salicylaldehyde (510 mg, 2.66 mmol) was dissolved in ethanol (25 mL) into a round bottom flask. Five drops of glacial acetic acid then added to the mixture. The mixture was then stirred under reflux at 90 °C for 24 h. The precipitate was then collected whilst hot using gravity filtration and wash thoroughly in methanol and then diethyl ether. The precipitate was left to dry overnight resulting was a brown/ yellow powder with a yield of ~70%. Crystals suitable for SC-XRD were grown by slow evaporation of $H_2\mathbf{L}^I$ (100 mg, 0.264 mmol) in 10 mL methanol. m.p. 221.6 °C, ^{1}HNMR: (300 MHz, DMSO-d_6 with TMS) δ 10.892 (s, 1H, NH), δ 7.979 (s, 1H, s, 1H, N=CH), δ 7.5624 (d, J = 7.62 Hz, 1H, ArH), δ 7.317 (d, J = 8.17 Hz, 1H, ArH), δ 7.0697-6.9227 (m, 4H, ArH), δ 6.1631 (d, 8.17 Hz, 1H, ArH), δ 6.0156 (s, 1H, ArH), δ 4.2428 (t, J = 5.73 Hz, 1H, CH), δ 3.3265 (q, J = 6.64, 4H, CH_2), δ 3.1499 (dd, J = 8.29, 1H, CH_2), δ 1.0672 (t, J = 6.64 Hz, 6H, CH_3). ^{13}CNMR: (75 MHz, DMSO-d_6 with TMS) δ 172.670, δ 164.455, δ 164.251, δ 151.285, δ 136.222, δ 135.976, δ 135.380, δ 127.089, δ 123.681, δ 120.799, δ 118.232, δ 111.245, δ 109.693, δ 107.339, δ 102.993, δ 97.093, δ 69.406, δ 43.727, δ 29.435, δ 12.435. ESI-HRMS: 380.1959 *m/z* $[H_2\mathbf{L}^I + H]^+$. FT-IR: 3675.67 cm^{-1} (N-H), 2971.83 cm^{-1} (O-H, carboxylic acid), 2900.91 cm^{-1} (O-H, phenol), 1593.70 cm^{-1} (O=C, carboxylic acid), 1520.28 cm^{-1} (C=N). UV−vis (1 cm optical path length, Milli-Q H_2O, 5 mM

glutathione (GSH), HEPES 20 mM, pH = 7.4): 20 μM $H_2\mathbf{L}^I$, λmax = 379 nm (abs = 0.830, ε = 41 500).

2.6.4 Synthesis of $[Al_2(\mathbf{L}^I)]^{4+}$

Potassium hydroxide (44.4 mg, 0.791 mmol) was dissolved in 10 mL methanol. $H_2\mathbf{L}^I$ (100 mg, 0.264 mmol) was completely dissolved in the mixture and filtered. The filtrate was then collected and stirred at 100 °C for 5 min. Aluminium chloride (70.4 mg, 0.528 mmol) was dissolved in 10 mL methanol and added dropwise to the mixture. The mixture was then stirred for a further 2 h and filtered. The filtrate was then collected and rotary evaporated until dry. 20 mL of Milli-Q water was added and the precipitate was collected via filtration and washed with ice-cold methanol and dried overnight resulting in a bright yellow powder at ~40% yield. ESI-HRMS: 482.1397 *m/z* $[Al_2(\mathbf{L}^I)]^{4+}$; $[Al_2(\mathbf{L}^I) + (OH)_3]^+$. FT-IR: 3675.74 cm^{-1} (N-H), 2971.99 cm^{-1} (O-H, carboxylic acid), 2900.91 cm^{-1} (O-H, phenol), 1593.65 cm^{-1} (O=C, carboxylic acid), 1520.28 cm^{-1} (C=N).

2.6.5 Fluorescent and UV−Vis Spectroscopy

A stock solution of $H_2\mathbf{L}^I$ (2 mM) was prepared in Milli-Q water at ~7.4 pH; this solution was used for all spectroscopic experiments except limited detection and Job's plot experiments which were conducted with a stock solution of $H_2\mathbf{L}^I$ (1 mM) in methanol. Other water-based solutions were trailed for limited detection and Job's plot experiments. However, due to interaction with an array of buffer solutions, as well as, decomposition of the ligand, pure methanol was used as a non-interfering media. Metal interaction experiments were carried out by aliquoting appropriate volumes of $H_2\mathbf{L}^I$ stock solution to 20 μM and metal ions to 40 μM (2 eq.) in mimicked intracellular conditions of 20 mM glutathione (GSH), 5 mM HEPES buffer at 7.4 pH in Milli-Q water to a total cuvette volume of 3 mL.[41] $AlCl_3$ was added as 2 eq. (40 μM), with competing metal ions also as 2 eq. (40 μM). Job's plot measurements were undertaken based upon literature protocols,[42,43] where $H_2\mathbf{L}^I$ and $AlCl_3$ were prepared in various molar ratios, with the combined concentration of both at 25 μM to a total cuvette volume of 3 mL. These molar ratio mixtures were prepared in a methanol to reduce external interactions with $H_2\mathbf{L}^I$ and $AlCl_3$. All fluorescent studies were excited at 358 nm, scanned from 368-700 nm and were prepared ~12 h prior to running, where they were stored in a dark, dry environment at standard laboratory conditions. Mimicked intracellular

solution studies were performed at slits of ex/em = 3/3 nm, whereas methanolic studies at ex/em = 1.25/1.25 nm.

2.6.6 Sensitivity Studies of $H_2\mathbf{L}^I$ with Al^{3+}

To determine the sensitivity of $H_2\mathbf{L}^I$ to Al^{3+} a metal titration approach was used in methanol, where samples of $H_2\mathbf{L}^I$ (20 μM) was prepared with a various equivalents of $AlCl_3$. The samples were left to incubate in a dark, dry environment at standard laboratory conditions for ~12 h prior to run time. The limit of detection (LoD) and limit of quantification (LoQ) were calculated using 3σ/m and 10σ/m, respectively, where σ is the standard deviation of a blank solution and m is the slope of the linear plot obtained.[44] For the standard deviation (σ) determination, we took 10 repeated spectra measurements of a blank solution ($H_2\mathbf{L}^I$ solution in the same conditions used for measurements but without any addition of $AlCl_3$) and calculated the standard deviation for the fluorescent values at 405 nm, obtaining a value of σ = 168.5.

2.6.7 Cell Culturing

Human 1321N1 cell line (1321N1 astrocytoma; purchased from Sigma-Aldrich/ ATCC) were grown in Dulbecco's modified eagle medium (DMEM) supplemented with 10% fetal bovine serum (FBS) and antibiotics (penicillin-100 μg ml^{-1}; streptomycin-50 μg ml^{-1}). Cells were cultured at 37 °C in a 95% air, 5% CO_2 incubator.

2.6.8 Cell Viability Assay

1321N1 astrocytoma cells were seeded into a 96-well plate and filled with complete DMEM to a total volume of 190 μL containing 10,000 cells each and then incubated (37 °C, CO_2 5%) for 24 h. Stock solutions of $H_2\mathbf{L}^I$ (10 mM, 5 mM, 1.25 mM) were prepared in sterile Milli-Q water at 7.4 pH. 10 μL of sextet concentration of 0, 20, 50, 100, 150, 200, 300, 350, 400 and 500 μM of $H_2\mathbf{L}^I$ were prepared into the 96 well plates and incubated for 24 h. 50 μL of 5 mg/mL 3-(4,5-dimethylthiazol-2-yl)-2,5-diphenyltetrazolium bromide (MTT) was added into each well and the cells were then left to incubate (37 °C, CO_2 5%) for a further 2 h. The media was decanted from each well and 100 μL of DMSO was added into each well to

solubilise the formazan crystals. The 96 plate well was gently agitated before optical absorbance was measured at 595 nm using the BMG FLUOstar OPTIMA microplate reader. The values were then calculated as the mean ± standard deviation errors of six independent experiments. The cell viability was expressed as the optical density ratio of the treatment compared to control samples.

2.6.9 Detection of Al^{3+} in Different Water Samples

Water samples were taken from type I water from a Milli-Q water purification system, tap water from Parramatta Council, Sydney, NSW, Australia. River water samples were collected from still river water samples of Cattai Creek, The Hills Shire Council, Sydney, NSW, Australia and Redbank Creek, Hawkesbury Shire Council, Sydney, NSW, Australia. Blank water samples were initially measured as controls. $H_2\mathbf{L}^I$ (20 µM) was added into varying spiked samples of $AlCl_3$ (0, 10, 20, 50, 100 and 200 µM) to a total volume of 3 mL in each of the water samples. All water samples were excited at 358 nm and data was collected at 405 nm with slit sizes of ex/em = 3/3 nm.

2.6.10 Cell Imaging

1321N1 astrocytoma cells were viewed under a Leica DMRBE Trinocular Research Microscope with all parameters according to table 2.3. Samples of live 1321N1 astrocytoma, 1321N1 astrocytoma upon addition of $H_2\mathbf{L}^I$ (150 µM), and $H_2\mathbf{L}^I$ (150 µM) in the coexistence with $AlCl_3$ (300 µM) were prepared on separate slides, excited under a UV lamp and viewed with an objective lens at 100 x magnification, 50 µm. All cellular environments were incubated in DMSO, PBS buffer (1: 6.67 v/v ratio respectively) at 37 °C, CO_2 (5%) for 30 minutes each, prior to assessment. All images captured were processed using LAS AF software.

Table 2.3 Parameters used for all fluorescent cell imaging studies of 1321N1 astrocytoma cells.

Dimension	Logical Size	Physical Length	Physical Origin	Voxel Size
X	1296 pixels	97.13 µm	0.00 µm	0.075 µm
Y	966 pixels	72.38 µm	0.00 µm	0.075 µm
LUT Name	**Exposure Time**	**Gain**	**Resolution XY**	**Resolution Z**
Grayscale	820.025 ms	5.6	0.258 µm	0.494 µm
Blue	688.517 ms	4.8	0.258 µm	0.494 µm

2.7 Acknowledgments

The authors thank the Western Sydney University (WSU) Advance Material Characterisation Facility and the WSU Mass Spectrometry Facility for instrumental access. D.J.W. also thanks WSU for their postgraduate research funding.

2.8 Conflicts of Interest

There are no conflicts to declare.

2.9 Reference List

1. K. Mal *et al.* Dihydroindeno[1,2-b]pyrroles: new Al3+ selective off–on chemosensors for bio-imaging in living HepG2 cells. *Org Biomol Chem* **16,** 5920–5931 (2018).
2. C. Exley. A biogeochemical cycle for aluminium? *J. Inorg. Biochem.* **97,** Journal of Inorganic Biochemistry (2003).
3. K. Tennakone, S. Wickramanayake & C. A. N. Fernando. Aluminium contamination from fluoride assisted dissolution of metallic aluminium. *Environ. Pollut.* **49,** 133–143 (1988).
4. X. Shi-Gang, S. Li-Xin, Z. Rong-Gen & H. Xing-Fang. Properties of aluminium oxide coating on aluminium alloy produced by micro-arc oxidation. *Surf. Coat. Technol.* **199,** 184–188 (2005).
5. K. R. Koch, M. A. Pougnet, S. de Villiers & F. Monteagudo. Increased urinary excretion of Al after drinking tea. *Nature* **12,** 122 (1988).
6. B. O. Rosseland, T. D. Eldhuset & M. Staurnes. Environmental effects of aluminium. *Environ. Geochem. Health* **12,** 17–27 (1990).
7. S. J. Zheng. Crop production on acidic soils: overcoming aluminium toxicity and phosphorus deficiency. *Ann. Bot.* **106,** 183–184 (2010).
8. S. J. Carr, G. S. P. Ritchie & W. M. Porter. A soil test for aluminium toxicity in acidic subsoils of yellow earths in Western Australia. *Aust. J. Agric. Res.* **42,** 875–892 (1991).
9. V. B. Gupta *et al.* Aluminium in Alzheimer's disease: are we still at a crossroad? *Cell. Mol. Life Sci.* **62,** 143–158 (2005).
10. A. Campbell. The potential role of aluminium in Alzheimer's disease. *Nephrol. Dial. Transplant.* **17,** 17–20 (2002).
11. J. P. Landsberg, B. McDonald & F. Watt. Absence of aluminium in neuritic plaque cores in Alzheimer's disease. *Nature* **360,** 65–68 (1992).
12. T. P. Flaten. Aluminium as a risk factor in Alzheimer's disease, with emphasis on drinking water. *Brain Res. Bull.* **55,** 187–196 (2001).
13. J. R. Lakowicz. Principles of Fluorescence Spectroscopy. 3rd ed. Springer Science and Business Media; 2013.
14. J.-C. Qin, X.-Y. Cheng, R. Fang, M.-F. Wang, Z.-Y. Yang, T.-R. Li, et al. Two Schiff base fluorescent sensors for selective sensing of aluminum (III): Experimental and computational studies. *Spectrochim. Acta, Part A.***152**, 352–357 (2016).
15. S. Kim *et al.* Salicylimine-Based Fluorescent Chemosensor for Aluminum Ions and Application to Bioimaging. *Inorg. Chem.* **51**, 3597–3602 (2012).
16. D. Maity & T. Govindaraju. Naphthaldehyde–Urea/Thiourea Conjugates as Turn-On Fluorescent Probes for Al3+ Based on Restricted C=N Isomerization. *Eur. J. Inorg. Chem.* **2011**, 5479–5485 (2011).
17. J. T. Vivian & P. R. Callis. Mechanisms of Tryptophan Fluorescence Shifts in Proteins. *Biophysical Journal* **80**, 2093–2109 (2001).
18. S. J. Murch, S. KrishnaRaj & P. K. Saxena. Tryptophan is a precursor for melatonin and serotonin biosynthesis in in vitro regenerated St. John's wort (Hypericum perforatum L. cv. Anthos) plants. *Plant Cell Reports* **19**, 698–704 (2000).
19. N. Narayanaswamy & T. Govindaraju. Aldazine-based colorimetric sensors for Cu2+ and Fe3+. *Sensors and Actuators B: Chemical* **161**, 304–310 (2012).
20. K. K. Upadhyay & A. Kumar. Pyrimidine based highly sensitive fluorescent receptor for Al3+ showing dual signalling mechanism. *Org. Biomol. Chem.* **8**, 4892–4897 (2010).
21. D. Maity & T. Govindaraju. Highly Selective Visible and Near-IR Sensing of Cu2+ Based on Thiourea–Salicylaldehyde Coordination in Aqueous Media. *Chem. Eur. J.* **17**, 1410 – 1414 (2011)

22. D. J. Fanna *et al.* Ultrasensitive Colorimetric and Ratiometric Detection of Cu2+: Acid–Base Properties, Complexation, and Binding Studies. *ACS Omega* **3**, 10471−10480 (2018).
23. K. J. Howard-Smith *et al.* Syntheses and Structure Investigations of 3d Transition Metal Complexes with a Flexible N4O2-Donor Hexadentate Schiff-Base Ligand. *Aust. J. Chem* **70**, 581–587 (2017).
24. A. R. Craze *et al.* Synthesis and characterisation of new tripodal lanthanide complexes and investigation of their optical and magnetic properties. *Dalton Trans.* **46**, 12177–12184 (2017).
25. X.-H. Jiang *et al.* 8-Hydroxyquinoline-5-carbaldehyde Schiff-base as a highly selective and sensitive Al3+ sensor in weak acid aqueous medium. *Inorganic Chemistry Communications* **14**, 1224–1227 (2011).
26. Z.-C. Liao, Z.-Y. Yang, Y. Li, B.-D. Wang & Q.-X. Zhou. A simple structure fluorescent chemosensor for high selectivity and sensitivity of aluminum ions. *Dyes and Pigments* **97**, 124–128 (2013).
27. J. Y. Noh *et al.* Solvent-dependent selective fluorescence assay of aluminum and gallium ions using julolidine-based probe. *Dyes and Pigments* **99**, 1016–1021 (2013).
28. L. Wang *et al.* A selective, cell-permeable fluorescent probe for Al3+ in living cells. *Org. Biomol. Chem.* **8**, 3751–3757 (2010).
29. N. Lashgari, A. Badiei & G. M. Ziarani. A Fluorescent Sensor for Al(III) and Colorimetric Sensor for Fe(III) and Fe(II) Based on a Novel 8-Hydroxyquinoline Derivative. *J. Fluoresc.* **26**, 1885–1894 (2016).
30. S. K. Shoora, A. K. Jain & V. K. Gupta. A simple Schiff base based novel optical probe for aluminium (III) ions. *Sens. Actuators B* **216**, 86–104 (2015).
31. Z.-C. Liao, Z.-Y. Yang, Y. Li, B.-D. Wang & Q.-X. Zhou. A simple structure fluorescent chemosensor for high selectivity and sensitivity of aluminum ions. *Dyes Pigments* **97**, 124–128 (2013).
32. X. Gan *et al.* Two analogously structural triphenylamine-based fluorescent"off-on" probes for Al3+via two distinct mechanisms and cell imagingapplication. *Sens. Actuators B Chem.* **239**, 642–651 (2017).
33. B. Ghanbari & M. Zarepour-jevinani. Promotional effect of macrocyclization in O2Nxnaphtha-aza-crownmacrocyclic ligands on fluorescence chemosensing of Al(III). *J. Lumin.* **205**, 219–227 (2019).
34. K. Velmurugan *et al.* Dual Functional Fluorescent Chemosensor for Discriminative Detection of Ni2+ and Al3+ Ions and Its Imaging in Living Cells. *ACS Sustain. Chem Eng* **6**, 16532−16543 (2018).
35. R. Dwivedi *et al.* Intracellular application and logic gate behavior of a 'turn off-on-off' type probe for selective detection of Al3+ and F− ions in pure aqueous medium. *Sens. Actuators B Chem.* **258**, 881–894 (2018).
36. C.-R. Li, J. -C. Qin, G.-Q. Wang, B.-D. Wang & Z.-Y. Yang. A novel pyrazine derivative as a "turn on" fluorescent sensor for the highly selective and sensitive detection of Al3+. *Anal Methods* **7**, 3500–3505 (2015).
37. Z.-C. Liao, Z.-Y. Yang, Y. Li, B.-D. Wang & Q.-X. Zhou. A simple structure fluorescent chemosensor for high selectivity and sensitivity of aluminum ions. *Dyes and Pigments* **97**, 124–128 (2013).
38. D. Escudero. Revising Intramolecular Photoinduced Electron Transfer (PET) from First-Principles. *Acc Chem Res* **49,** 1816−1824 (2016).
39. L. D. Lavis & R. T. Raines. Bright Ideas for Chemical Biology. *ACS Chem Biol* **3,** 142–155 (2018).
40. G. Schwarzenbach & H. Flaschka. *Complexometric Titrations*. (H. M. N. H, 1969).
41.H. Y. Au-Yeung, E. J. New & C. J. Chang. A selective reaction-based fluorescent probe

for detecting cobalt in living cells. *Chem. Commun.* **48**, 5268–5270 (2012).
42. P. Job. Formation and Stability of Inorganic Complexes in Solution. *Ann. Chim.* **9**, (1928).
43. J. S. Renny, L. L. Tomasevich, E. H. Tallmadge & D. B. Collum. Applications of Job Plots to the Study of Molecular Associations in Organometallic Chemistry. *Angew. Chem., Int. Ed.* **52**, 11998−12013 (2013).
44. B. Magnusson. The Fitness for Purpose of Analytical Methods: A Laboratory Guide to Method Validation and Related Topics; Eurachem, 2014. in (Eurachem, 2014).

2.10 Supplementary Information

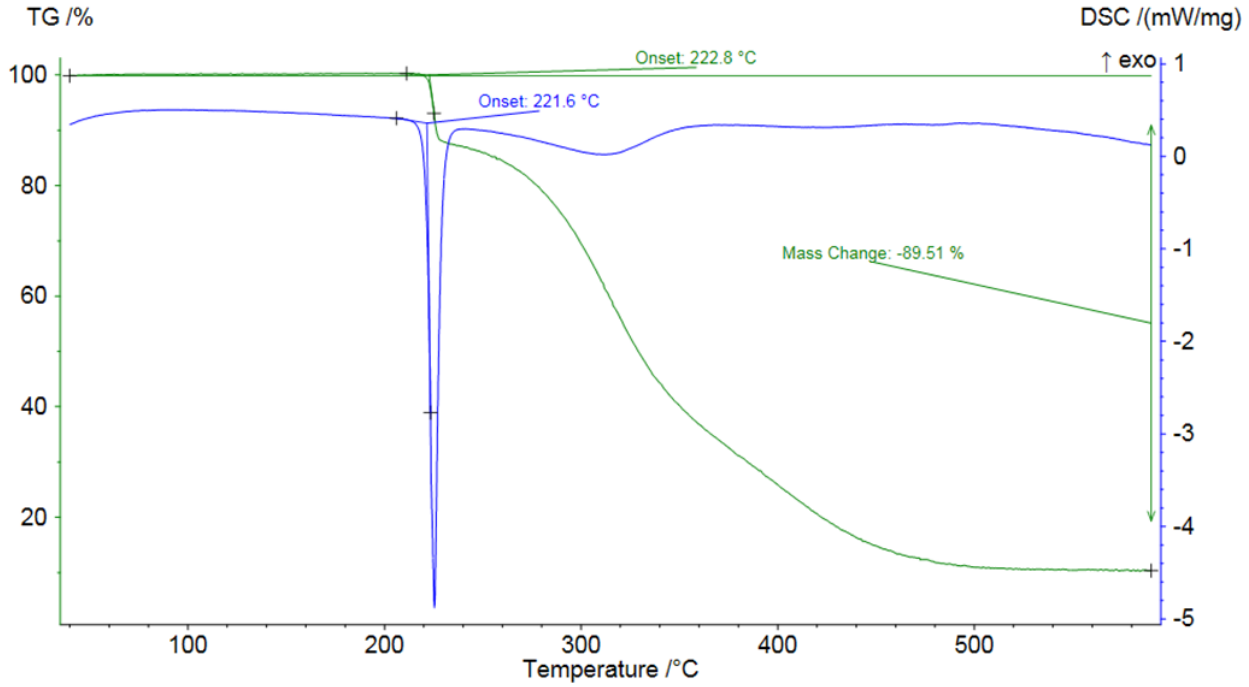

Figure S2.1 The STA data of $H_2\mathbf{L}^{I}$ (40-590 °C).

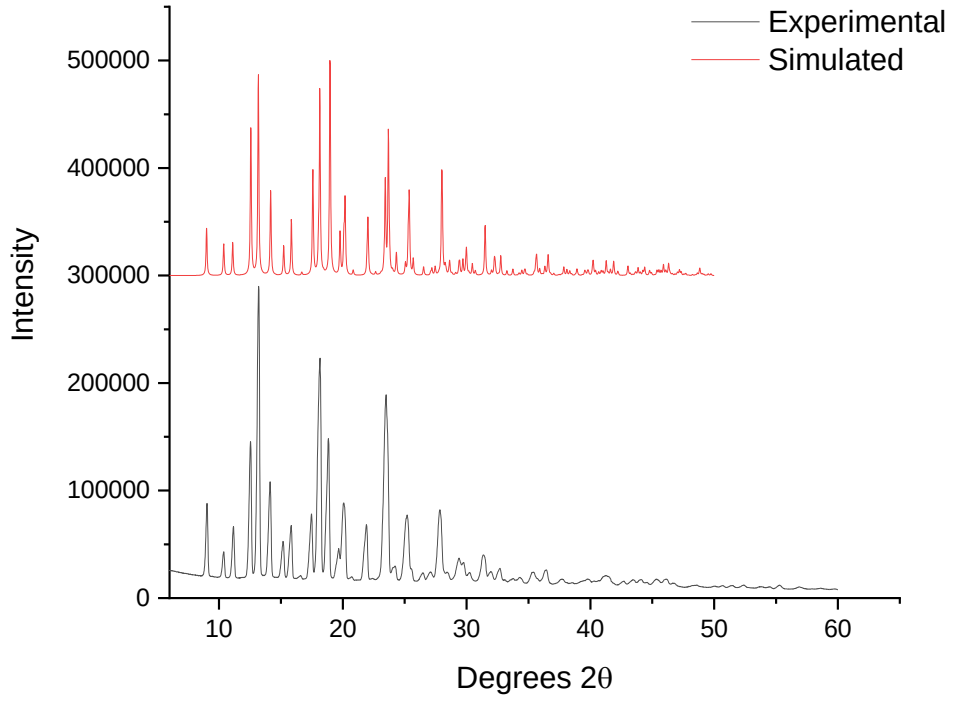

Figure S2.2 Simulated (top) vs experimental (bottom) powder X-ray diffraction data of $H_2\mathbf{L}^{I}$, indicating phase purity of the bulk powder sample with the measure single crystal diffraction data.

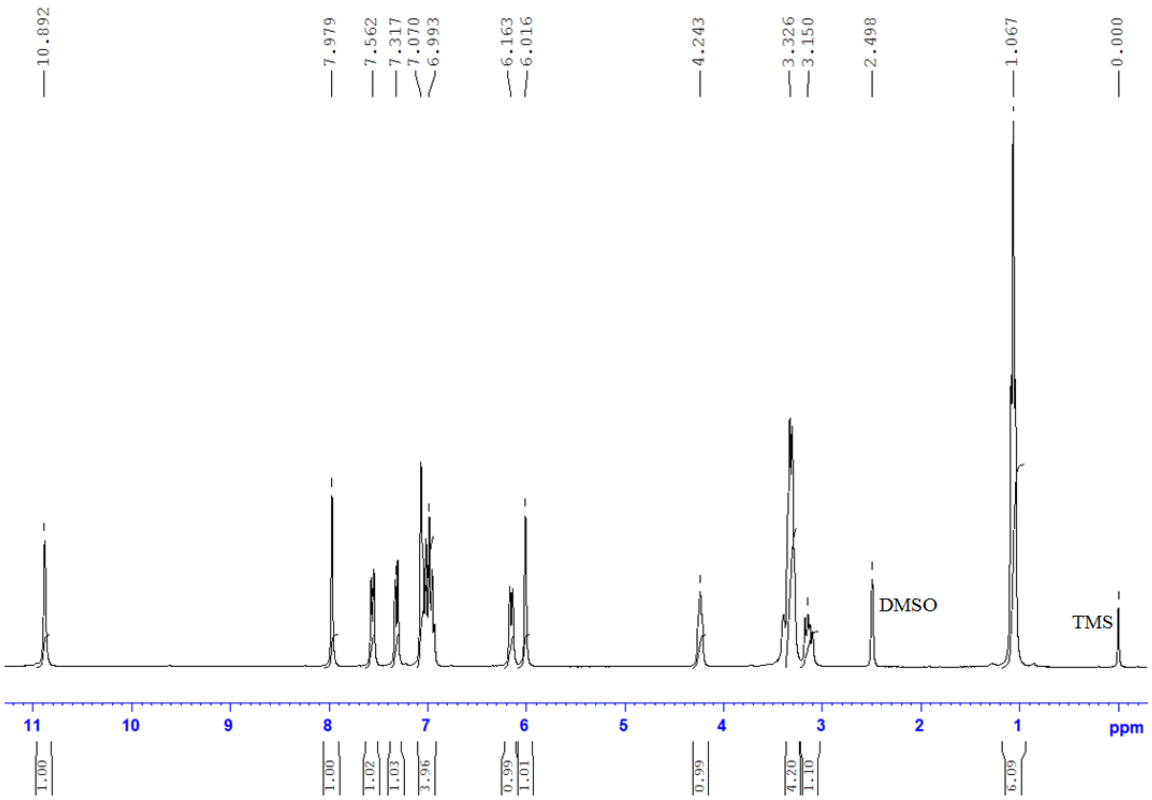

Figure S2.3 The ^{1}HNMR spectrum of $H_2\mathbf{L}^{I}$ in DMSO-d_6.

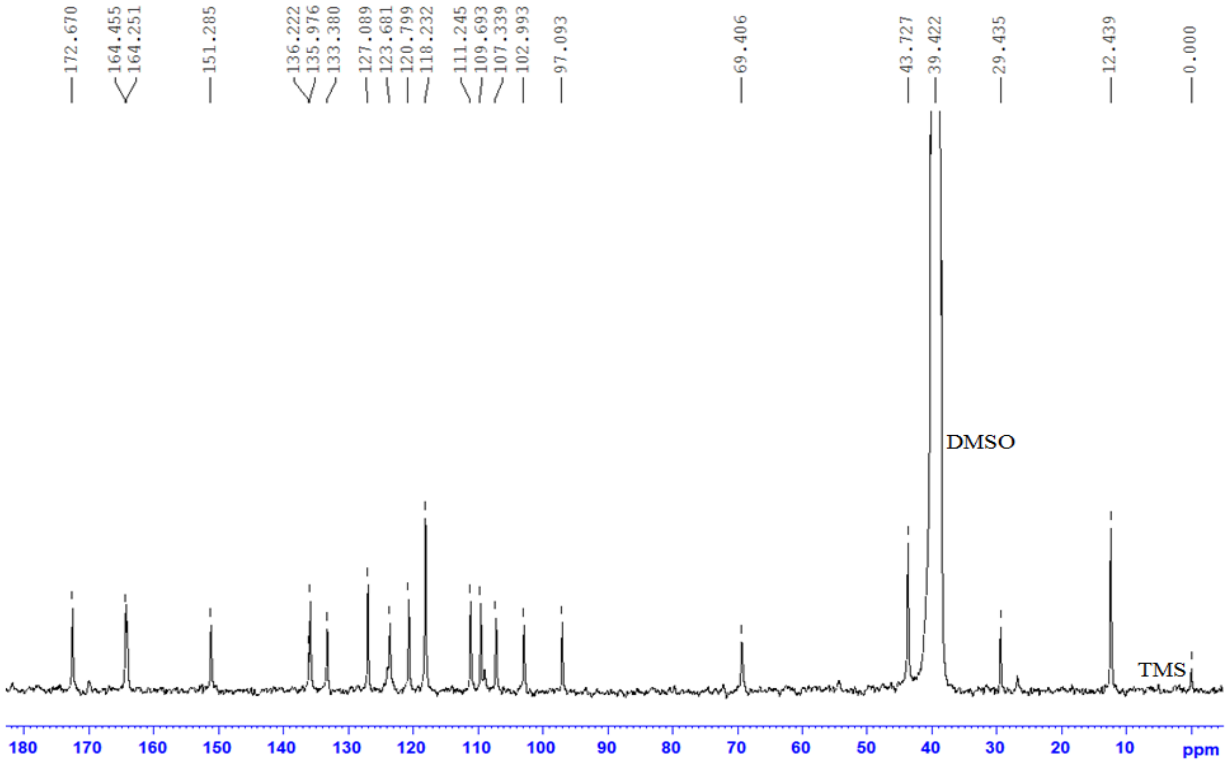

Figure S2.4 The ^{13}CNMR spectrum of $H_2\mathbf{L}^{I}$ in DMSO-d_6.

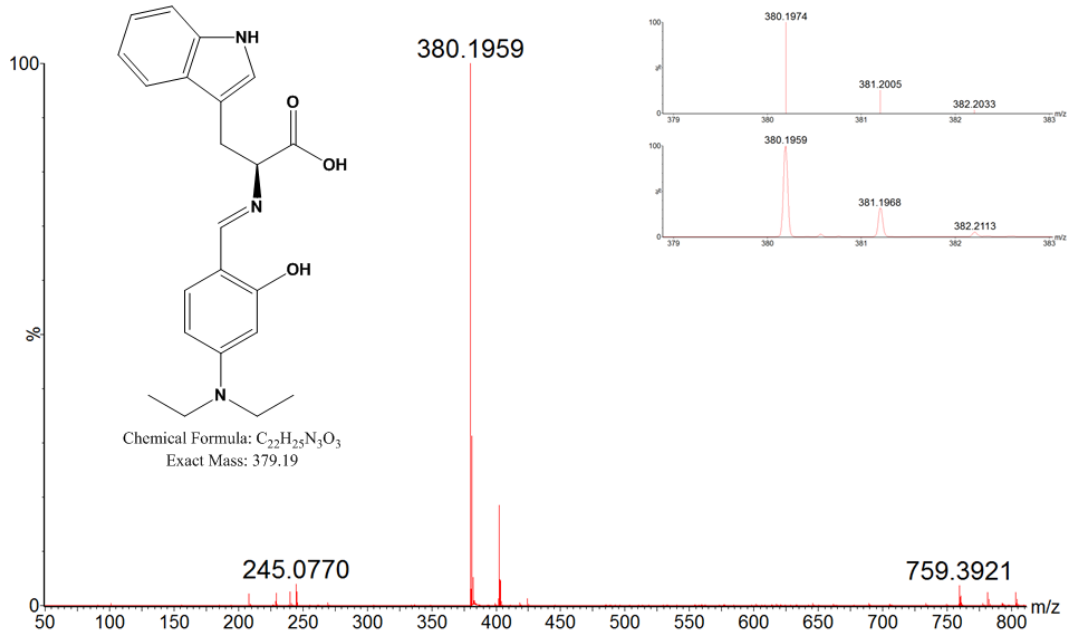

Figure S2.5 ESI-HRMS of $H_2\mathbf{L}^I$;$[H_2\mathbf{L}^I + H]^+$ in methanol from 50 – 800 *m/z*. Inset: On the left, the structure and molar mass of $H_2\mathbf{L}^I$. On the right, the predicted (above) and experimental (bellow) isotopic patterns of $[H_2\mathbf{L}^I + H]^+$.

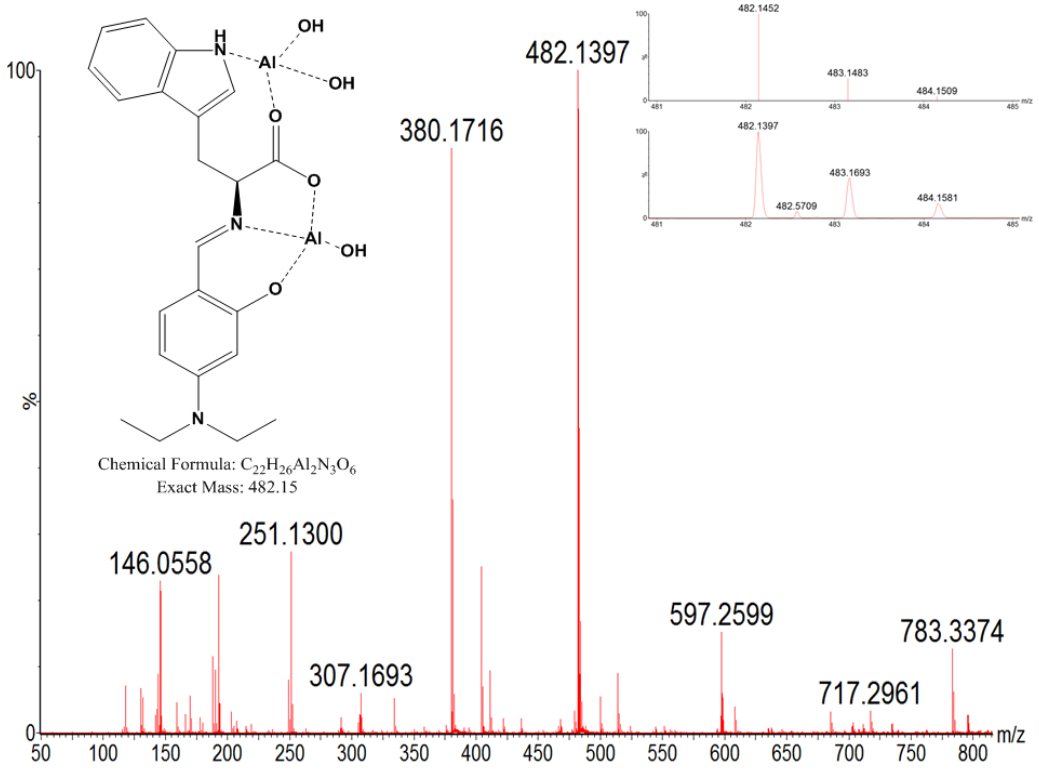

Figure S2.6 ESI-HRMS of $[Al_2(\mathbf{L}^I)]^{4+}$; $[Al_2(\mathbf{L}^I) + (OH)_3]^+$ in methanol from 50 – 800 *m/z*. Inset: On the left, the predicted structure and molar mass of $[Al_2(\mathbf{L}^I)]^{4+}$. On the right, the predicted (above) and experimental (bellow) isotopic patterns of $[Al_2(\mathbf{L}^I) + (OH)_3]^+$.

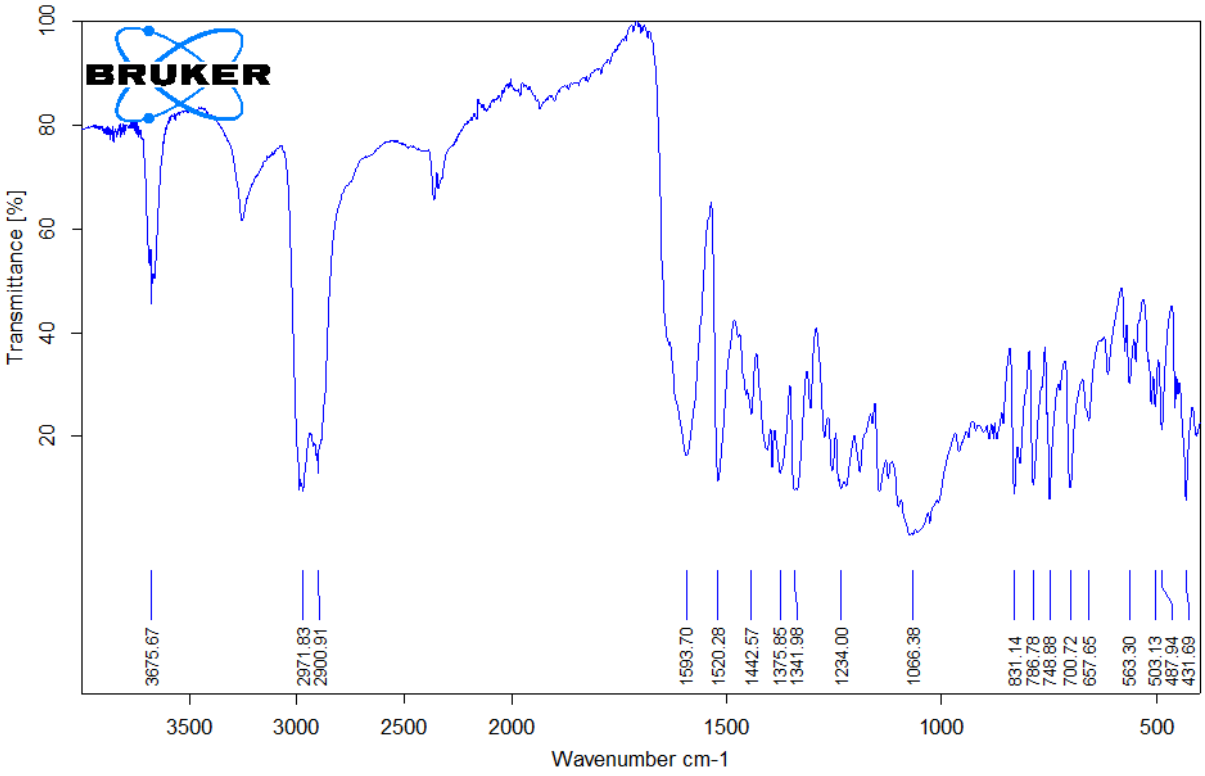

Figure S2.7 FT-IR spectrum of $H_2\mathbf{L}^{I}$.

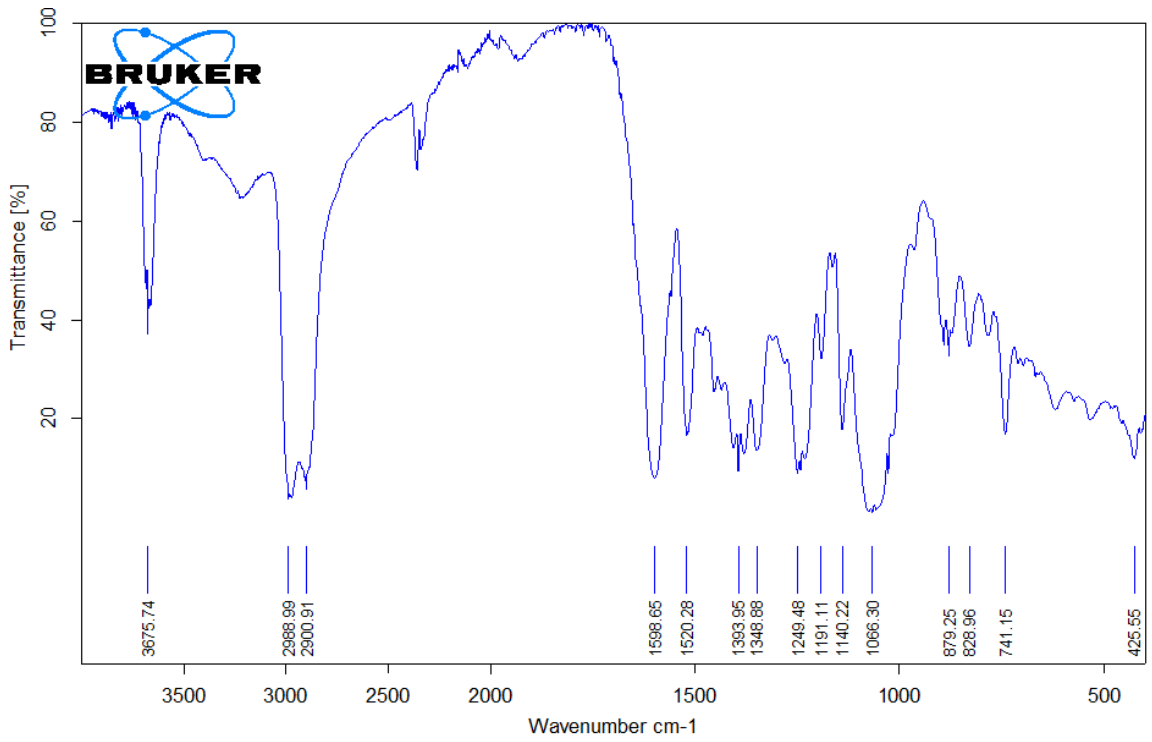

Figure S2.8 FT-IR spectrum of $[Al_2(\mathbf{L}^{I})]^{4+}$.

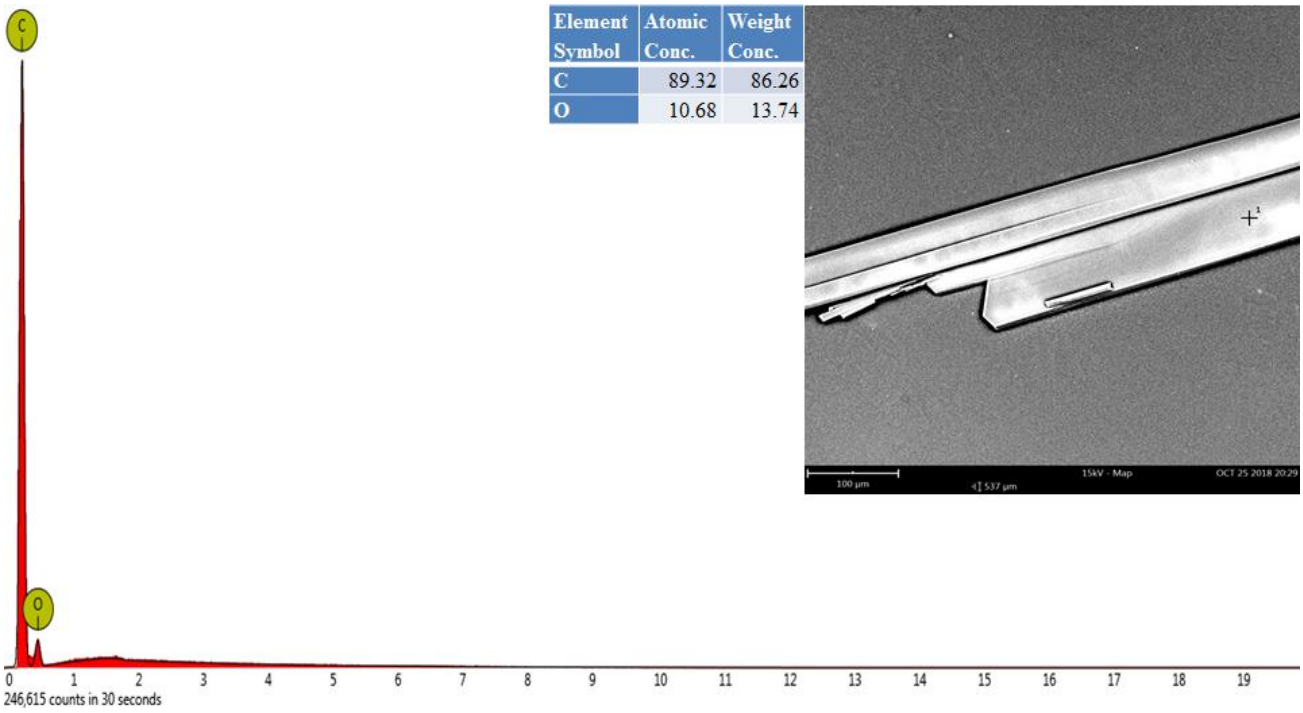

Element Symbol	Atomic Conc.	Weight Conc.
C	89.32	86.26
O	10.68	13.74

Figure S2.9 EDS spectrum of $H_2\mathbf{L}^{I}$. Inset: At the top, the elemental composition of $H_2\mathbf{L}^{I}$ and on the right, backscattered SEM micrograph of $H_2\mathbf{L}^{I}$ at 500 x magnification.

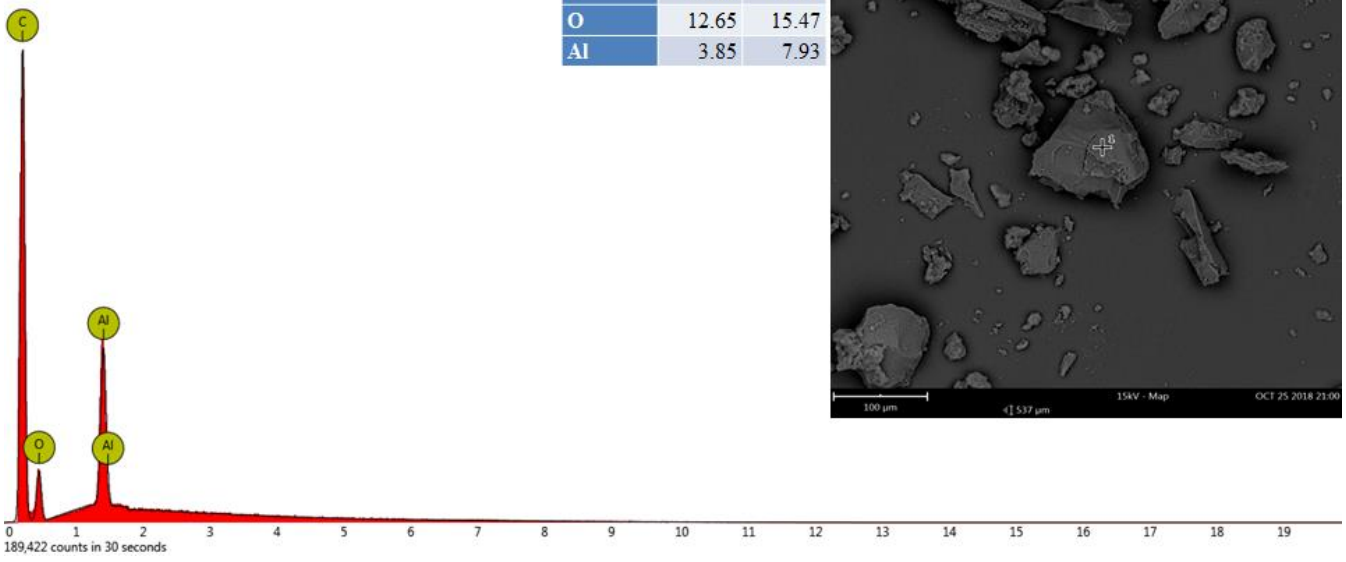

Element Symbol	Atomic Conc.	Weight Conc.
C	83.50	76.61
O	12.65	15.47
Al	3.85	7.93

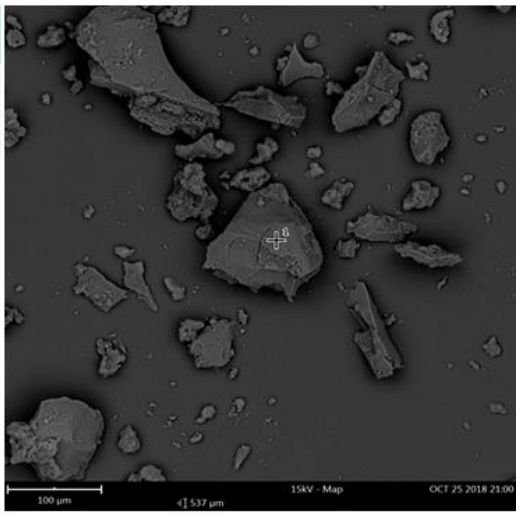

Figure S2.10 EDS spectrum of $[Al_2(\mathbf{L}^{I})]^{4+}$. Inset: At the top, the elemental composition of $[Al_2(\mathbf{L}^{I})]^{4+}$ and on the right, backscattered SEM micrograph of $[Al_2(\mathbf{L}^{I})]^{4+}$ at 500 x magnification.

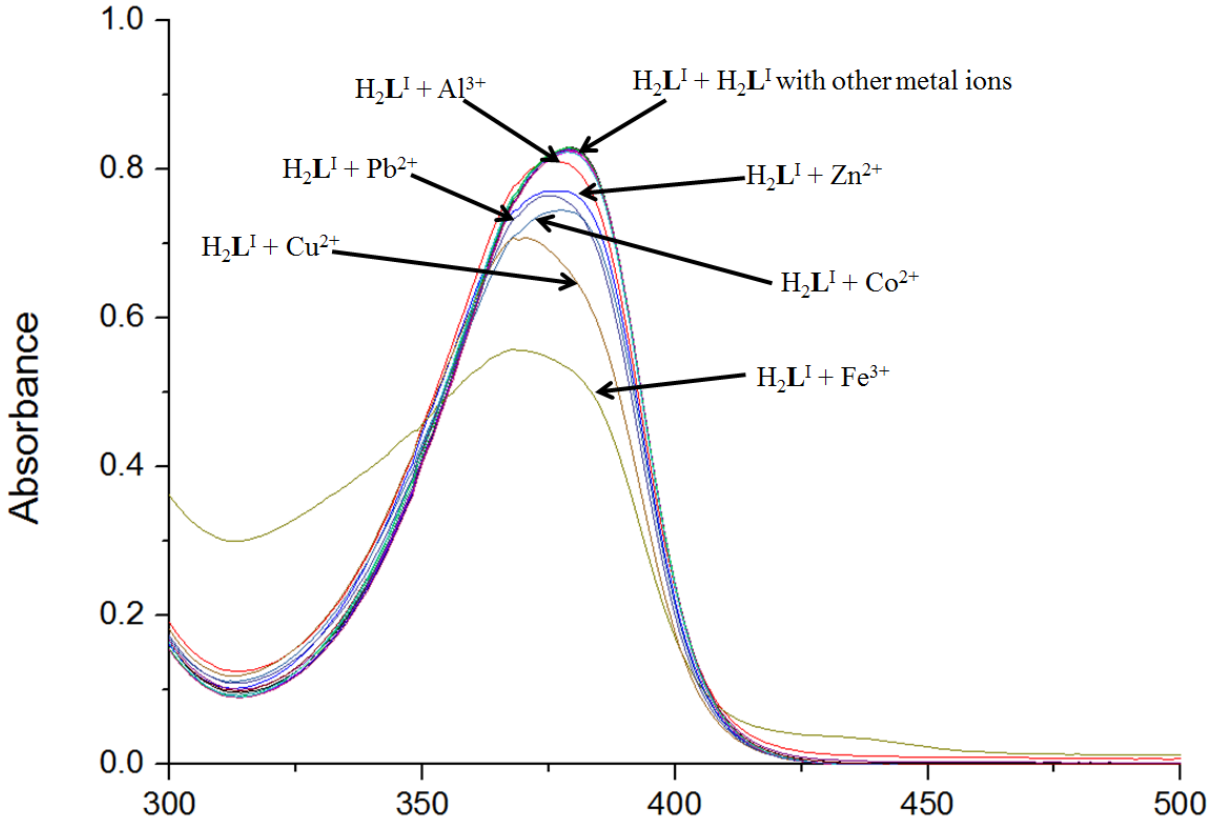

Figure S2.11 The UV-vis spectrum (300-500 nm) of the metal scan of $H_2\mathbf{L}^I$ and $H_2\mathbf{L}^I$ in the presence of various metal ions.

Chapter 3 – The Metal Binding and Anticancer Properties of Lanthanides upon Complexation of a New Schiff Base Ligand

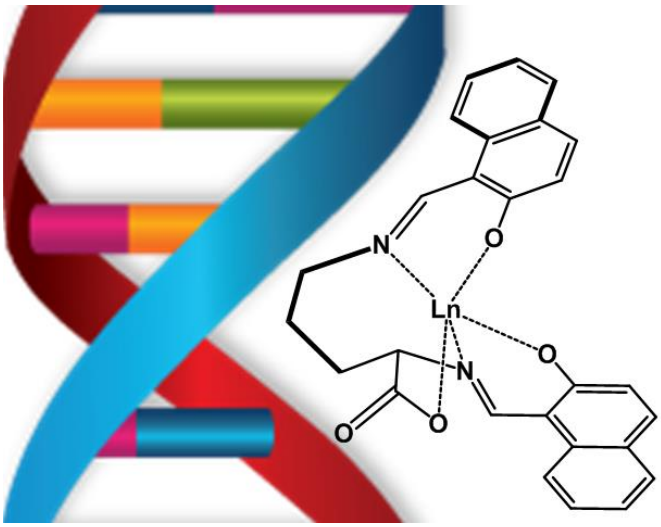

3.1 Abstract

Despite being the focal point of much medicinal research, the high prevalence and fatality rate of cancer-related illnesses demonstrates the difficulty in finding appropriate cancer treatments. Minimal research has explored the potential of lanthanide-based inorganic complexes for their application as anticancer agents despite the unique properties which may make complexes of lanthanides ideal deoxyribose nucleic acid (DNA) binders and hence, anticancer drugs. Herein, ligand ($H_3\mathbf{L}^{II}$) is synthesised via a Schiff base condensation reaction between L-ornithine and 2-hydroxy-1-naphthaldehyde. $H_3\mathbf{L}^{II}$ is initially investigated for its metal binding ability using spectral analysis where it demonstrated a significant and selective ~6.5-fold fluorescent enhancement for Zn^{2+}. Upon complexation of $H_3\mathbf{L}^{II}$ to the trivalent lanthanides (Eu^{3+}, Gd^{3+} and Dy^{3+}), $H_3\mathbf{L}^{II}$ and its lanthanide complexes were investigated for their DNA binding affinity and potential use as anticancer agents. $H_3\mathbf{L}^{II}$ and its complexes demonstrate selectivity to cisplatin resistant A2780 carcinoma cells with EC_{50} values of 12.96 µM, 12.41 µM, 14.06 µM and 6.998 µM for $H_3\mathbf{L}^{II}$, $[Eu\mathbf{L}^{II}_2]^{3-}$, $[Gd\mathbf{L}^{II}_2]^{3-}$ and $[Dy\mathbf{L}^{II}_2]^{3-}$ respectively. Lanthanide complexes were found to increase toxicity of $H_3\mathbf{L}^{II}$ towards 1321N1 astrocytoma cells by 67.5%, 51.5% and 47.9% for $[Eu\mathbf{L}^{II}_2]^{3-}$, $[Gd\mathbf{L}^{II}_2]^{3-}$ and $[Dy\mathbf{L}^{II}_2]^{3-}$ respectively. $H_3\mathbf{L}^{II}$ and its complexes demonstrate DNA binding affinity to calf thymus DNA (ctDNA).

3.2 Introduction

Cancer-related diseases constitute to the top three of the world's deaths and despite best efforts, there are still no cures.[1-3] Chemotherapy is frequently the first treatment for cancer. Anticancer drugs typically function by either preventing or halting the division of rapidly dividing cells such as cancer cells often by interactions with DNA, preventing DNA replication resulting in apoptosis via the p53 pathway. However, other rapidly proliferating cells such as stem cells are also affected by such chemotherapies resulting in many adverse side effects towards the patient.[2,4,5] Platinum-based complexes, such as cisplatin, have achieved great success as anticancer agents since their discovery in the 1960s.[6-8] The success of platinum-based drugs is associated with their ability to bind to nucleobases and cleave DNA either hydrolytically or oxidatively. Binding to DNA results in a kink to formed in the DNA structure and transcription factors are blocked, hence, DNA replication and therefore cell division ceases.[5,9-12] However, platinum-based drugs are associated with multiple side effects and often have succumbed to self-triggered drug resistance. Therefore, the development of alternative metal-based anticancer drugs is imperative for the enhancement of safer, more cancer-specific forms of chemotherapy.[8,13,14] Lanthanides have been of great intrigue to chemists for their magnetic and phosphorescent properties. Their high coordination number and strong binding capabilities allow lanthanides to adopt many different coordinate geometries which remain intact even after excretion from the human body.[15,16] Complexes of lanthanides have been widely investigated for their applications in medical imaging.[17,18] Despite their vast medical usage, recent research suggests lanthanides exhibit cytoxicity.[16] Due to the unique properties of lanthanides, lanthanide-based complexes may make ideal DNA binding and therefore anticancer agents. However, in part due to their labile nature, minimal research has explored the potential applications of lanthanide complexes towards cancer treatment.[18] Lanthanide complexes may prove key to the development of cancer-specific, antitumour treatments.

Herein, $H_3\mathbf{L}^{II}$ is synthesised via the Schiff base condensation reaction between L-ornithine and 2-hydroxy-1-naphthaldehyde. $H_3\mathbf{L}^{II}$ was initially screened as a metal ion fluorescent sensor before being deemed unsuitable due to low effective concentration (EC) values in cell viability assays. Lanthanide (Eu^{3+}, Gd^{3+} and Dy^{3+}) complexes of $H_3\mathbf{L}^{II}$ are then synthesised, characterised are then observed for their DNA binding potential by the use of spectral analysis. $H_3\mathbf{L}^{II}$ and its lanthanide complexes are undergone further cell viability

assays via the MTT reduction method in the presence of 1321N1 astrocytoma, L6 myoblast cells and A2780 carcinoma cell lines to observe potential applications of $H_3\mathbf{L}^{II}$ and its lanthanide complexes as anticancer drugs. The cell viability effects of coordinated lanthanides are then compared to that of $H_3\mathbf{L}^{II}$ to make direct correlations between the effects of coordinated lanthanides and $H_3\mathbf{L}^{II}$.

3.3 Results and Discussion

3.3.1 Synthesis and Structure of $H_3\mathbf{L}^{II}$

$H_3\mathbf{L}^{II}$ was synthesised from the condensation of L-ornithine and 2-hydroxy-1-naphthaldehyde (1:2) at room temperature for 24 h in methanol upon the presence of a catalytic amount of glacial acetic acid (Fig. 3.1). It was then characterised via ^{1}H NMR and ^{13}CNMR, Electrospray Ionisation - High Resolution Mass Spectrometry (ESI-HRMS), FT-IR and simultaneous thermal analysis (STA).

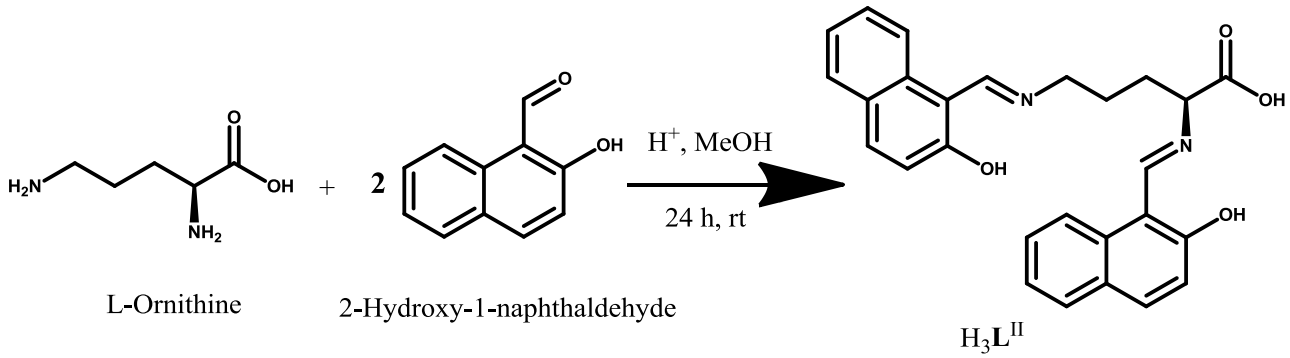

Figure 3.1 Synthesis of $H_3\mathbf{L}^{II}$.

3.3.2 Screening of Metal Cations

$H_3\mathbf{L}^{II}$ was initially characterised in a UV-visible (UV-vis) spectrophotometer indicating a peak maxima of 400 nm. $H_3\mathbf{L}^{II}$ was then scanned in the presence of various metal ions (2 eq.) indicating interaction with Al^{3+}, Fe^{3+}, Co^{2+}, Ni^{2+}, Cu^{2+}, Zn^{2+}, and Pb^{2+}. A fluorescent spectrum of $H_3\mathbf{L}^{II}$ was obtained upon excitation at 399 nm indicating a broad, however, non-fluorescent peak at 464 nm. $H_3\mathbf{L}^{II}$ was then scanned in the presence of various metal ions (2 eq.). A significant fluorescent enhancement response of ~6.5-fold is observed at

447 (blue) nm when $H_3\mathbf{L}^{II}$ is in the presence of Zn^{2+} (2 eq.). A weak fluorescent enhancement is also exhibited at 464 nm when in the presence of Al^{3+}, and Pb^{2+} (2 eq.). Quenching of $H_3\mathbf{L}^{II}$ occurs when in the presence of Fe^{3+}, Co^{2+}, Cu^{2+}, and Hg^{2+} (2 eq.). Results demonstrate that $H_3\mathbf{L}^{II}$ has a significant and selectivity fluorescent response to Zn^{2+} over other metal ions (Fig. 3.2).

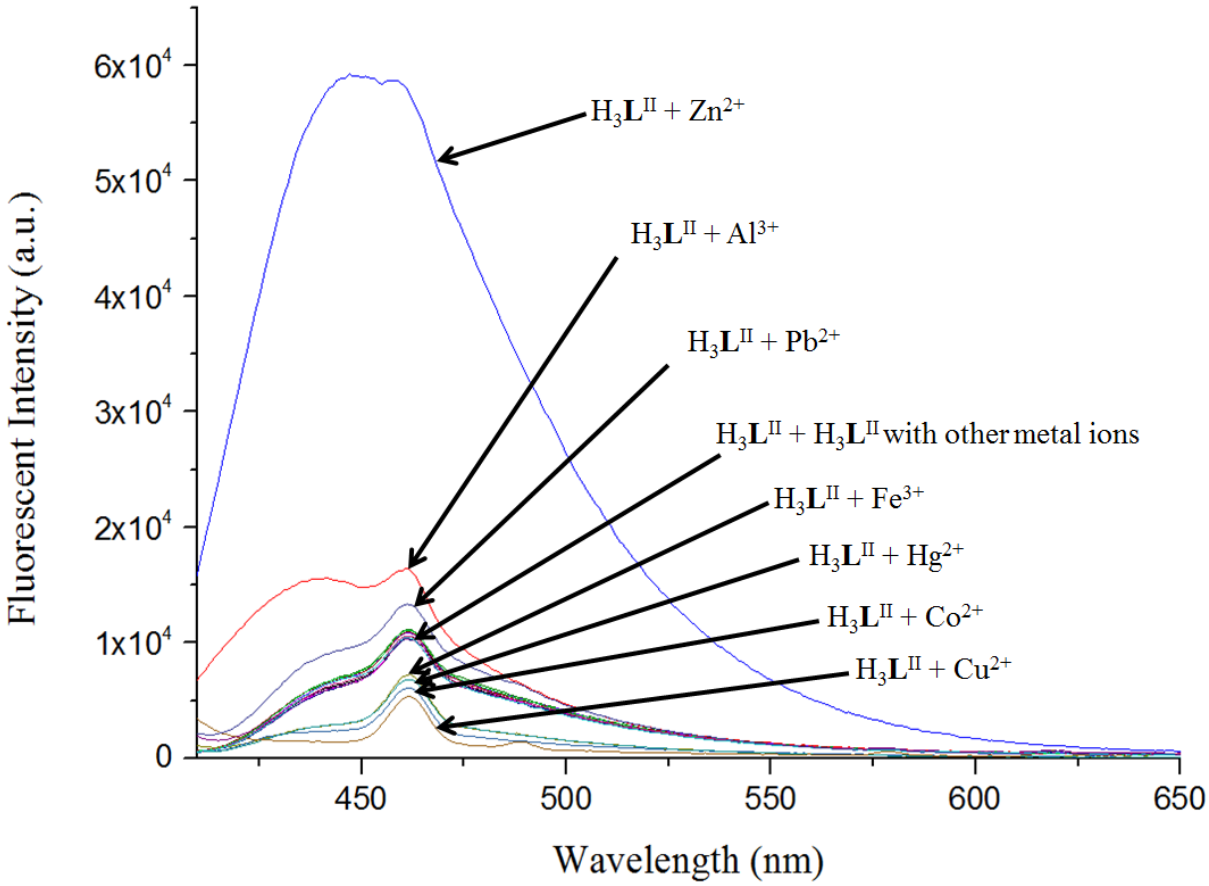

Figure 3.2 The fluorescence spectrum of $H_3\mathbf{L}^{II}$ (20 μM) in the presence of various metal ions (2 eq.) in 20 mM HEPES solution at pH = 7.4.

3.3.3 Competing Metal Ion

Competing metal ion studies of $H_3\mathbf{L}^{II}$ and Zn^{2+} in the coexistence of other metal ions was conducted in order to determine the possibility of $H_3\mathbf{L}^{II}$ to sense Zn^{2+} in the presence of potentially interfering metal ions. $H_3\mathbf{L}^{II}$ and Zn^{2+} in the coexistence of Cr^{3+}, Co^{2+}, and Cu^{2+}, observed significant fluorescence quenching. $H_3\mathbf{L}^{II}$ and Zn^{2+} in the coexistence of Fe^{3+} observed fluorescence quenching; however, still observed a detectable fluorescent

enhancement of ~2-fold (Fig. 3.3).

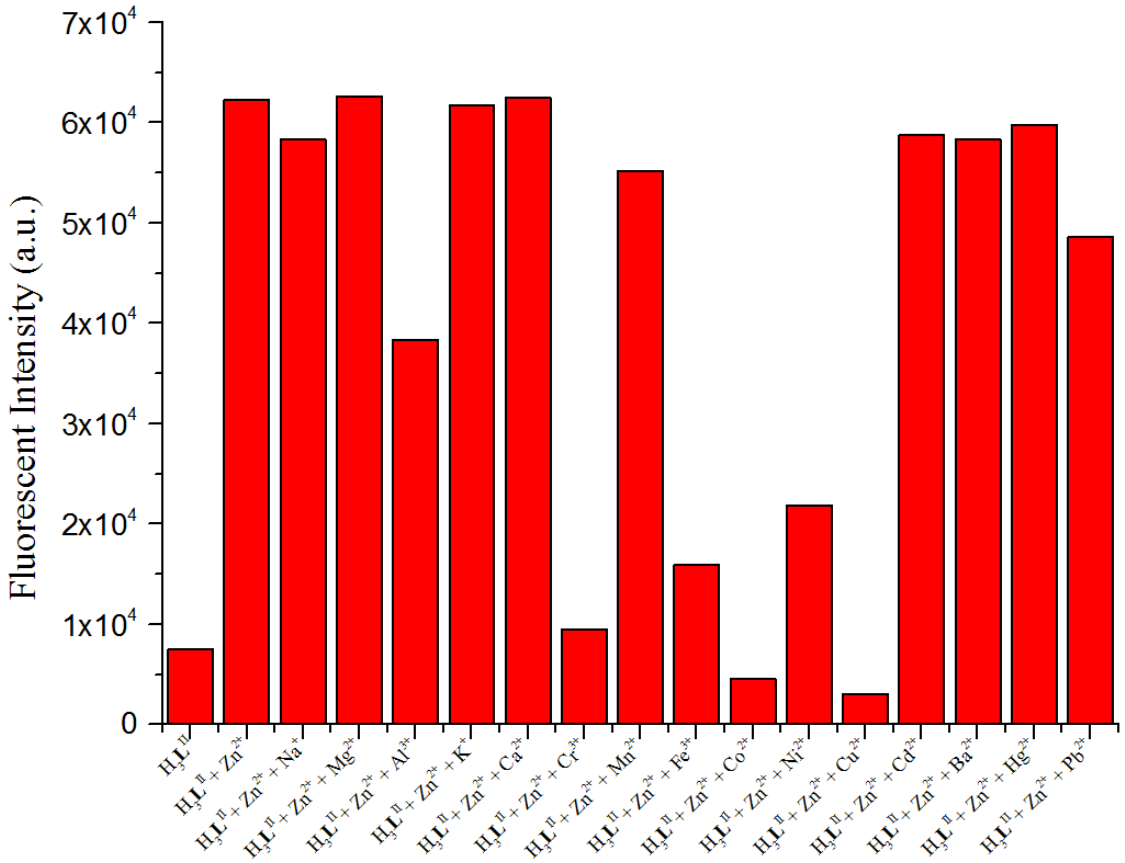

Figure 3.3 Fluorescence intensity of $H_3\mathbf{L}^{II}$ (20 μM) with Zn^{2+} (2 eq.) under the coexistence of other metal cations (2 eq.) in 20 mM HEPES solution at pH = 7.4. The samples were excited at 399 nm and fluorescent intensities were taken at 447 nm.

3.3.4 Cell Viability Assays

Cell viability assays were performed with $H_3\mathbf{L}^{II}$ and its lanthanide complexes (using the MTT method) upon 1321N1 astrocytoma, L6 myoblast and A2780 carcinoma cells as indicated in table 3.1. $H_3\mathbf{L}^{II}$ itself is non-toxic towards 1321N1 astrocytoma cells, however, the lanthanide complexes drastically lowered half maximal effective concentration (EC_{50}) values in comparison to $H_3\mathbf{L}^{II}$ by 67.5%, 51.5% and 47.9% for $[Eu\mathbf{L}^{II}_2]^{3-}$, $[Gd\mathbf{L}^{II}_2]^{3-}$, and $[Dy\mathbf{L}^{II}_2]^{3-}$ respectively. $H_3\mathbf{L}^{II}$ complexes displayed some cytotoxicity towards L6 myoblast cells and the lanthanide complexes exhibited little change in EC_{50} value in comparison to $H_3\mathbf{L}^{II}$. $H_3\mathbf{L}^{II}$ and its lanthanide complexes displayed selective cytotoxicity towards A2780

carcinoma cells. EC_{50} values were determined as 12.96 µM, 12.41 µM, 14.06 µM and 6.998 µM for $H_3\mathbf{L}^{II}$, $[Eu\mathbf{L}^{II}_2]^{3-}$, $[Gd\mathbf{L}^{II}_2]^{3-}$, and $[Dy\mathbf{L}^{II}_2]^{3-}$ respectively. Cisplatin demonstrates EC_{50} values >33 µM for the resistant A2780 carcinoma cell lines which is significantly more than that of $H_3\mathbf{L}^{II}$ and its lanthanide complexes, which also display a substantial amount of specificity towards the cytotoxicity of A2780 carcinoma cell lines over neurological and muscle cell lines.[19]

3.3.5 DNA Binding Assay - UV-vis Analysis

Table 3.1 EC values of $H_3\mathbf{L}^{II}$, $[Eu\mathbf{L}^{II}_2]^{3-}$, $[Gd\mathbf{L}^{II}_2]^{3-}$ and $[Dy\mathbf{L}^{II}_2]^{3-}$ within 1321N1 astrocytoma, L6 myoblast and A2780 carcinoma cells (4 sig. fig; Λ = 595 nm; Error bars = STD; n = 6). The percentage change in EC value (Δ; 3 sig fig.) in comparison to $H_3\mathbf{L}^{II}$ is also indicated.

	1321N1 Astrocytoma						L6 Myoblast						A2780 Carcinoma					
	EC_{20}	**Δ (%)**	**EC_{50}**	**Δ (%)**	**EC_{80}**	**Δ (%)**	**EC_{20}**	**Δ (%)**	**EC_{50}**	**Δ (%)**	**EC_{80}**	**Δ (%)**	**EC_{20}**	**Δ (%)**	**EC_{50}**	**Δ (%)**	**EC_{80}**	**Δ (%)**
$H_3\mathbf{L}^{II}$	223.2 ± 31.32	0	308.4 ± 56.62	0	426.2 ± 142.8	0	39.17 ± 4.679	0	56.91 ± 4.235	0	82.69 ± 10.82	0	8.904 ± 2.561	0	12.96 ± 1.999	0	18.87 ± 0.474	0
$[Eu\mathbf{L}^{II}_2)]^{3-}$	73.21 ± 6.349	-67.2	100.1 ± 4.417	-67.5	136.8 ± 9.270	-67.9	40.45 ± 9.758	3.27	57.39 ± 9.981	0.84	81.41 ± 22.46	-1.55	5.804 ± 1.789	-34.8	12.41 ± 1.705	-4.24	26.54 ± 2.455	40.6
$[Gd\mathbf{L}^{II}_2)]^{3-}$	127.8 ± 3.164	-42.7	149.7 ± 1.653	-51.5	175.4 ± 3.834	-58.8	33.00 ± 7.676	-15.8	61.04 ± 8.508	7.26	113.00 ± 23.31	36.7	8.117 ± 2.398	-8.84	14.06 ± 1.775	8.49	24.35 ± 1.968	29.0
$[Dy\mathbf{L}^{II}_2)]^{3-}$	140.1 ± 10.15	-37.2	160.6 ± 8.782	-47.9	184.2 ± 18.75	-56.8	27.02 ± 8.255	-31.0	67.50 ± 14.04	18.6	168.62 ± 61.72	204	1.734 ± 1.462	-80.5	6.998 ± 2.216	-46.0	28.25 ± 5.412	49.7

As the primary pharmacological target of many metal-based anticancer drugs, DNA binding activities of $H_3\mathbf{L}^{II}$ and its lanthanide complexes (25 µM) were obtained in a UV-vis spectrum in the absence and then in the presence of ctDNA (40 µM; Fig. 3.4). Results indicated mild amounts of absorbance shifting in all samples of $H_3\mathbf{L}^{II}$ and its lanthanide complexes indicating DNA binding activity.

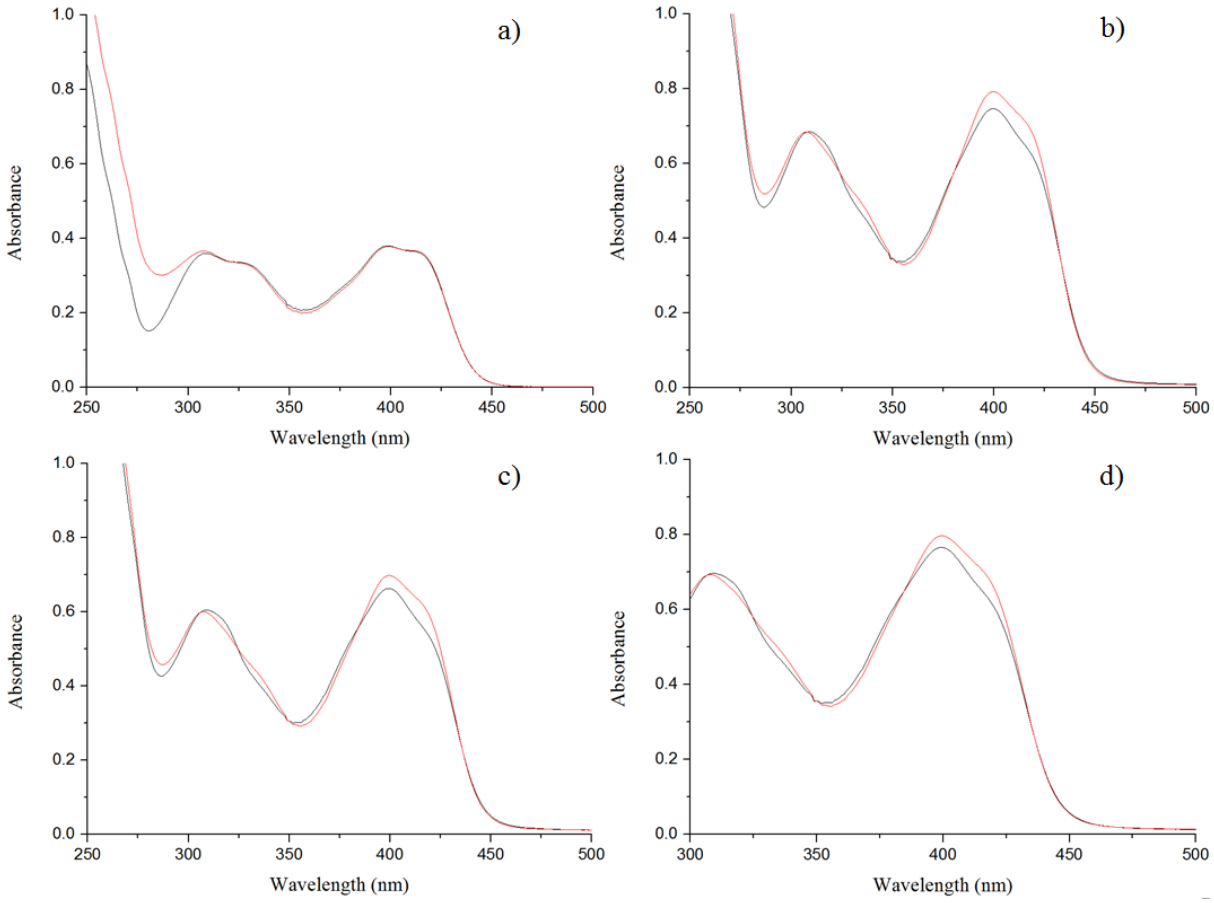

Figure 3.4 Electronic spectra of a) $H_3\mathbf{L}^{II}$ (black) and $H_3\mathbf{L}^{II}$ upon addition of ctDNA (red) b) $[Eu\mathbf{L}^{II}_2]^{3-}$ (black) and $[Eu\mathbf{L}^{II}_2]^{3-}$ upon addition of ctDNA (red) c) $[Gd\mathbf{L}^{II}_2]^{3-}$ (black) and $[Gd\mathbf{L}^{II}_2]^{3-}$ upon addition of ctDNA (red) d) $[Dy\mathbf{L}^{II}_2]^{3-}$ (black) and $[Dy\mathbf{L}^{II}_2]^{3-}$ upon addition of ctDNA (red) in Milli-Q water (250-500 nm).

3.3.6 DNA Binding Assay - Fluorescent Analysis

Ethidium bromide (EB) was used to allow for fluorescence of ctDNA forming ctDNA-EB (40 µM). Upon addition of $H_3\mathbf{L}^{II}$ and its lanthanide complexes (25 µM), fluorescent enhancements, as well as blue fluorescent shifts, are observed in all molecules indicating the DNA binding of $H_3\mathbf{L}^{II}$ and its lanthanide complexes (Fig. 3.5). Spectral DNA binding studies from both colourimetric and fluorescent analysis of $H_3\mathbf{L}^{II}$ and its lanthanide complexes imply that all molecules are likely interacting with DNA within cells, resulting in apoptosis and thus low EC values. The DNA binding which is exhibited by $H_3\mathbf{L}^{II}$ and its lanthanide complexes may be likely due to the left-handed (L) chirality of both $H_3\mathbf{L}^{II}$ and

complexes. Many biomolecules, such as DNA, exhibited left-handed chirality, allowing for a greater affinity towards groove binding with other left-handed chiral molecules such as $H_3\mathbf{L}^{II}$.[20,21]

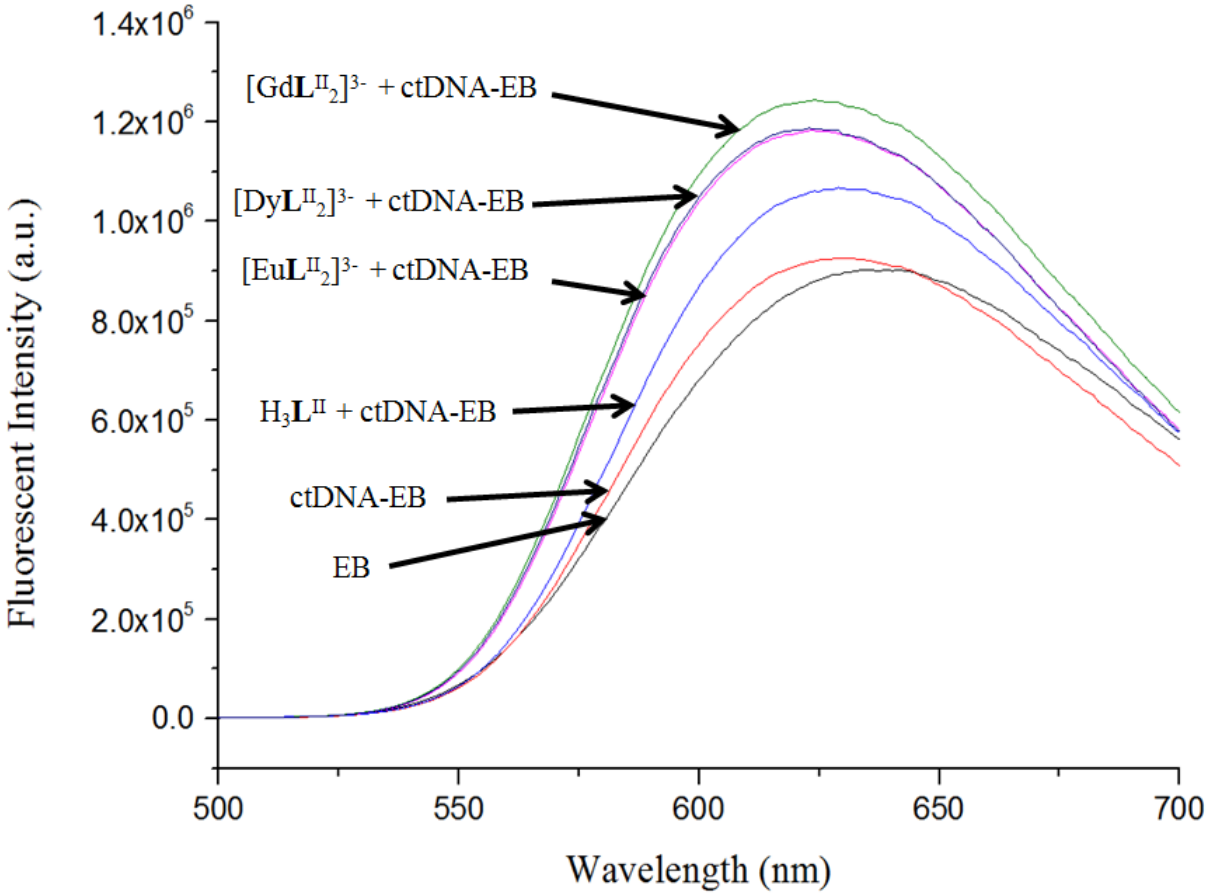

Figure 3.5 The fluorescence spectrum of $H_3\mathbf{L}^{II}$ and its lanthanide complexes interacting with ctDNA-EB in Milli-Q water (500-700 nm).

3.4 Conclusion

$H_3\mathbf{L}^{II}$ and its lanthanide complexes were successfully synthesised and characterised. $H_3\mathbf{L}^{II}$ displayed some potential as a Zn^{2+} sensor; however, its potential is limited due to its high cytotoxicity, as well as, poor binding affinity for Zn^{2+}. $H_3\mathbf{L}^{II}$ and its lanthanide complexes demonstrated selectively low EC values for A2780 carcinoma cells. This was significantly lower than that of cisplatin, evoking the potential use of $H_3\mathbf{L}^{II}$ and lanthanide complexes as anticancer drugs. The lanthanide complexes exhibited drastically lower EC values in astrocytoma cells in respect to $H_3\mathbf{L}^{II}$ indicating the selectivity of lanthanides to

enhance toxicity of ligands towards neurological cell lines. However, lanthanide complexes had little effect on cell viability of L6 myoblast and 1321N1 astrocytoma cell lines. DNA binding studies affirmed the potential mechanism of how $H_3\mathbf{L}^{II}$ and its lanthanide complexes are evoking cytotoxic responses, by binding to DNA, preventing cell division, resulting in apoptosis.

3.5 Experimental

3.5.1 Chemicals and Reagents

All chemicals, solvents and cell lines were purchased from commercial sources of commercial grade and used without further purification. All aqueous solutions were prepared with type I water from a Milli-Q water purification system. Metal standards were prepared from chloride (Na^+ , Mg^{2+}, Al^{3+}, K^+ , Ca^{2+}, Cr^{3+}, Mn^{2+}, Fe^{3+}, Co^{2+}, Ni^{2+}, Cu^{2+}, Zn^{2+}, Cd^{2+}, Ba^{2+}, and Hg^{2+}) or nitrate (Pb^{2+}) salts of analytical grade, then standardised using literature complexometric titration methods with H_2Na_2EDTA.[22]

3.5.2 Instrumentations

Characterisation of $H_3\mathbf{L}^{II}$ was carried out using a range of techniques. ^1H and ^{13}C NMR spectra were measured on a Bruker DRX-300 NMR spectrometer. FT-IR measurements were conducted on a Bruker Vertex 70 spectrometer. Electrospray ionisation high resolution mass spectra (ESI-HRMS) were collected using a Waters Xevo QToF quadrupole mass spectrometer with samples dissolved in methanol. Simultaneous thermal analysis (STA) was undertaken on a Netzsch STA449 C Jupiter thermo-microbalance. An Edinburgh instruments FS5 Spectrofluorometer was used to conduct all fluorescent measurements. Agilent Cary 100 spectrophotometer was used to conduct the UV-vis experiments. Quartz cuvettes with a 1 cm optical path length were used for all fluorescent and colourmetric experiments. Fluorescent and colourimetric measurements, as well as cell viability assays, were graphed using Origin Pro 9.0. Scanning electron microscopy–electron dispersive spectroscopy (SEM-EDS) analysis was conducted on a Phenom XL instrument. Samples were run at 15 kV at medium vacuum without surface coating.

3.5.3 Synthesis of $H_3\mathbf{L}^{II}$

L-ornithine (300 mg, 2.27 mmol) and 2-hydroxy-1-naphthaldehyde (782 mg, 4.54 mmol) was dissolved in methanol (25 mL) into a conical flask. Five drops of glacial acetic acid were then added to the mixture. The mixture was stirred at room temperature (rt) for 24 h. The precipitate was then collected using filtration and washed thoroughly in methanol and then diethyl ether. The precipitate was left to dry overnight resulting was a bright yellow powder with a yield of ~90%. m.p. 197.5 °C, ^{1}HNMR: (300 MHz, DMSO-d_6 with TMS) δ 9.223 (s, 1H, N=CH), δ 9.120 (s, 1H, N=CH), δ 8.090-6.733 (m, ArH), δ 4.544 (t, J = 6.82 Hz, 1H, CH), δ 3.722 (t, 2H, CH_2) δ 2.079 (m, 1H, CH), δ 1.991 (m, 1H, CH), δ 1.772 (m, 2H, CH_2). ^{13}CNMR: (75 MHz, DMSO-d_6 with TMS) δ 176.95, δ 174.85, δ 172.06, δ 159.62, δ 159.11, δ 136.93, δ 136.9, δ 134.13, δ 133.79, δ 128.84, δ 128.75, δ 127.87, δ 127.73, δ 125.57, δ 125.30, δ 124.26, δ 122.51, δ 122.04, δ 118.72, δ 118.38, δ 106.39, δ 105.61, δ 63.61, δ 50.23, δ 30.20, δ 25.35. ESI-HRMS: 441.1777 *m/z* $[H_3\mathbf{L}^{II} + H]^+$. FT-IR: 3027.02 cm^{-1} (O-H, carboxylic acid), 2929.32 cm^{-1} (O-H, phenol), 1716.96 cm^{-1} (O=C, carboxylic acid), 1615.62 cm^{-1} (C=N). UV−vis (1 cm optical path length, Milli-Q H_2O, HEPES 20 mM, pH = 7.4): 20 μM $H_3\mathbf{L}^{II}$, λmax = 414 nm (abs = 0.35585, ε = 17 793).

3.5.4 Synthesis of $[Eu\mathbf{L}^{II}{}_2]^{3-}$

Potassium hydroxide (46.6 mg, 0.681 mmol) was dissolved in 10 mL methanol. $H_3\mathbf{L}^{II}$ (100 mg, 0.227 mmol) was completely dissolved in the mixture and filtered. The filtrate was then collected and stirred at rt for 5 min. Europium nitrate hexahydrate (50.6 mg, 0.114 mmol) was dissolved in 10 mL methanol and added dropwise to the mixture. The mixture was then stirred for a further 2 h and filtered. The precipitate was then collected and dried overnight. The result was a bright yellow powder at ~40% yield. ESI-HRMS: 1107.4897 *m/z* $[Eu\mathbf{L}^{II}{}_2]^{3-}$; $[[Eu\mathbf{L}^{II}{}_2] + H_2 + K_2]]^+$ FT-IR: 3053.30 cm^{-1} (O-H, carboxylic acid), 2917.94 cm^{-1} (O-H, phenol), 1615.80 cm^{-1} (O=C, carboxylic acid), 1542.82 cm^{-1} (C=N).

3.5.5 Synthesis of $[Gd\mathbf{L}^{II}{}_2]^{3-}$

Potassium hydroxide (46.6 mg, 0.681 mmol) was dissolved in 10 mL methanol. $H_3\mathbf{L}^{II}$ (100 mg, 0.227 mmol) was completely dissolved in the mixture and filtered. The filtrate was then collected and stirred at rt for 5 min. Gadolinium nitrate hexahydrate (51.5 mg, 0.114

mmol) was dissolved in 10 mL methanol and added dropwise to the mixture. The mixture was then stirred for a further 2 h and filtered. The precipitate was then collected and dried overnight. The result was a bright yellow powder at ~40% yield. ESI-HRMS: 1112.5115 *m/z* $[Gd\mathbf{L}^{II}_2]^{3-}$; $[[Gd\mathbf{L}^{II}_2] + H_2 + K_2]]^+$ FT-IR: 2989.03 cm^{-1} (O-H, carboxylic acid), 2900.90 cm^{-1} (O-H, phenol), 1615.77 cm^{-1} (O=C, carboxylic acid), 1543.37 cm^{-1} (C=N).

3.5.6 Synthesis of $[Dy\mathbf{L}^{II}_2]^{3-}$

Potassium hydroxide (46.6 mg, 0.681 mmol) was dissolved in 10 mL methanol. $H_3\mathbf{L}^{II}$ (100 mg, 0.227 mmol) was completely dissolved in the mixture and filtered. The filtrate was then collected and stirred at rt for 5 min. Dysprosium nitrate hexahydrate (52.1 mg, 0.114 mmol) was dissolved in 10 mL methanol and added dropwise to the mixture. The mixture was then stirred for a further 2 h and filtered. The precipitate was then collected and dried overnight. The result was a bright yellow powder at ~40% yield. ESI-HRMS: 1118.5183 *m/z* $[Dy\mathbf{L}^{II}_2]^{3-}$; $[[Dy\mathbf{L}^{II}_2] + H_2 + K_2]]^+$ FT-IR: 2989.06 cm^{-1} (O-H, carboxylic acid), 2900.95 cm^{-1} (O-H, phenol), 1615.91 cm^{-1} (O=C, carboxylic acid), 1543.36 cm^{-1} (C=N).

3.5.7 Fluorescent and UV−Vis Spectroscopy

A stock solution of $H_3\mathbf{L}^{II}$ (2 mM) was prepared in DMSO; this solution was used for all spectral experiments. Metal interaction experiments were carried out by aliquoting appropriate volumes of $H_3\mathbf{L}^{II}$ stock solution to 20 μM and metal ions to 40 μM (2 eq.) in 5 mM HEPES buffer at 7.4 pH in Milli-Q water to a total cuvette volume of 3 mL. All fluorescent studies were excited at 399 nm and scanned from 409-700 nm prepared ~12 h prior to running, where they were stored in a dark, dry environment at standard laboratory conditions. All fluorescent experiments were conducted at slits of ex/em = 4/4 nm.

3.5.8 Cell Culturing

Human 1321N1 cell line (1321N1 astrocytoma; purchased from Sigma-Aldrich/ ATCC) and immortalised rat skeletal myoblasts cell line (L6 myoblast; purchased from ATCC) were grown in Dulbecco's modified eagle medium (DMEM). A2780 human ovarian cancer cell line (A2780 carcinoma; purchased from ATCC) were grown in Rosewell Park Memorial Institute medium (RPMI-1640). All media of all cells lines used were

supplemented with 10% fetal bovine serum (FBS) and antibiotics (penicillin-100 µg ml^{-1}; streptomycin-50 µg ml^{-1}). All cells were cultured at 37 °C in a 95% air, 5% CO_2 incubator.

3.5.9 Cell Viability Assay

Cells (either 1321N1 astrocytoma, L6 myoblast or A2780 cell lines) were seeded into a 96-well plate and filled with complete DMEM (for 1321N1 astrocytoma and L6 myoblast cells) or RPMI-1640 (for A2780 carcinoma cell line) to a total volume of 190 µL containing 10,000 cells each and then incubated (37 °C, CO_2 5%) for 24 h. Stock solutions of $H_3\mathbf{L}^{II}$ and $[Ln\mathbf{L}^{II}_2]^{3-}$ (10 mM, 5 mM, 1.25 mM) were prepared in sterile Milli-Q water and DMSO (1:1, v/v) solutions. 10 µL of sextet concentration of 0, 20, 50, 100, 150, 200, 300, 350, 400 and 500 µM of $H_3\mathbf{L}^{II}$ and $[Ln\mathbf{L}^{II}_2]^{3-}$ were prepared into the 96 well plates and incubated for 24 h. 50 µL of 5 mg/mL 3-(4,5-dimethylthiazol-2-yl)-2,5-diphenyltetrazolium bromide (MTT) was added into each well and the cells were then left to incubate (37 °C, CO_2 5%) for a further 2 h. The media was decanted from each well and 100 µL of DMSO was added into each well to solubilise the formazan crystals. The 96 plate well was gently agitated before optical absorbance was measured at 595 nm using the BMG FLUOstar OPTIMA microplate reader. The values were then calculated as the mean ± standard deviation errors of six independent experiments. The cell viability was expressed as the optical absorbance of formazan at 595 nm. EC values were determined using Origin Pro 9.0 sigmoidal logistics curves.

3.5.10 ctDNA Sample Preparation

Stock solutions of $H_3\mathbf{L}^{II}$ and $[Ln\mathbf{L}^{II}_2]^{3-}$ (2 mM) were prepared in DMSO. A Stock solution of ctDNA (4 mM) was calculated using Beer's law using the molar absorption coefficient of 6600 M^{-1} cm^{-1} at 258 nm in sodium chloride (5 mM).[23] The UV absorbance ratio (260 nm over 280 nm) was calculated to be greater than 1.8, indicating that the ctDNA was sufficiently free of protein.[24] The DNA was then stored at 4 °C and used within 6 months of preparation.

3.5.11 DNA Binding Assay - UV-vis Analysis

Samples of 25 µM $H_3\mathbf{L}^{II}$ or $[Ln\mathbf{L}^{II}_2]^{3-}$ were prepared in a cuvette of Milli-Q water and

measured from 200-800 nm. Additions of ctDNA (40 µM) were aliquoted into the cuvette and incubated for one minute. The samples were scanned again from 200-800 nm to observe for any interactions between $H_3\mathbf{L}^{II}$ or $[Ln\mathbf{L}^{II}_2]^{3-}$ with ctDNA.

3.5.12 DNA Binding Assay - Fluorescent Analysis

A stock solution of ethidium bromide (EB; 500 µM) was prepared in Milli-Q water. 40 µM of EB was aliquoted to a cuvette of Milli-Q water and measured. ctDNA (40 µM) was then added and measured forming ctDNA-EB. Aliquots of either $H_3\mathbf{L}^{II}$ or $[Ln\mathbf{L}^{II}_2]^{3-}$ (25 µM) were then added to observe DNA binding interactions. All experiments were excited at 260 nm at slits of ex/em = 4/4 nm.

2.6 Acknowledgments

The authors thank the Western Sydney University (WSU) Advance Material Characterisation Facility and the WSU Mass Spectrometry Facility for instrumental access. D.J.W. also thanks WSU for their postgraduate research funding.

2.7 Conflicts of Interest

There are no conflicts to declare.

3.8 Reference List

1. D. R. Williams. Metals, Ligands, and Cancer. *Chemical Reviews* **72**, 203–213 (1972).
2. H. Wu *et al.* Two Lanthanide(III) Complexes based on the Schiff Base N,N-Bis(salicylidene)-1,5-diamino-3-oxapentane: Synthesis, Characterization,DNA-binding Properties, and Antioxidation. *Z. Anorg. Allg. Chem.* **640**, 2062–2071 (2014).
3. J. Zhou, L.-F. Wang, J.-Y. Wang & N. Tang. Synthesis, characterization, antioxidative and antitumor activities of solid quercetin rare earth(III) complexes. *Journal of Inorganic Biochemistry* **83**, 41–48 (2001).
4. I. Ott. On the medicinal chemistry of gold complexes as anticancer drugs. *Coordination Chemistry Reviews* **253**, 1670–1681 (2009).
5. A. Chakraborty, P. Kumar, K. Ghosh & P. Roy. Evaluation of a Schiff base copper complex compound as potent anticancer molecule with multiple targets of action. *European Journal of Pharmacology* **647**, 1–12 (2010).
6. B. Rosenberg, L. V. Camp, J. E. Trosko & V. H. Mansour. Platinum Compounds: a New Class of Potent Antitumour Agent. *Nature* **222**, 385–386 (1969).
7. Z. Abbasi, M. Salehi, A. Khaleghian & M. Kubicki. In vitro cytotoxic activity of a novel Schiff base ligand derived from 2-hydroxy-1-naphthaldehyde and its mononuclear metal complexes. *Journal of Molecular Structure* **1173**, 213–220 (2018).
8. X. Qiao *et al.* Study on potential antitumor mechanism of a novel Schiff Base copper(II) complex: Synthesis, crystal structure, DNA binding, cytotoxicity and apoptosis induction activity. *Journal of Inorganic Biochemistry* **105**, 728–737 (2011).
9. A. Hussain *et al.* Photocytotoxic Lanthanum(III) and Gadolinium(III) Complexes of Phenanthroline Bases Showing Light-Induced DNA Cleavage Activity. *Inorg. Chem.* **49**, 4036–4045 (2010).
10. N. J. Turro, J. K. Barton & D. A. Tomalia. Molecular Recognition and Chemistry in Restricted Reaction Spaces. Photophysics and Photoinduced Electron Transfer on the Surfaces of Micelles, Dendrimers, and DNA. *Acc. Chem. Res.* **24**, 332–340 (1991).
11. E. L. Hegg & J. N. Burstyn. Toward the development of metal-based synthetic nucleases and peptidases: a rationale and progress report in applying the principles of coordination chemistry. *Coordination Chemistry Reviews* **173**, 133–165 (1998).
12. F. Mancin, P. Scrimin, P. Tecilla & U. Tonellato. Artificial metallonucleases. *Chem. Commun.* **20**, 2540–2548 (2005).
13. I. Kostova. Lanthanides as Anticancer Agents. *Curr. Med. Chem. - Anti-Cancer Agents* **5,** 591–602 (2005).
14. P. C. A. Bruijnincx & P. J. Sadler. New trends for metal complexes with anticancer activity. *Curr. Opin. Chem. Biol.* **12,** 197–206 (2008).
15. P. Caravan, J. J. Ellison, T. J. McMurry & R. B. . Lauffer. Gadolinium(III) Chelates as MRI Contrast Agents: Structure, Dynamics, and Applications. *Chem Rev* **99,** 2293−2352 (1999).
16. P. Tai, Q. Zhao, D. Su, P. Li & F. Stagnitti. Biological toxicity of lanthanide elements on algae. *Chemosphere* **80,** (2010).
17. M. T. Kaczmarek, M. Zabiszak, M. Nowak & R. Jastrzab. Lanthanides: Schiff base complexes, applications in cancer diagnosis, therapy, and antibacterial activity. *Coordination Chemistry Reviews* **370**, 42–54 (2018).
18. Z.-Q. Xu *et al.* Synthesis, characterization and anticancer activities of two lanthanide(III) complexes with a nicotinohydrazone ligand. *Journal of Molecular Structure* **1102**, 86–90 (2015).
19. W. Yu *et al.* α-TEA inhibits survival and enhances death pathways in cisplatin sensitive and resistant human ovarian cancer cells. *Apoptosis* **11**, 1813–1823 (2006).

20. O. Delalande, J. Malina, V. Brabec & J. Kozelka. Chiral Differentiation of DNA Adducts Formed by Enantiomeric Analogues of Antitumor Cisplatin Is Sequence-Dependent. *Biophys J.* **88**, 4159–4169 (2005).
21. Y. Wang, H. Huang, Q. Zhang & P. Zhang. Chirality in metal-based anticancer agents. *Dalton Trans.* **47**, 4017–4026 (2018).
22. G. Schwarzenbach & H. Flaschka. *Complexometric Titrations*. (H. M. N. H, 1969).
23. C. V. Kumar & E. H. Asuncion. DNA Binding Studies and Site Selective Fluorescence Sensitization of an Anthryl Probe. *J. Am. Chem. Soc.* **115**, 8547–8553 (1993).
24. Y.-B. Zeng, N. Yang, W.-S. Liu & N. Tang. Synthesis, characterization and DNA-binding properties of La(III) complex of chrysin. *Journal of Inorganic Biochemistry* **97**, 258–264 (2003).

3.9 Supplementary Information

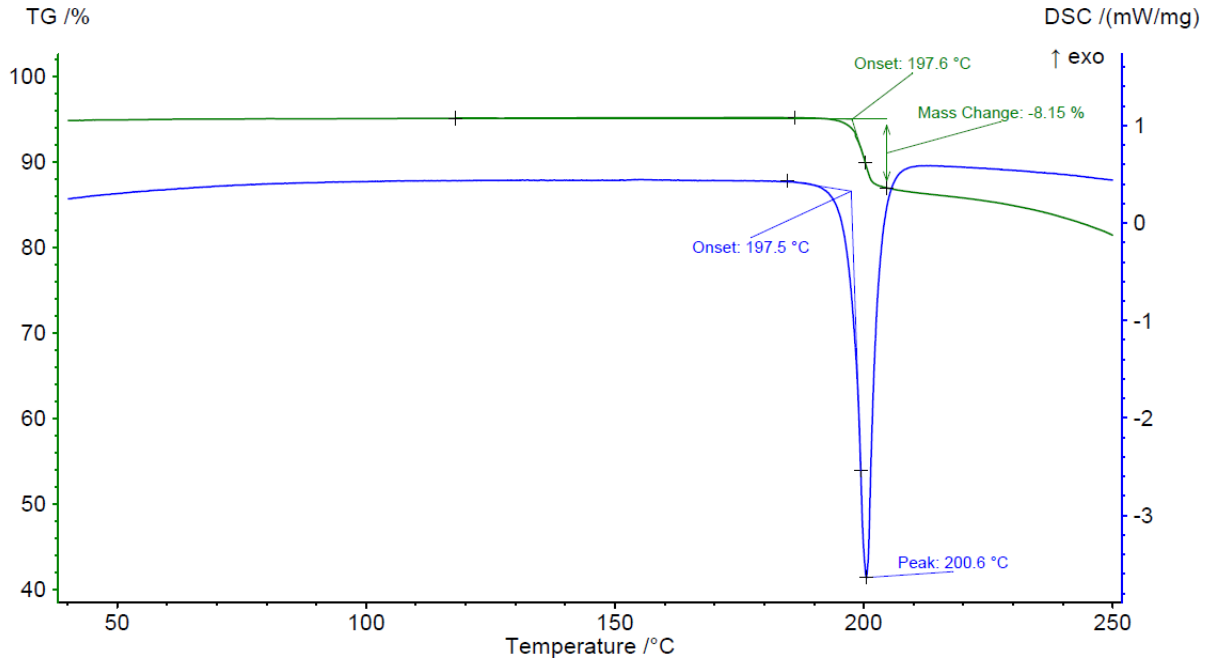

Figure S3.1 The STA data of $H_3\mathbf{L}^{II}$ (40-250 °C).

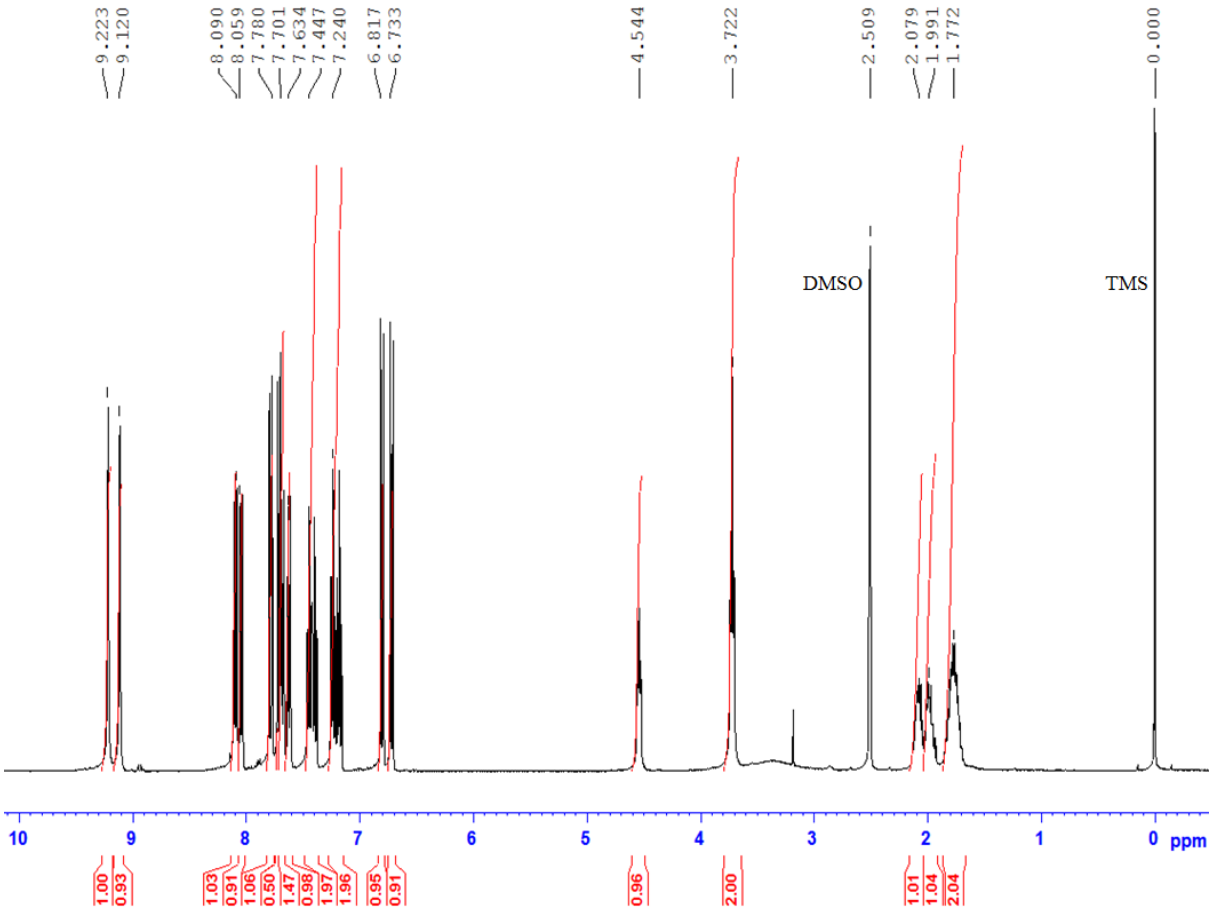

Figure S3.2 The ^{1}HNMR spectrum of $H_3\mathbf{L}^{II}$ in DMSO-d_6.

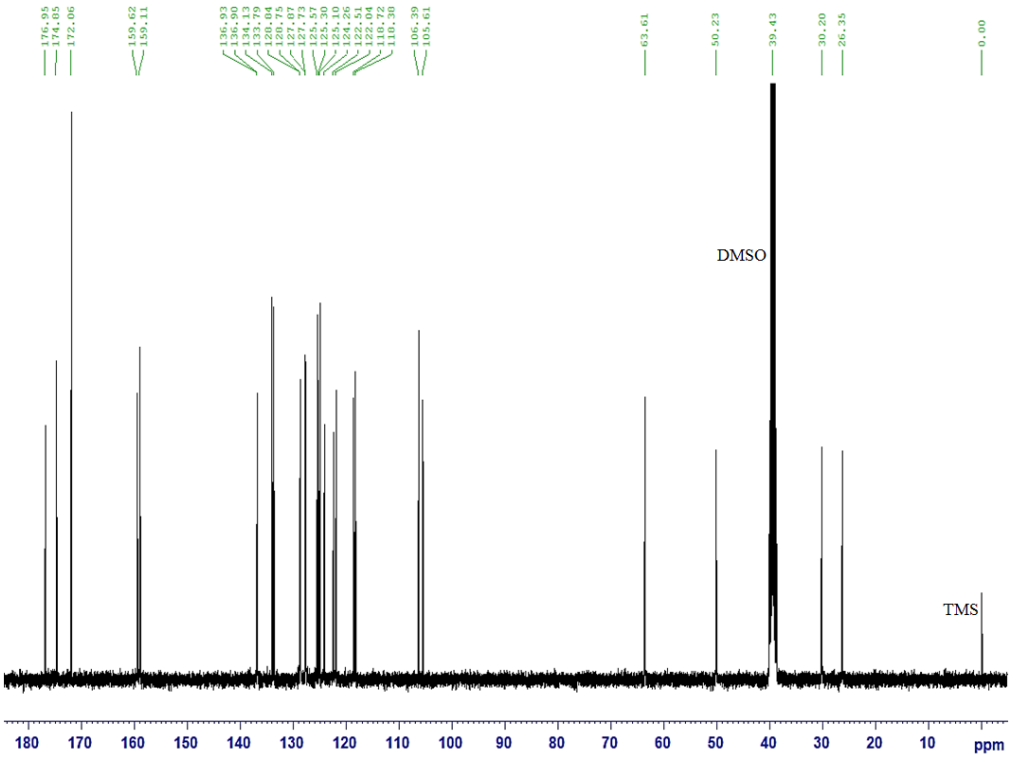

Figure S3.3 The ^{13}CNMR spectrum of $H_3\mathbf{L}^{II}$ in DMSO-d_6.

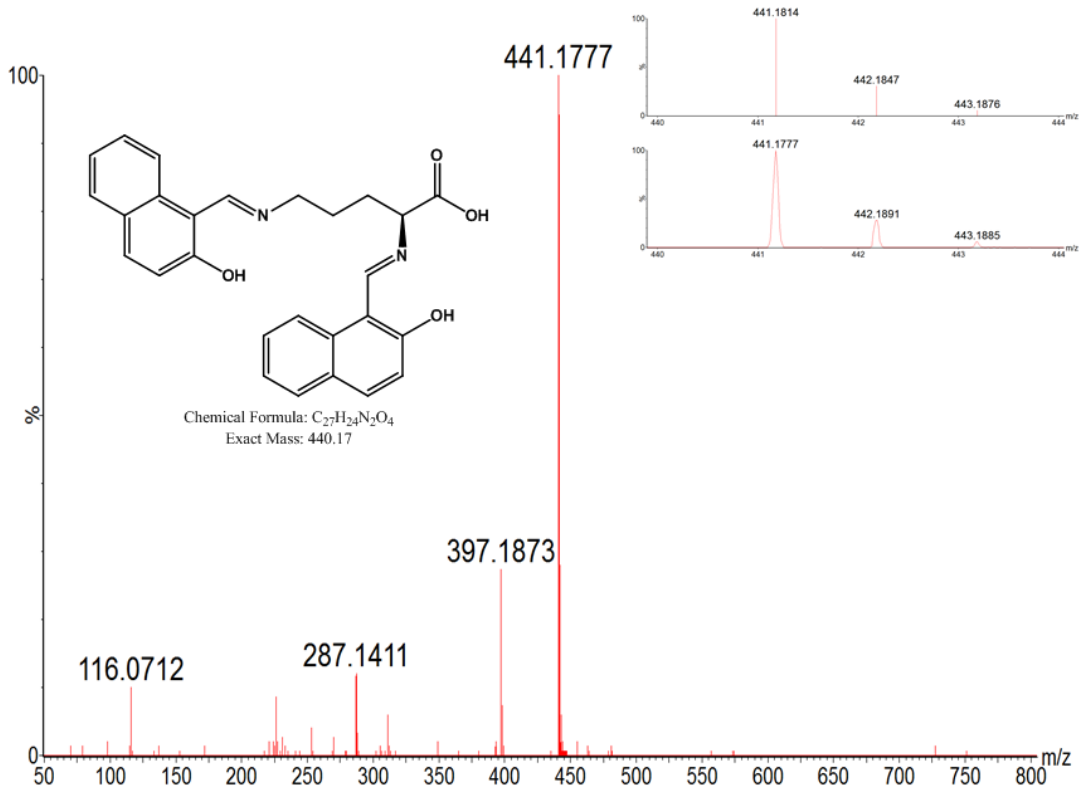

Figure S3.4 ESI-HRMS of $H_3\mathbf{L}^{II}$;$[H_3\mathbf{L}^{II} + H]^+$ in methanol from 50 – 800 *m/z*. Inset: On the left, the structure and molar mass of $H_3\mathbf{L}^{II}$. On the right, the predicted (above) and experimental (bellow) isotopic patterns of $[H_3\mathbf{L}^{III} + H]^+$.

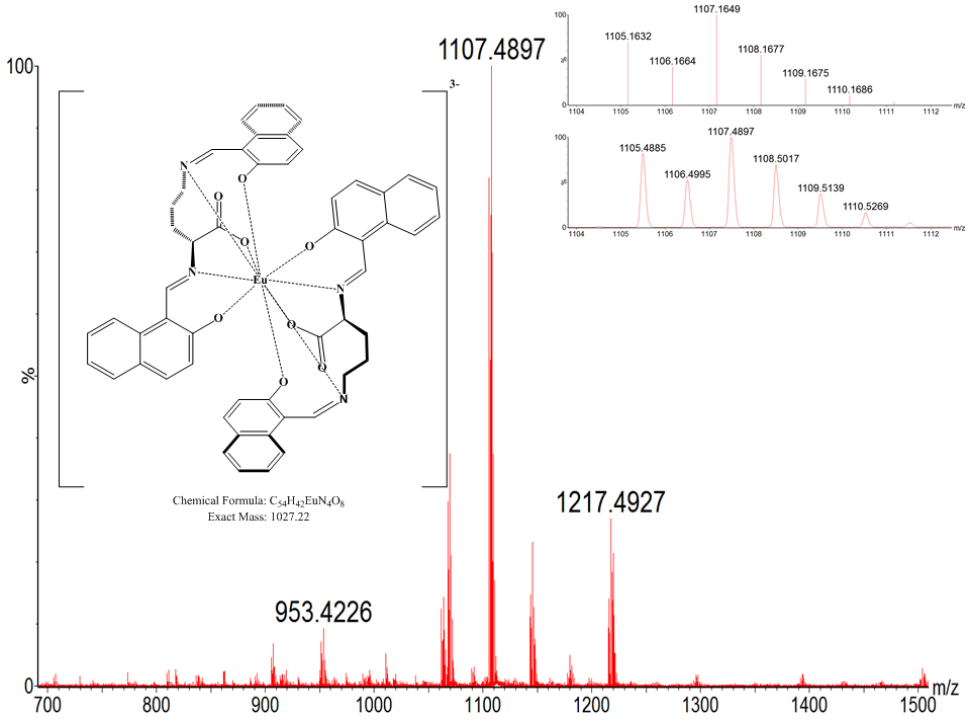

Figure S3.5 ESI-HRMS of $[Eu\mathbf{L}^{II}_2]^{3-}$; $[[Eu\mathbf{L}^{II}_2] + H_2 + K_2]]^+$ in methanol from 700 – 1500 *m/z*. Inset: On the left, the predicted structure and molar mass of $[Eu\mathbf{L}^{II}_2]^{3-}$. On the right, the predicted (above) and experimental (bellow) isotopic patterns of $[Eu\mathbf{L}^{II}_2] + H_2 + K_2]^+$.

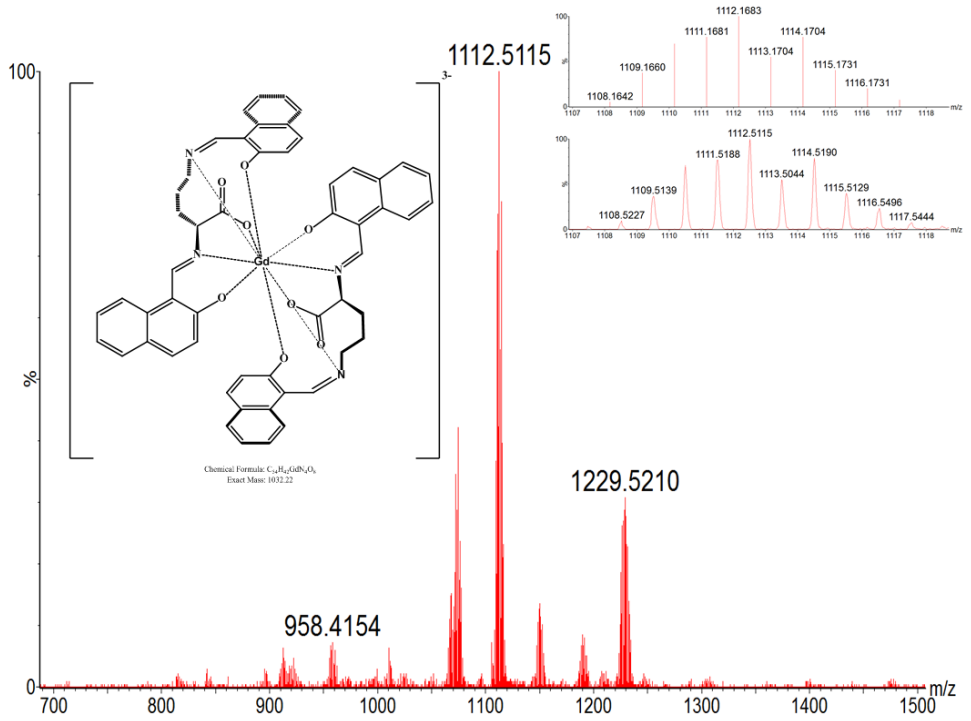

Figure S3.6 ESI-HRMS of $[Gd\mathbf{L}^{II}_2]^{3-}$; $[[Gd\mathbf{L}^{II}_2] + H_2 + K_2]]^+$ in methanol from 700 – 1500 *m/z*. Inset: On the left, the predicted structure and molar mass of $[Gd\mathbf{L}^{II}_2]^{3-}$. On the right, the predicted (above) and experimental (bellow) isotopic patterns of $[Gd\mathbf{L}^{II}_2] + H_2 + K_2]^+$.

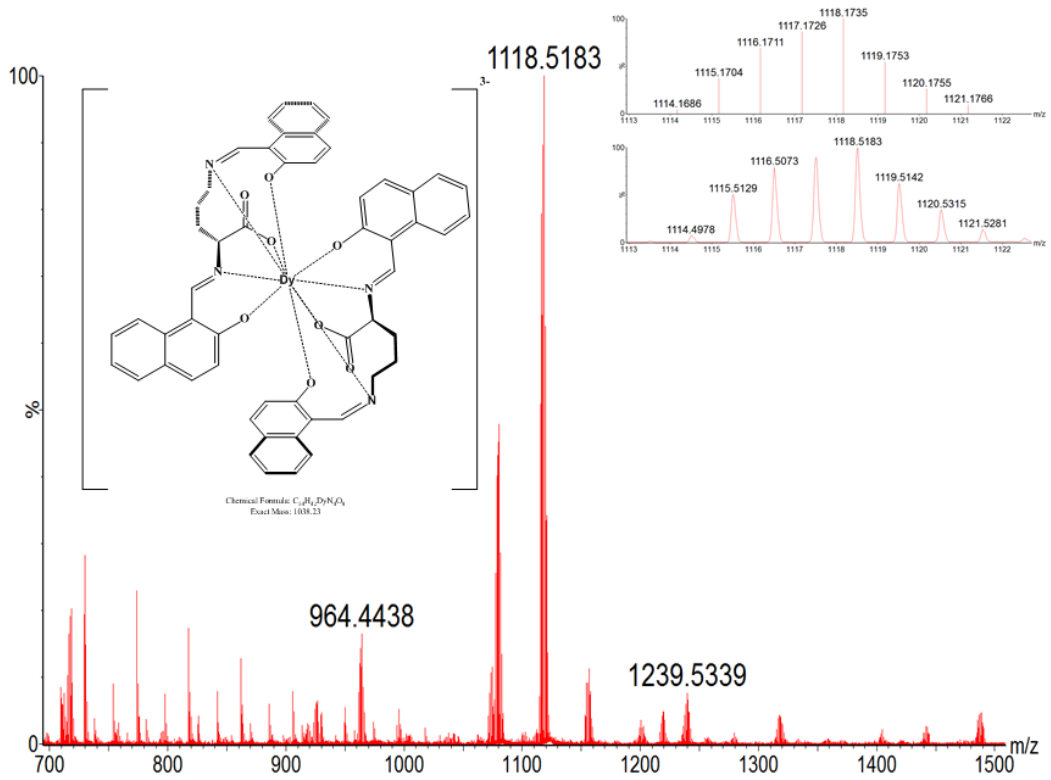

Figure S3.7 ESI-HRMS of $[Dy\mathbf{L}^{II}_2)]^{3-}$; $[[Dy\mathbf{L}^{II}_2] + H_2 + K_2]]^{+}$ in methanol from 700 – 1500 *m/z*. Inset: On the left, the predicted structure and molar mass of $[Dy\mathbf{L}^{II}_2)]^{3-}$. On the right, the predicted (above) and experimental (bellow) isotopic patterns of $[[Dy\mathbf{L}^{II}_2] + H_2 + K_2]]^{+}$.

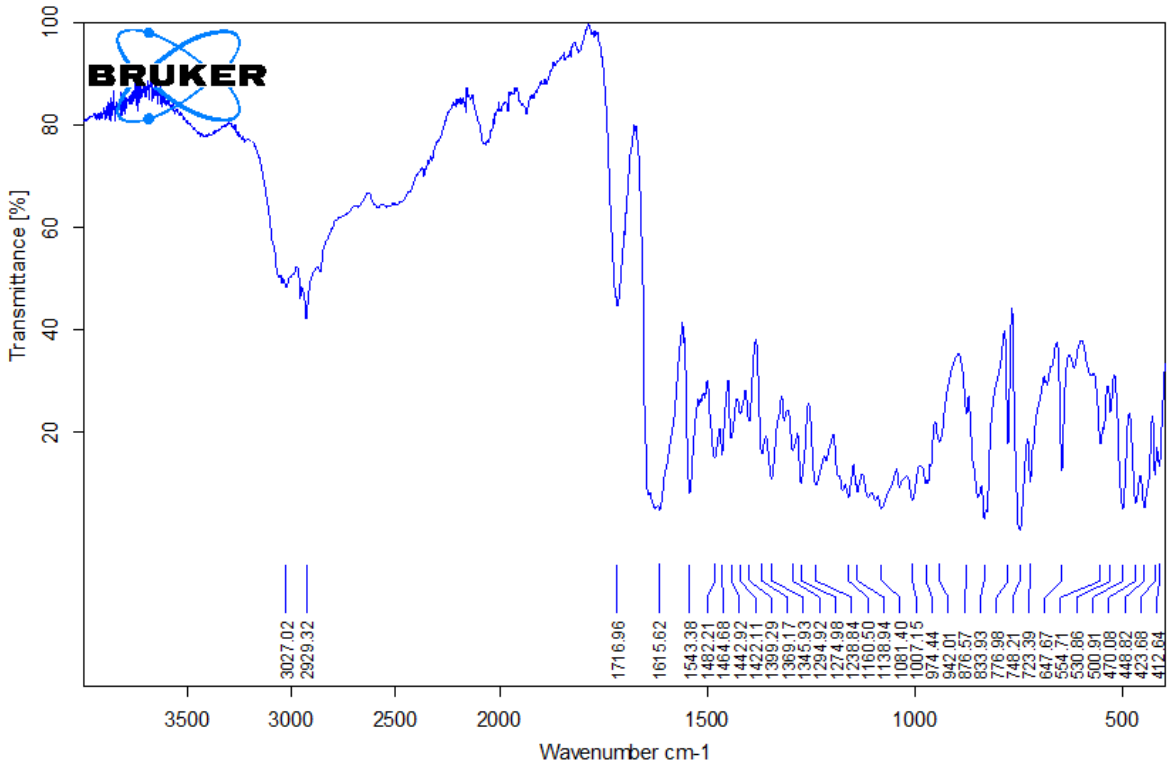

Figure S3.8 FT-IR spectrum of $H_3\mathbf{L}^{II}$.

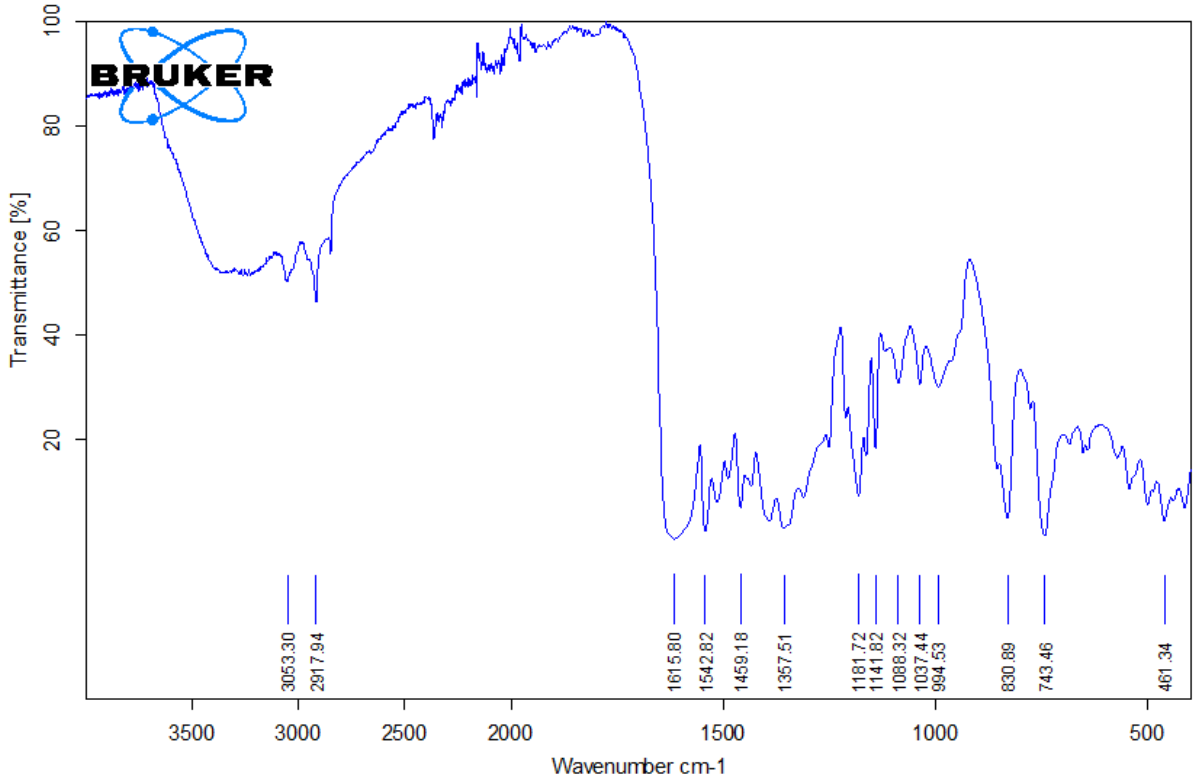

Figure S3.9 FT-IR spectrum of $[Eu\mathbf{L}^{II}_2]^{3-}$.

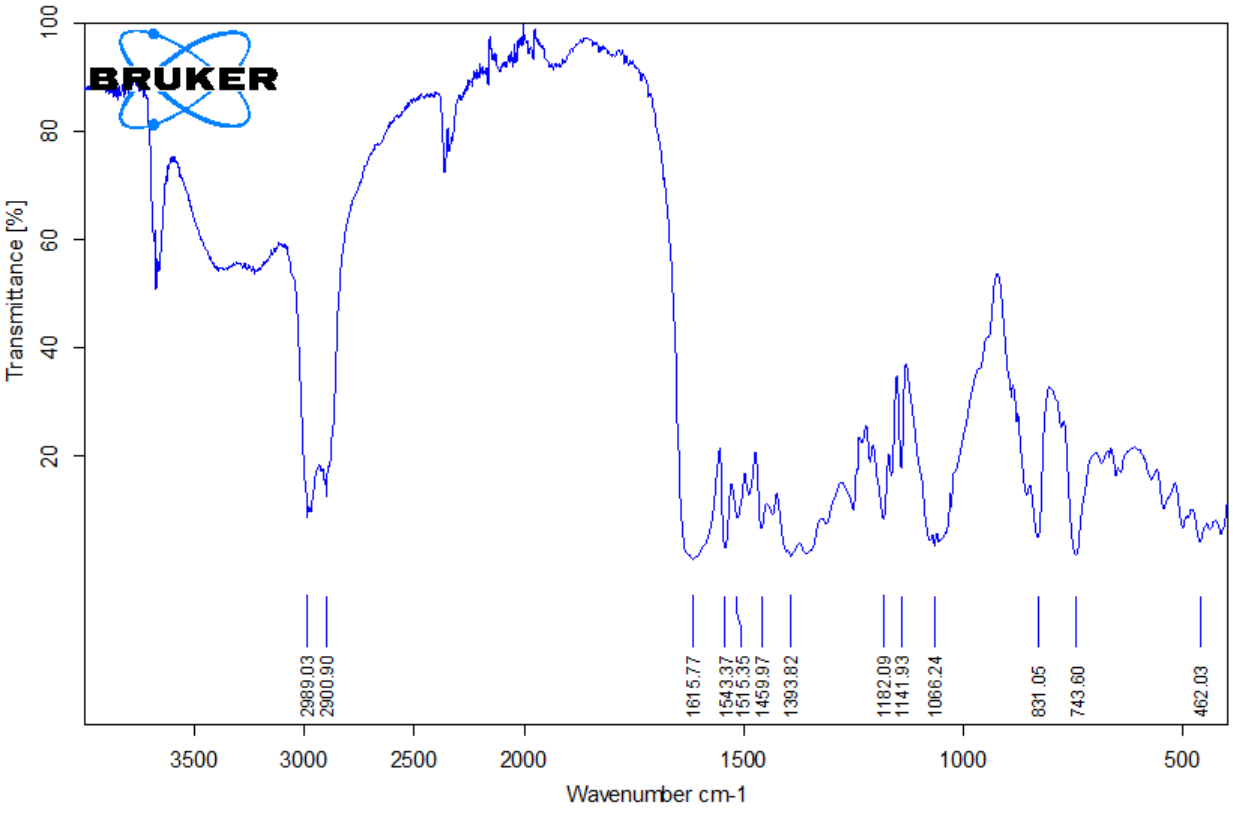

Figure S3.10 FT-IR spectrum of $[Gd\mathbf{L}^{II}_2]^{3-}$.

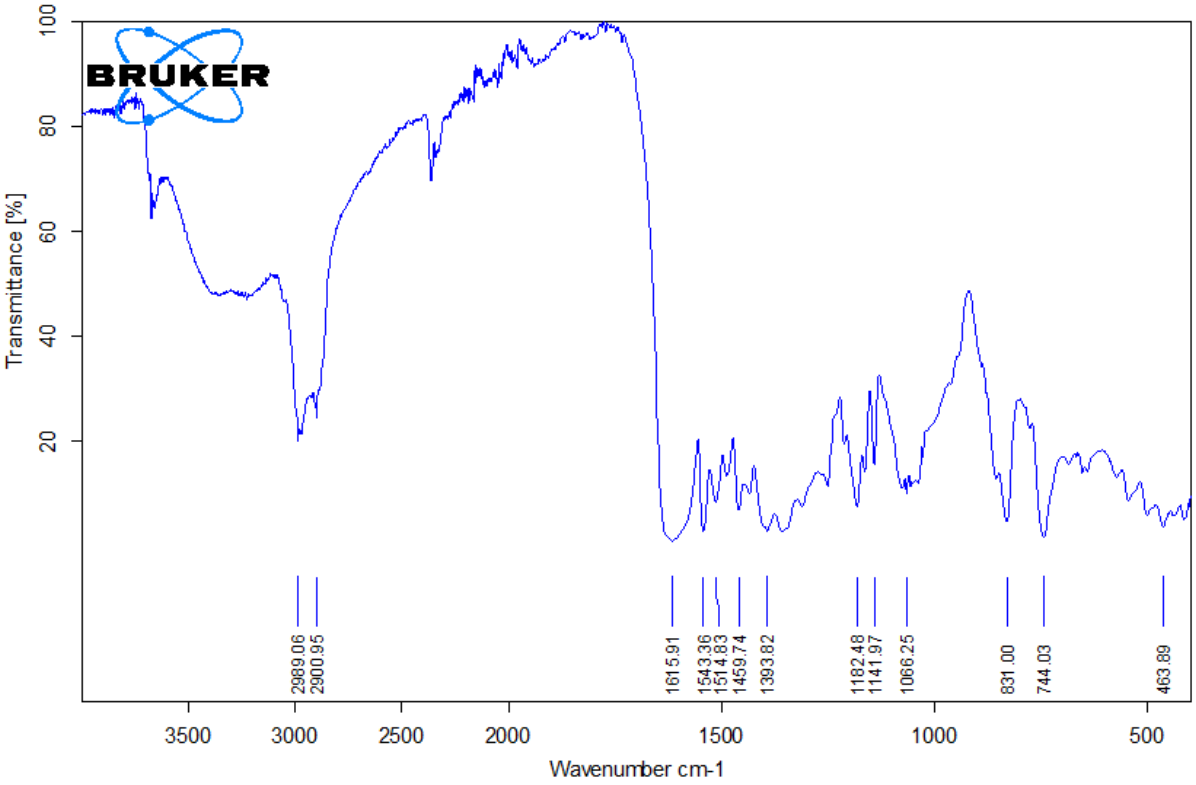

Figure S3.11 FT-IR spectrum of $[Dy\mathbf{L}^{II}_2]^{3-}$.

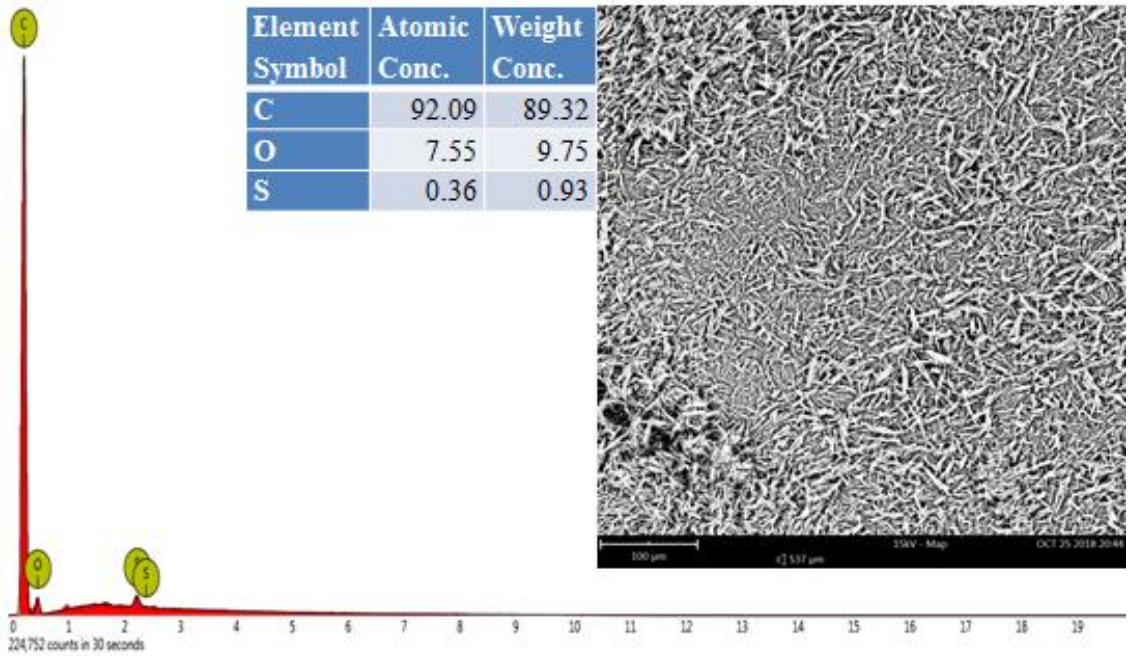

Figure S3.12 EDS spectrum of $H_3\mathbf{L}^{II}$. Inset: At the top, the elemental composition of $H_3\mathbf{L}^{II}$ and on the right, backscattered SEM micrograph of $H_3\mathbf{L}^{II}$ at 500 x magnification**.**

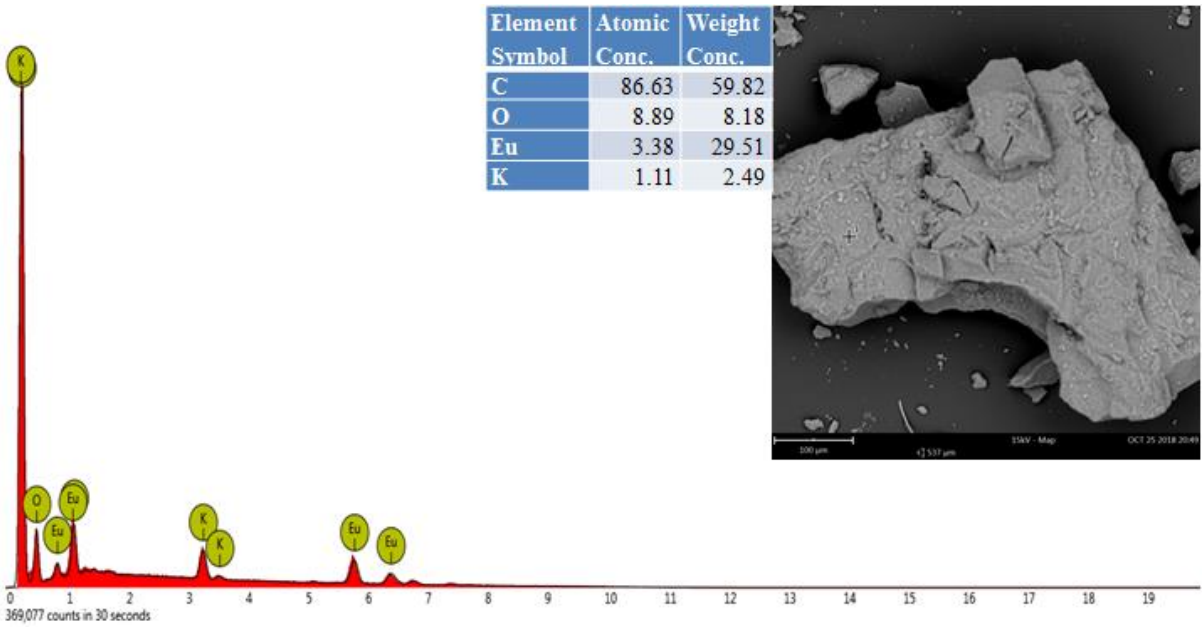

Figure S3.13 EDS spectrum of $[Eu\mathbf{L}^{II}_2]^{3-}$. Inset: At the top, the elemental composition of $[Eu\mathbf{L}^{II}_2]^{3-}$and on the right, backscattered SEM micrograph of $[Eu\mathbf{L}^{II}_2]^{3-}$ at 500 x magnification.

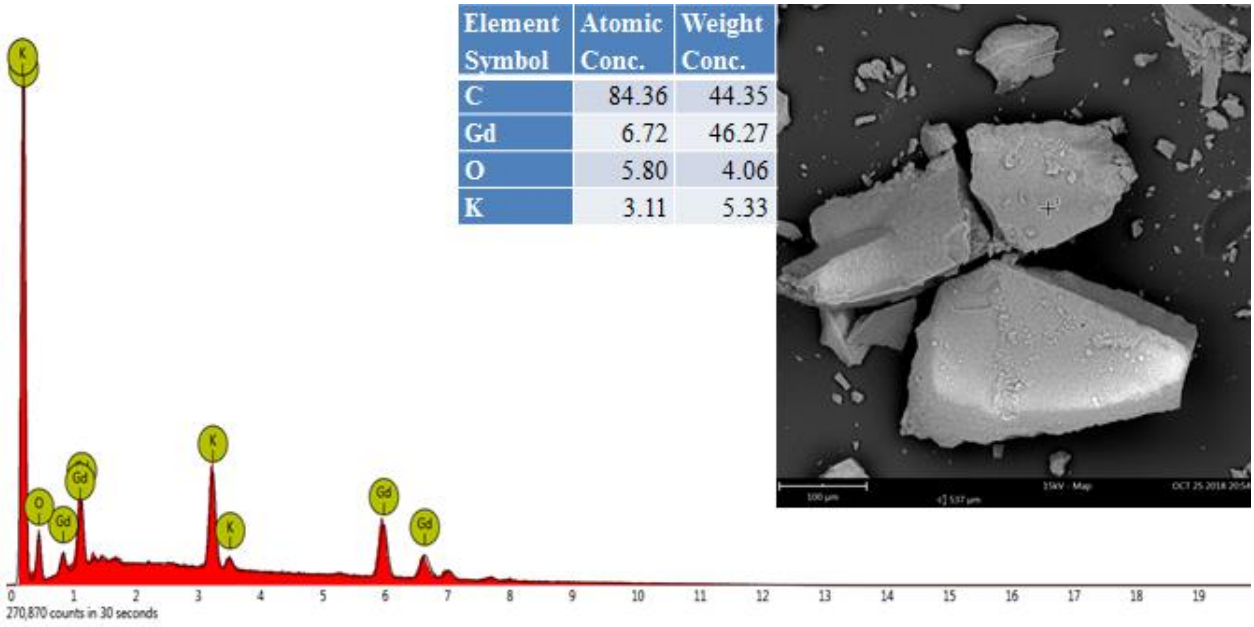

Figure S3.14 EDS spectrum of $[Gd\mathbf{L}^{II}_2]^{3-}$. Inset: At the top, the elemental composition of $[Gd\mathbf{L}^{II}_2]^{3-}$and on the right, backscattered SEM micrograph of $[Gd\mathbf{L}^{II}_2]^{3-}$ at 500 x magnification**.**

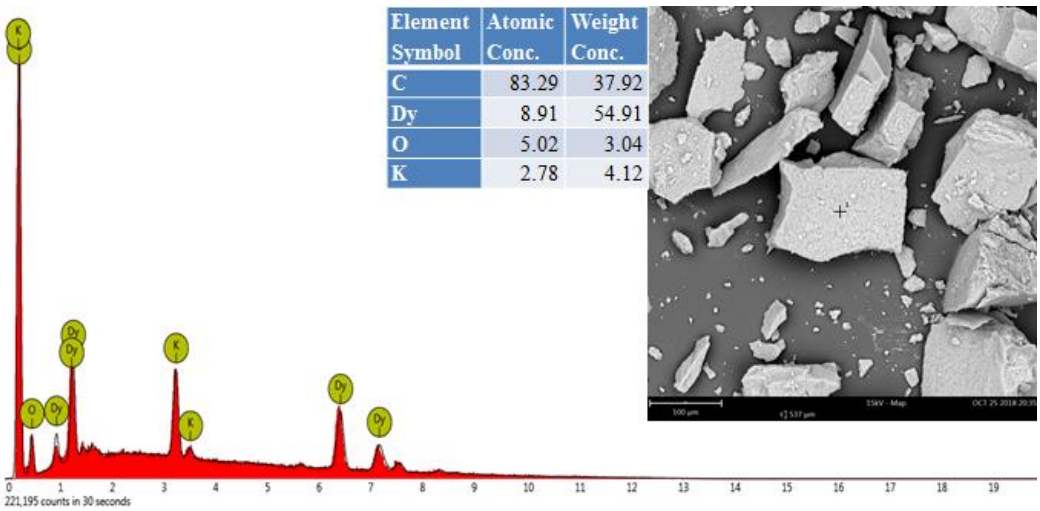

Figure S3.15 EDS spectrum of $[Dy\mathbf{L}^{II}_2)]^{3-}$. Inset: At the top, the elemental composition of $[Dy\mathbf{L}^{II}_2)]^{3-}$and on the right, backscattered SEM micrograph of $[Dy\mathbf{L}^{II}_2)]^{3-}$ at 500 x magnification.

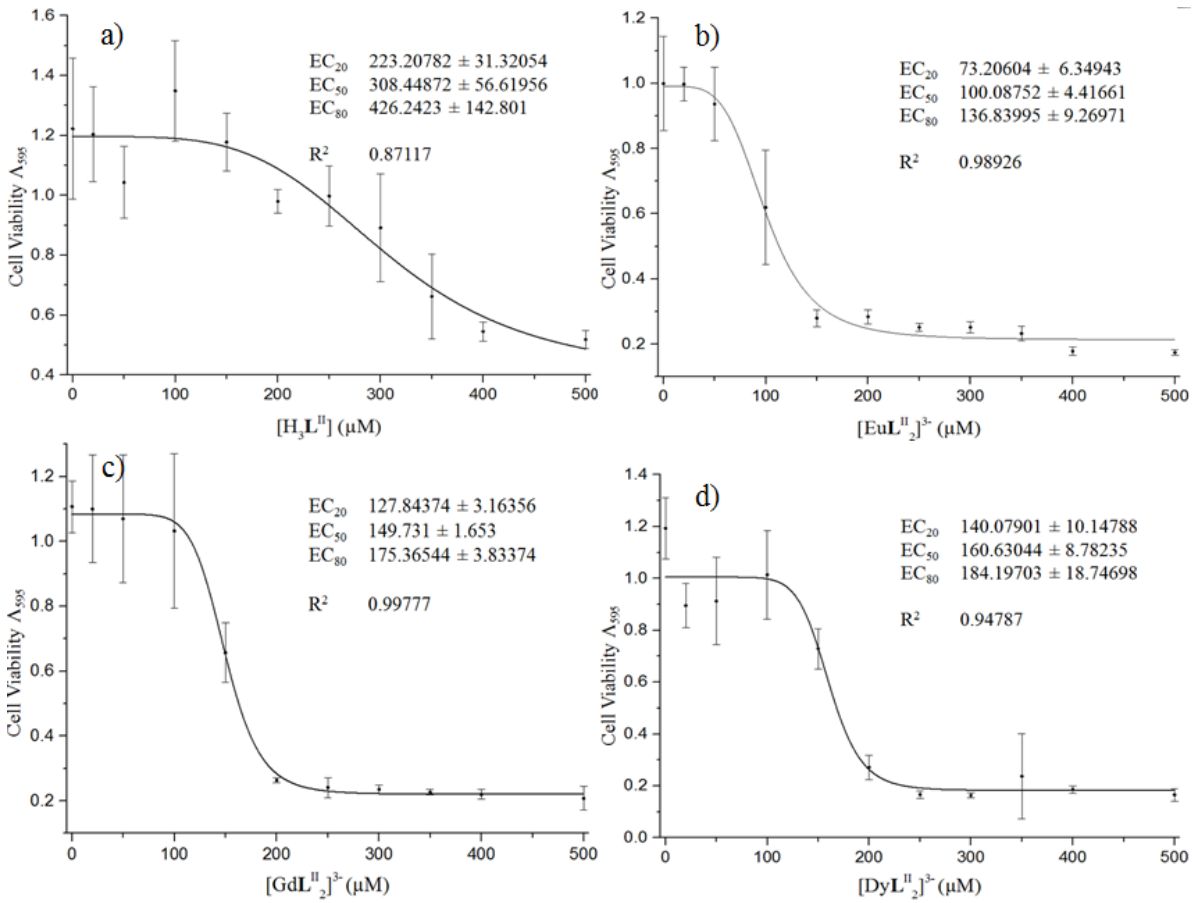

Figure S3.16 Cell viability of 1321N1 astrocytoma cells treated with varying concentrations (0–500 μM) of a.) $H_3\mathbf{L}^{II}$, b.) $[Eu\mathbf{L}^{II}_2]^{3-}$, c.) $[Gd\mathbf{L}^{II}_2]^{3-}$ and d.) $[Dy\mathbf{L}^{II}_2]^{3-}$ for 24 h incubation periods, determined by an MTT reduction assay. Λ = 595 nm, Error bars = STD (n = 6).

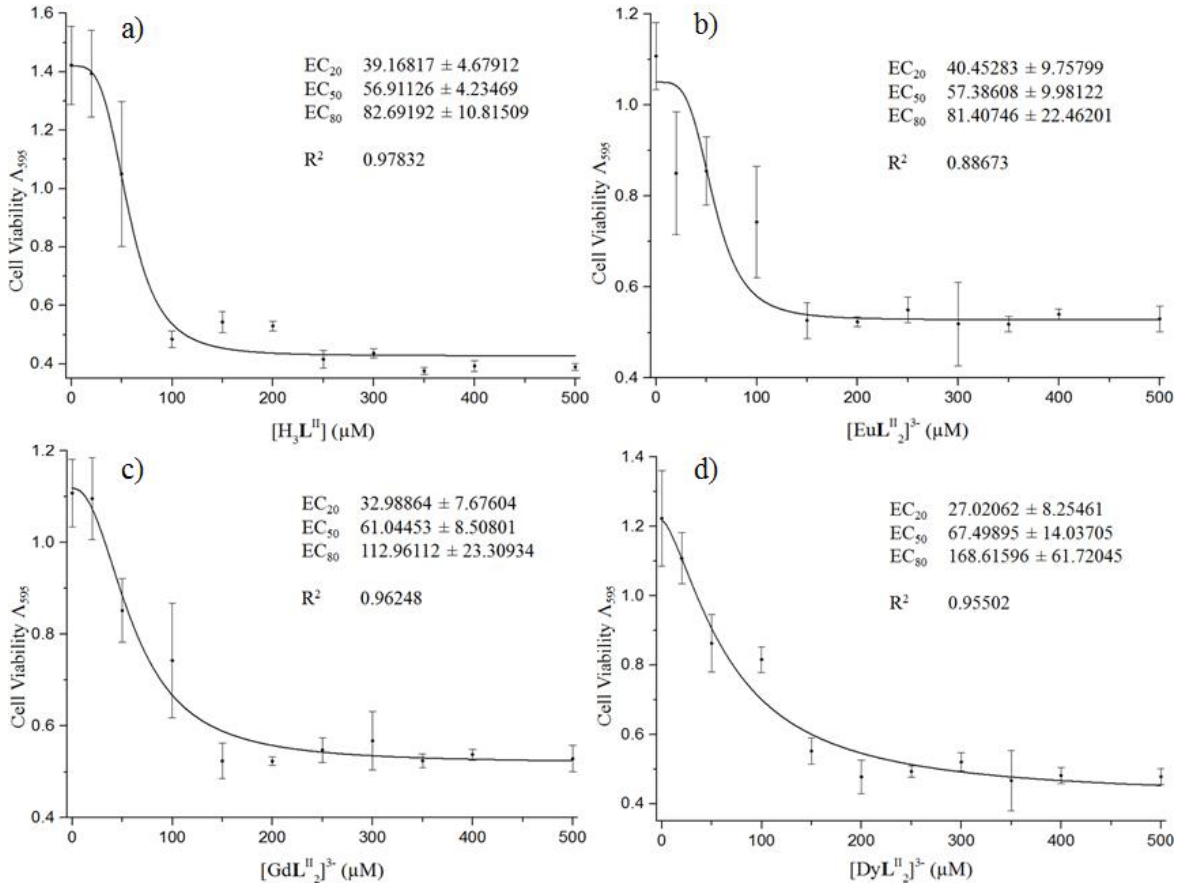

Figure S3.17 Cell viability of L6 myoblast cells treated with varying concentrations (0–500 μM) of a.) $H_3\mathbf{L}^{II}$, b.) $[Eu\mathbf{L}^{II}_2]^{3-}$, c.) $[Gd\mathbf{L}^{II}_2]^{3-}$ and d.) $[Dy\mathbf{L}^{II}_2]^{3-}$ for 24 h incubation periods, determined by an MTT reduction assay. Λ = 595 nm, Error bars = STD (n = 6).

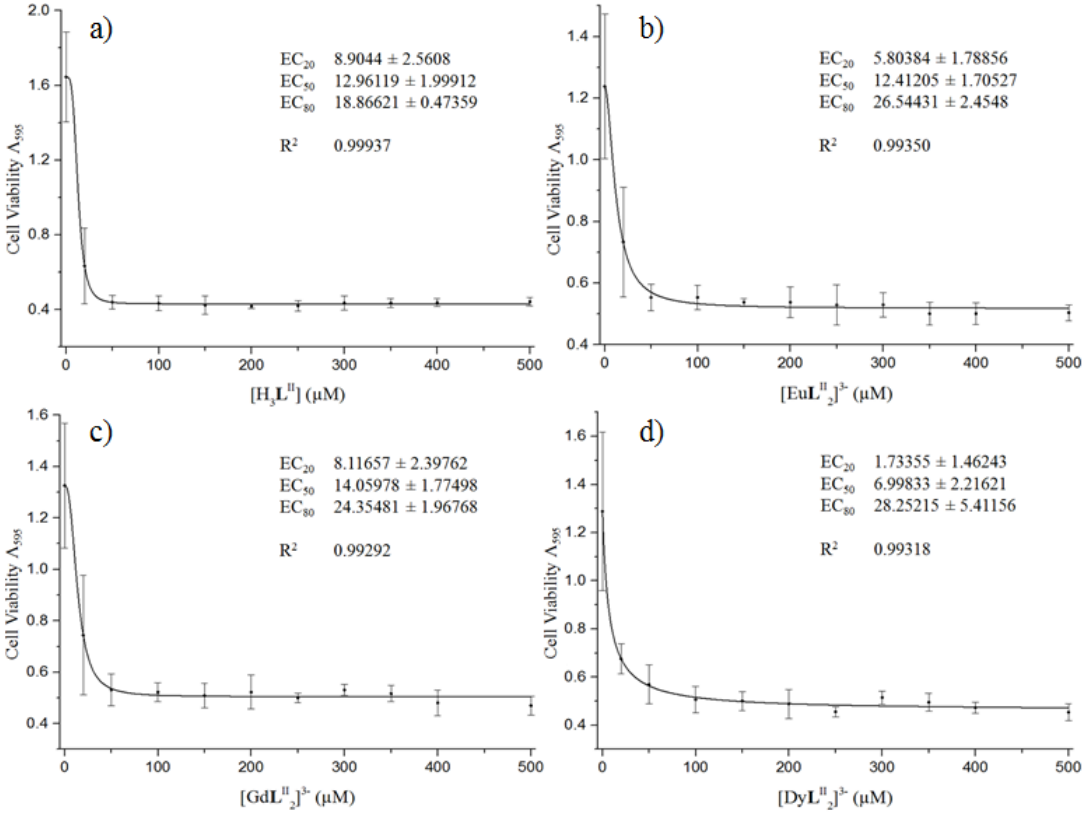

Figure S3.18 Cell viability of A2780 carcinoma cells treated with varying concentrations (0–500 μM) of a.) $H_3\mathbf{L}^{II}$, b.) $[Eu\mathbf{L}^{II}_2]^{3-}$, c.) $[Gd\mathbf{L}^{II}_2]^{3-}$ and d.) $[Dy\mathbf{L}^{II}_2]^{3-}$ for 24 h incubation periods, determined by an MTT reduction assay. Λ = 595 nm, Error bars = STD (n = 6).

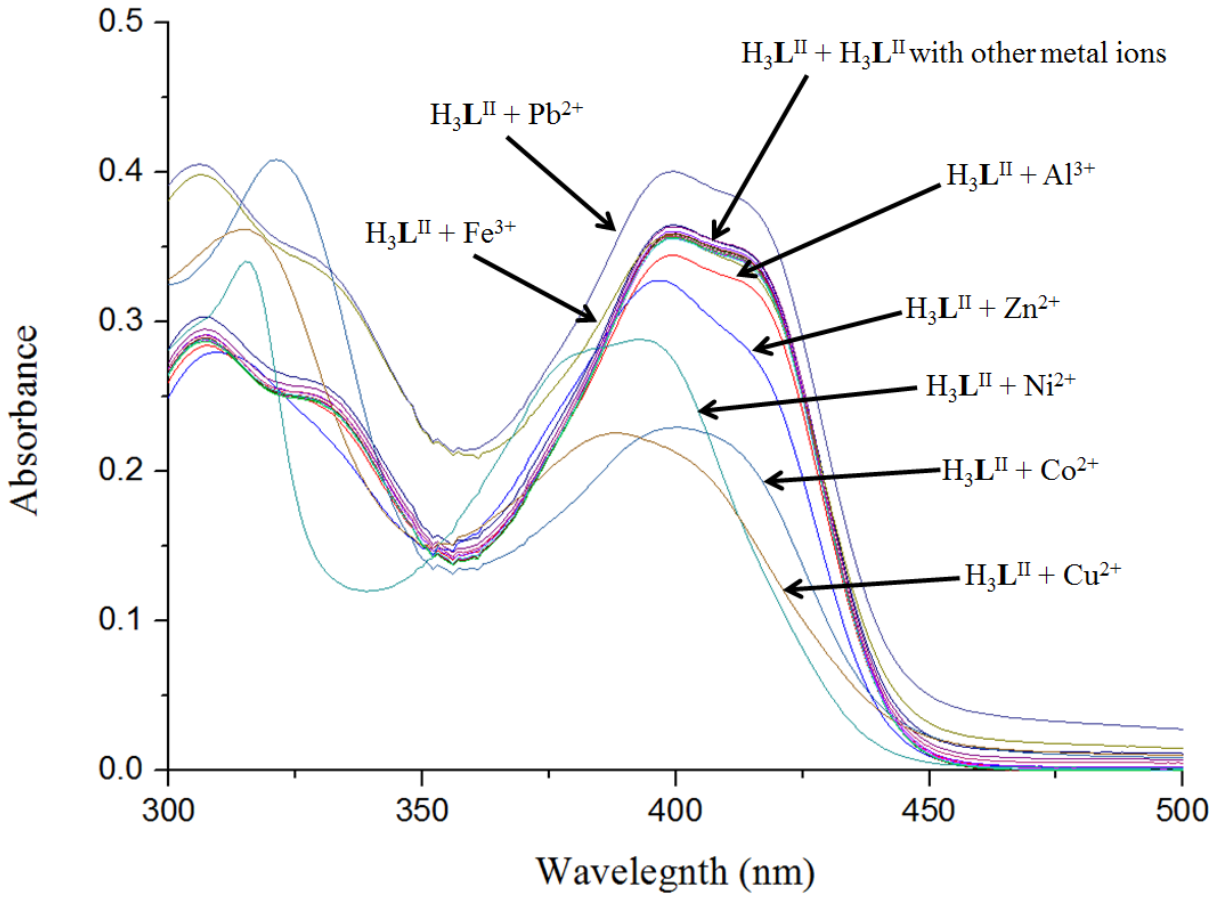

Figure S3.19 The UV-vis spectrum (300-500 nm) of the metal scan of $H_3\mathbf{L}^{II}$ and $H_3\mathbf{L}^{II}$ in the presence of various metal ions.

Chapter 4 – A Selective 'Turn-on' Fluorescent Sensor for Detecting Al^{3+} in Aqueous Solutions and Intracellular Environments

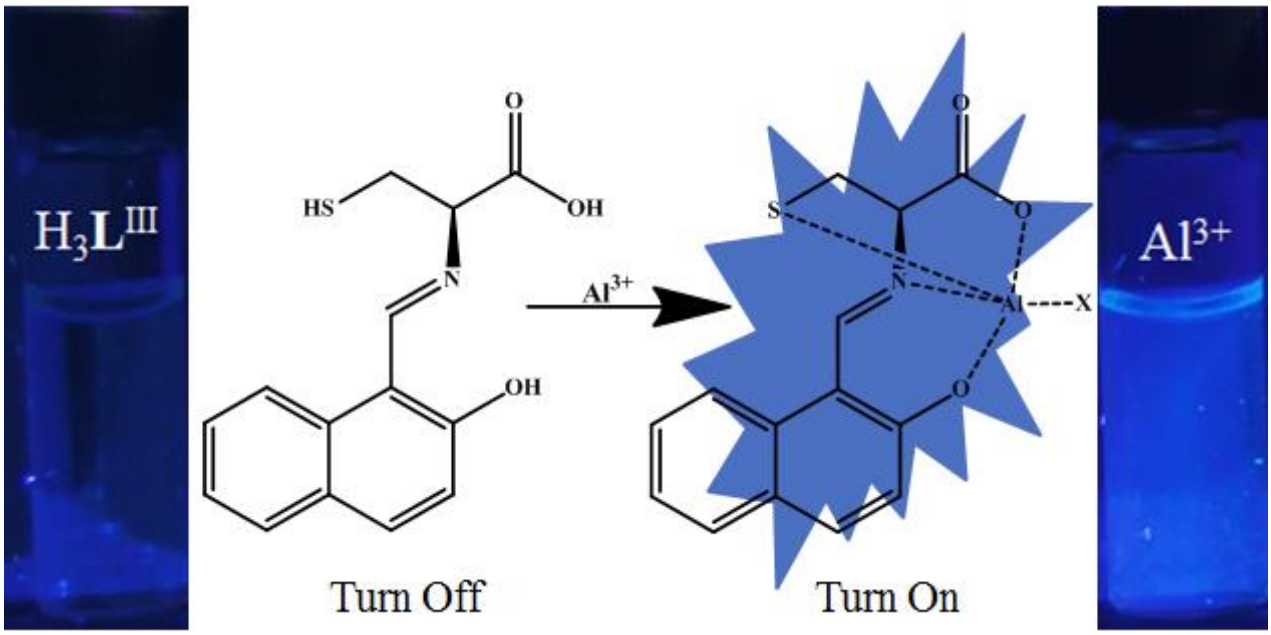

4.1 Abstract

Despite its toxicity; organisms are exposed to aluminium by an array of household appliances, utensils, cosmetics and pharmaceuticals. Aluminium has some links to Alzheimer's disease (AD); however, many of these claims are frequently disputed. At a low pH, aluminium is readily solubilised in water and is potentially toxic to wildlife either directly or due to biomagnification. Therefore, the need to study the effects of Al^{3+} is imperative to enhance the understanding of its potential roles in biology. Fluorescent sensors are in great demand for the study metal ions in bioinorganic chemistry. However, many of the current Al^{3+} fluorescent sensors come with their limitations. Herein, we synthesise and characterise ligand ($H_3\mathbf{L}^{III}$) via the Schiff base condensation reaction between L-cysteine and 2-hydroxy-1-naphthaldehyde and analyse its potential as an Al^{3+} 'turn-on' fluorescent enhancement sensor in biological systems. $H_3\mathbf{L}^{III}$ detects Al^{3+} with a 17-fold fluorescent enhancement which exhibits little effect in the coexistence of competitively binding metals. $H_3\mathbf{L}^{III}$ demonstrates a 1:1 ligand-to-metal stoichiometry with a low limit of detection (LoD) of 3.46 nM. $H_3\mathbf{L}^{III}$ observes no effect on cell viability and is able to detect Al^{3+} in 321N1 astrocytoma without the need for additional Al^{3+}.

4.2 Introduction

Aluminium is the most abundant metal in the lithosphere, constituting to 8.3% of its total mass.[1] Aluminium is also prevalent within humans and its overexposure has some links with the development of Alzheimer's disease (AD).[2-5] According to the Department of Agriculture and Food, Western Australian government, aluminium sensitive plants require only 2-5 ppm of Al^{3+} to be toxic to the roots of such plants. Within acidic environments, aluminium is readily solubilised due to its oxidation into Aluminium oxide. Once soluble, aluminium is then potentially toxic to organisms within its adjacent environment. This is particularly problematic within industrialised areas, where chemical spills, as well as, the formation of acid rain result in lowering pH, allowing aluminium to dissolve, ruining agriculture and harming lifeforms.[6-8] Recently, aluminium has acquired much interest from scientists within medical fields for its possible role in the development of AD.[9] As many of these claims come with contrary counter-arguments, the demand for developing more advanced methods of sensing Al^{3+} is constantly on the rise. Much attention has therefore been focused on the development of Al^{3+} fluorescent sensors for their biological applications.[10-12] Unfortunately, many of the current Al^{3+} sensors are marked with their limitations. Many that currently exist are limited by complicated synthetic pathways with low yields and are inappropriate for biological applications due to their toxicity or lack of testing in biological systems.[13,14] Therefore, the development of new fluorescent sensors for Al^{3+} is imperative to enhance the understanding of Al^{3+} and its role in biology.

Ligand ($H_3\mathbf{L}^{III}$) is synthesised via the Schiff base condensation reaction between L-cysteine and 2-hydroxy-1-naphthaldehyde. L-cysteine is a water-soluble amino acid with high binding affinity to metal ions.[15-17] 2-hydroxy-1-naphthaldehyde is a prevalent fluorophore, commonly explored for its role in the design of fluorescent sensors.[18] Schiff bases are wildly exploited for their unique properties. Due to a lone pair of electrons upon their imine functional group, photo-induced electron transfer (PET) is a prevalent method for inducing fluorescent enhancement, hence, 'turn-on' fluorescent sensors.[19-21]

4.3 Results and Discussion

4.3.1 Synthesis and Structure of $H_3\mathbf{L}^{III}$

$H_3\mathbf{L}^{III}$ was synthesised from the condensation of L-cysteine and 2-hydroxy-1-naphthaldehyde at room temperature for 24 h in methanol upon the presence of a catalytic amount of glacial acetic acid (Fig. 4.1). It was then characterised via ^{1}H NMR and ^{13}CNMR, Electrospray Ionisation - High Resolution Mass Spectrometry (ESI-HRMS), FT-IR and simultaneous thermal analysis (STA). NMR and STA data indicated the synthesis of two products.

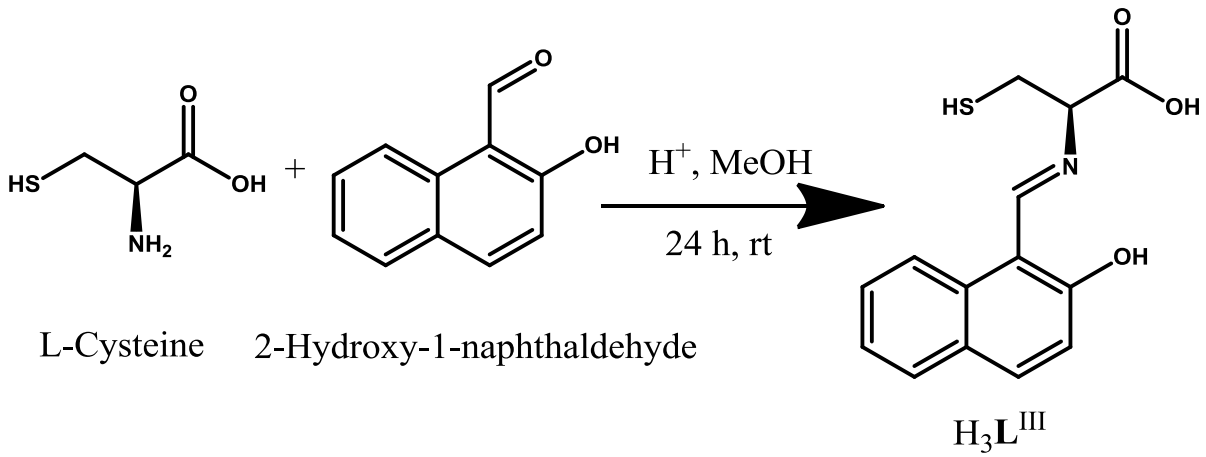

Figure 4.1 Synthesis of $H_3\mathbf{L}^{III}$.

4.3.2 Screening of Metal Cations

$H_3\mathbf{L}^{III}$ was examined by a UV-visible spectrophotometer (UV-vis) indicating a peak maxima of 414 nm. $H_3\mathbf{L}^{III}$ was then scanned in the presence of various metal ions (2 eq.) indicating interaction with Al^{3+}, Fe^{3+}, Co^{2+}, Ni^{2+}, Cu^{2+} and Pb^{2+}. A fluorescent spectrum of $H_3\mathbf{L}^{III}$ was obtained when excited at 395 nm indicating a broad, however, mostly non-fluorescent peak of $H_3\mathbf{L}^{III}$ at 456 nm. $H_3\mathbf{L}^{III}$ was then scanned in the presence of various metal ions (2 eq.). A significant fluorescent enhancement response of ~17-fold is observed at 437 nm (blue) when $H_3\mathbf{L}^{III}$ is in the presence of Al^{3+} (2 eq.). A weak fluorescent enhancement is also exhibited at 455 nm when in the presence of Zn^{2+} (2 eq.) and very weak fluorescent

enhancement of Hg^{2+} (2 eq.) at 456. Weak quenching of $H_3\mathbf{L}^{III}$ occurs when in the presence of Fe^{3+} (2 eq.). Results demonstrate that $H_3\mathbf{L}^{III}$ has a significant and selectivity fluorescent response to Al^{3+} over other metal ions. The stability of $H_3\mathbf{L}^{III}$ with Al^{3+} was then measured as a function of time where fluorescence intensity plateaued at ~300 min (Fig. 4.2).

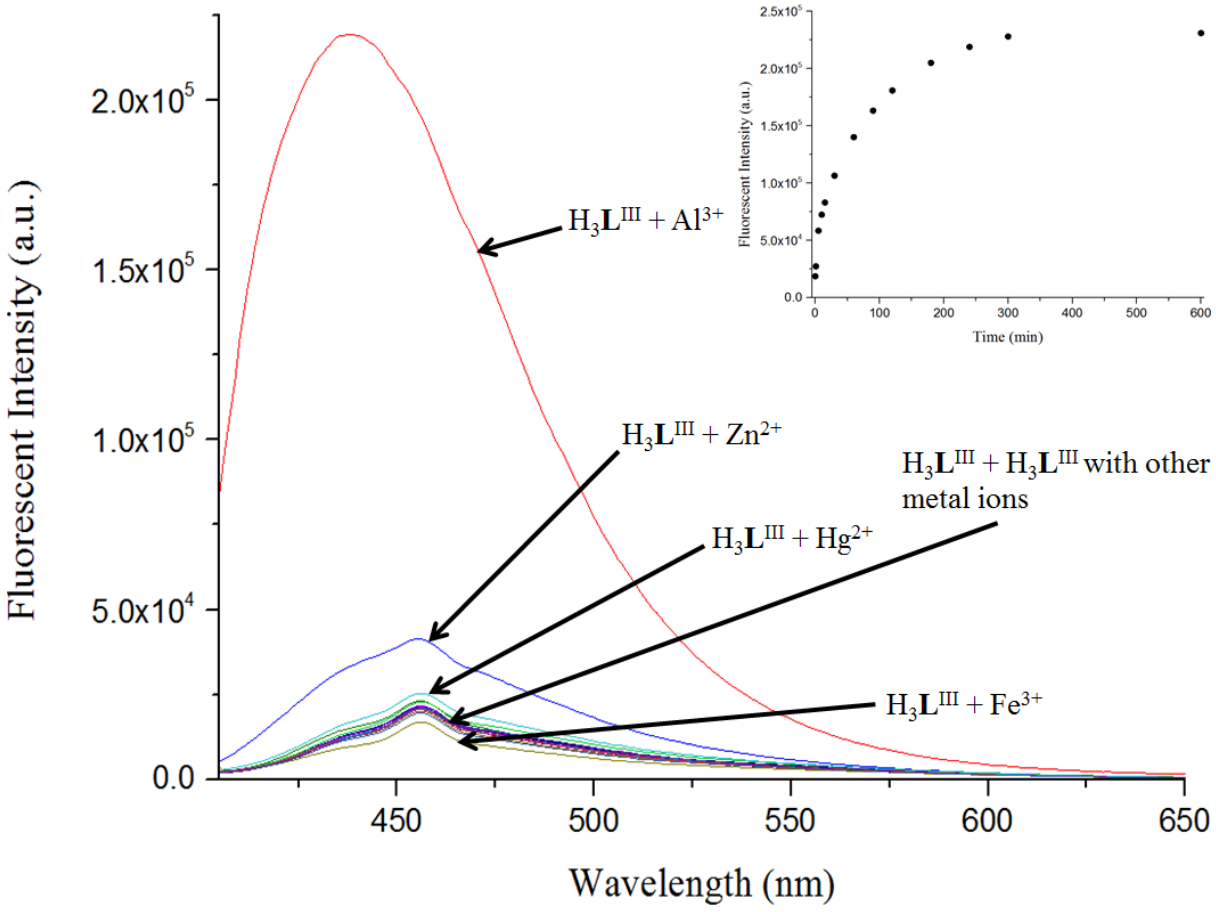

Figure 4.2 The fluorescence spectrum of $H_3\mathbf{L}^{III}$ (20 μM) in the presence of various metal ions (2 eq.) in 20 mM HEPES, 5 mM GSH water solution at pH = 7.4. Inset: A scatter plot of the fluorescence of $H_3\mathbf{L}^{III}$ (20 μM) in the presence of 2 eq. Al^{3+} in 20 mM HEPES, 5 mM GSH, Milli-Q water solution at pH = 7.4, as a function of time (0-600 min).

4.3.3 Naked Eye; Al^{3+} Detection

The contrast in fluorescence intensities between $H_3\mathbf{L}^{III}$, $H_3\mathbf{L}^{III}$ and Al^{3+}, and $H_3\mathbf{L}^{III}$ with other metal ions can be observed under the naked eye when excited with ultraviolet (UV) light at 365 nm (Fig. 4.3). As observed $H_3\mathbf{L}^{III}$ in the presence of Al^{3+} emits light at a blue colour which is significantly brighter than that of $H_3\mathbf{L}^{III}$ or $H_3\mathbf{L}^{III}$ in the presence of other

metal ions. Mild fluorescent enhancement can also be observed when $H_3\mathbf{L}^{III}$ is in the presence of Zn^{2+}, however, this is barely detectable. This pronounced fluorescent enhancement of $H_3\mathbf{L}^{III}$ at 437 nm when in the presence of Al^{3+} displays a high selectivity of $H_3\mathbf{L}^{III}$ to Al^{3+}. PET phenomenon, may explain the mechanism of how $H_3\mathbf{L}^{III}$ acts as a 'turn-on' fluorescent enhancer for Al^{3+}. Electrons from the imine nitrogen atom of the Schiff base may invoke contributions to PET, which quench the fluorescence intensity of $H_3\mathbf{L}^{III}$. However, when $H_3\mathbf{L}^{III}$ chelates to the strongly bound, diamagnetic Al^{3+}, the quenching is inhibited and the substantial fluorescence intensity of $H_3\mathbf{L}^{III}$ is restored.[19,22,23]

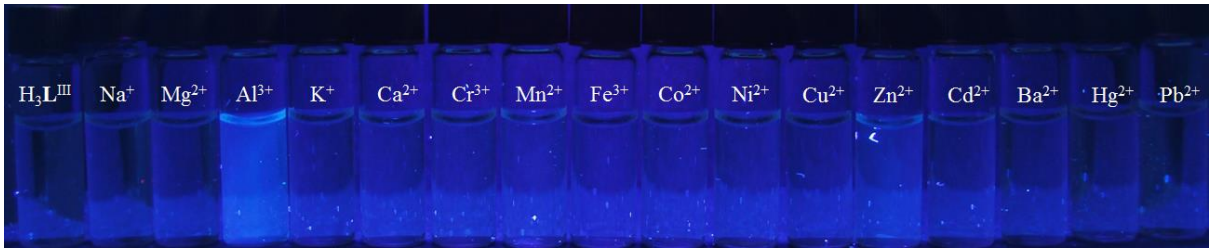

Figure 4.3 Detection of Al^{3+} by the naked eye using $H_3\mathbf{L}^{III}$ (20 μM) and $H_3\mathbf{L}^{III}$ in the presence of a series of metal cations (2 eq.) under UV light (365 nm) in 20 mM HEPES, 5 mM GSH, Milli-Q water solution at pH = 7.4.

4.3.4 Competing Metal Ion

Competing metal ion studies of $H_3\mathbf{L}^{III}$ and Al^{3+} in the coexistence of other metal ions was conducted in order to determine the capabilities of $H_3\mathbf{L}^{III}$ to sense Al^{3+} in the presence of potentially interfering ions. All samples were excited at 395 nm and fluorescent intensities were taken at 437 nm. $H_3\mathbf{L}^{III}$ and Al^{3+} in the coexistence of Cr^{3+}, Fe^{3+}, Co^{2+}, Ni^{2+}, Cu^{2+} and Hg^{2+} displayed some quenching, however, fluorescent intensity was still increased by ~5-fold (Cr^{3+}), ~2-fold (Fe^{3+}) and ~7-fold (Co^{2+}), ~8.5-fold (Ni^{2+}), ~7.5-fold (Cu^{2+}) and ~9.5-fold (Hg^{2+}) respectively, which are all clearly detectable. All other metal ions observed very minimal or no quenching effects (Fig. 4.4).

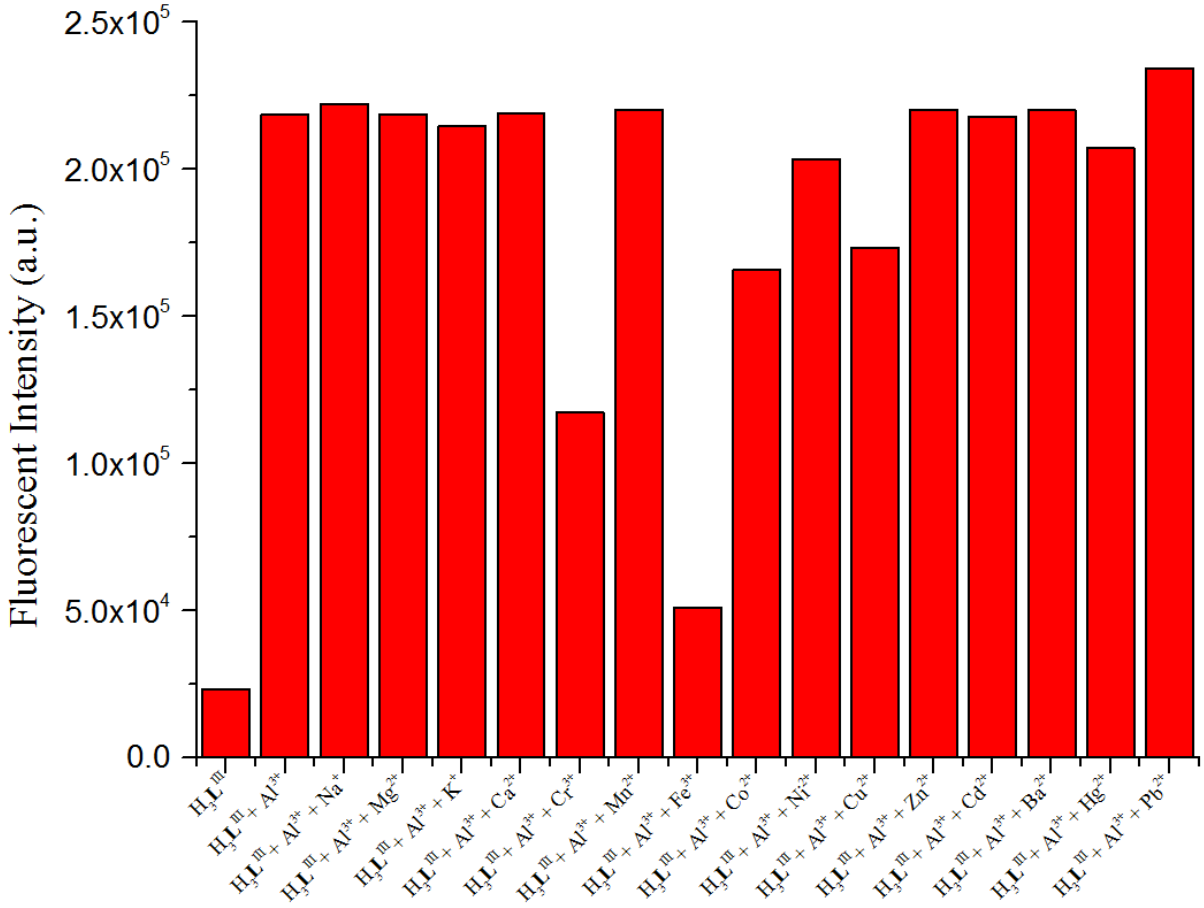

Figure 4.4 Fluorescence intensity of $H_3\mathbf{L}^{III}$ (20 µM) with Al^{3+} (2 eq.) under the coexistence of other metal cations (2 eq.) in 20 mM HEPES, 5 mM GSH, Milli-Q water solution at pH = 7.4. The samples were excited at 395 nm and fluorescent intensities were taken at 437 nm.

4.3.5 Limit of Detection (LoD)

A metal titration of Al^{3+} into $H_3\mathbf{L}^{III}$ (20 µM) was conducted which determined the limit of detection (LoD) of $H_3\mathbf{L}^{III}$ where all samples were excited at 395 nm and fluorescent intensities were taken at 437 nm. The titration determined a LoD of 3.46 nM and a limit of quantification (LoQ) of 15.5 nM. The metal titration also indicated a 1:1 ligand-to-metal stoichiometry (Fig. 4.5).

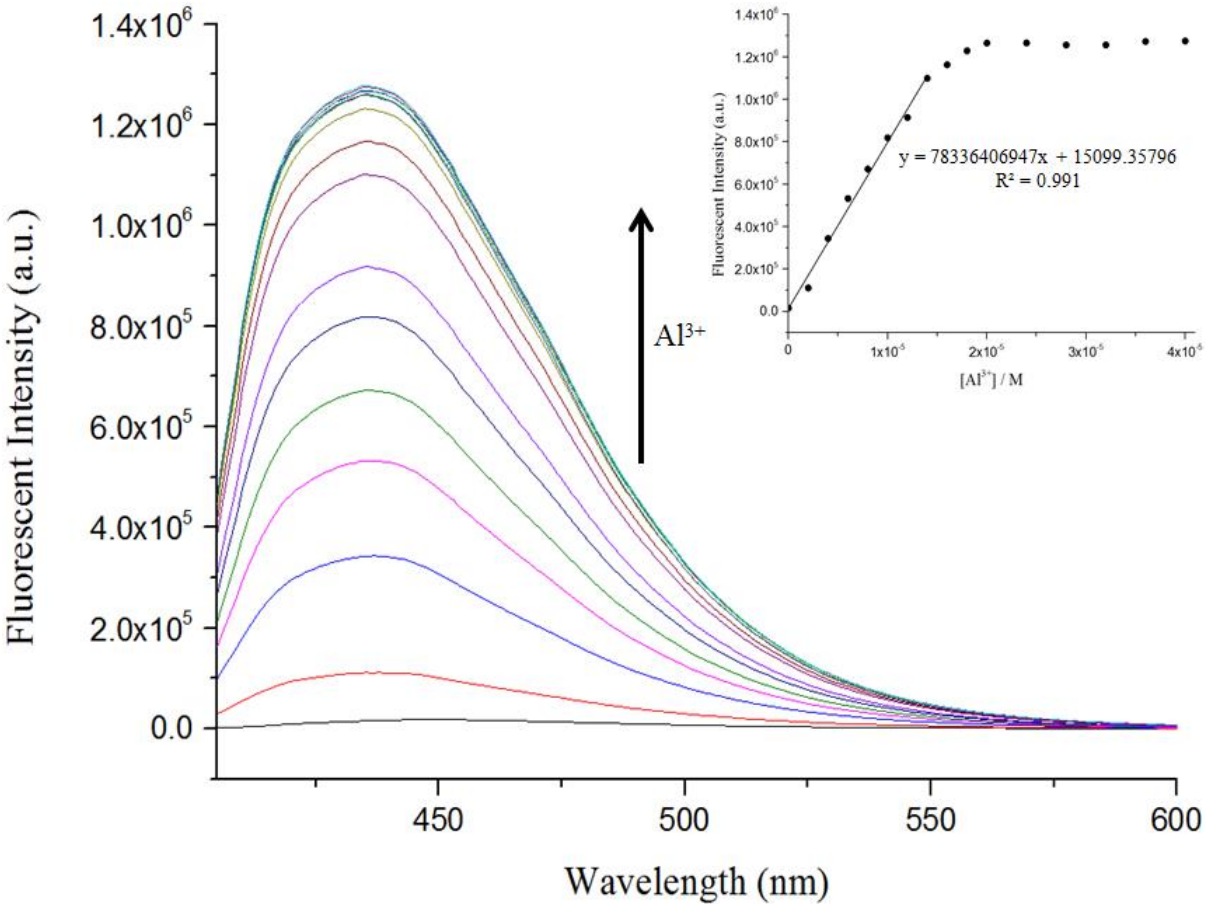

Figure 4.5 Fluorescence titration of $H_3\mathbf{L}^{III}$ upon addition of increasing amounts of Al^{3+} (0-2 eq.) in methanol. Inset: Fitting of the fluorescence titration curve of $H_3\mathbf{L}^{III}$ in methanol. LoD = 3.46 nM and LoQ = 15.5 nM determined by the following equations 3σ/m and 10σ/m respectively.

4.3.6 Job's plot

A Job's plot was conducted upon $H_3\mathbf{L}^{III}$ and Al^{3+} in methanol to a total concentration of 50 µM. Fluorescent intensities were excited at 395 nm and taken at 437 nm. The Job's plot intersect at a molar fraction of 0.50 matched data from MS and titration indicating a 1:1 ligand-to-metal stoichiometry (Fig. 4.6).

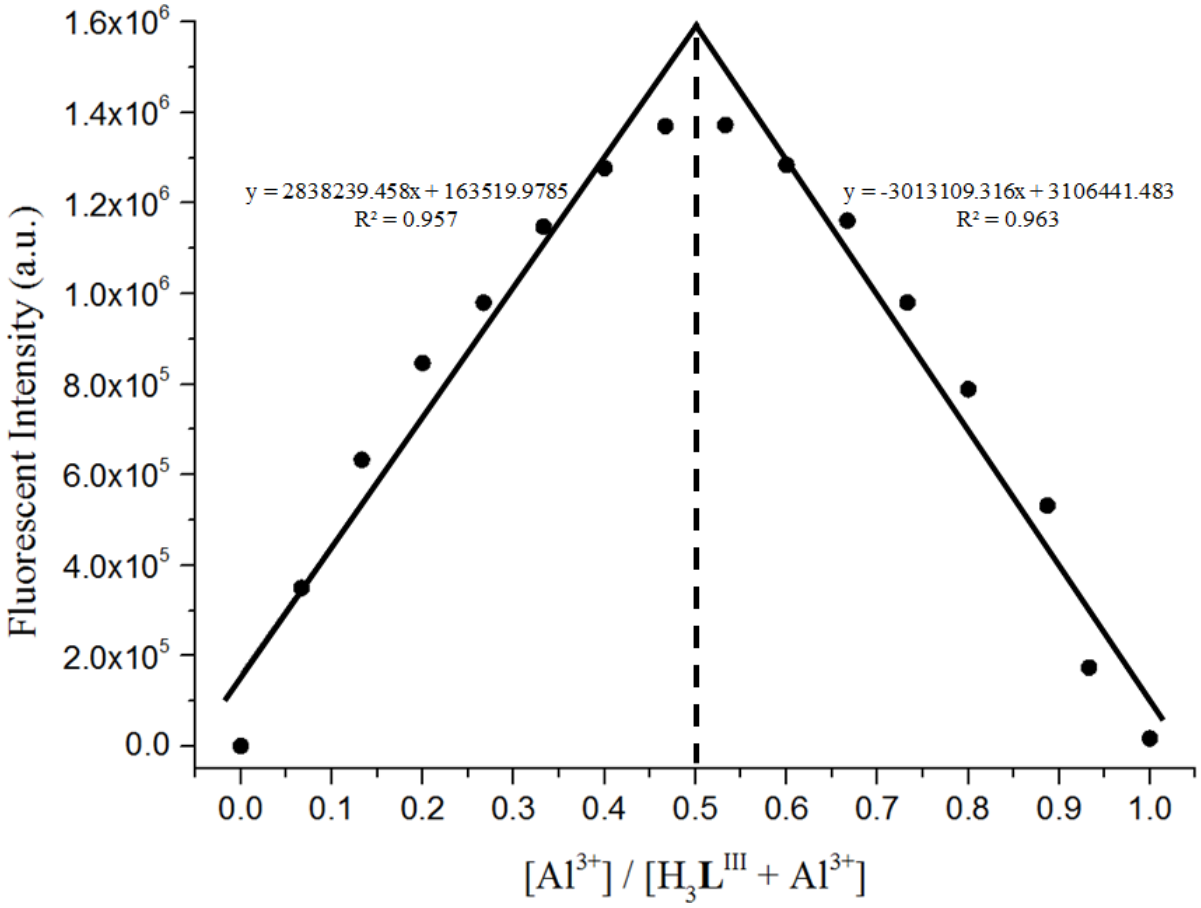

Figure 4.6 Job's plot of $H_3\mathbf{L}^{III}$ upon Al^{3+} at λ_{max} = 437 nm. Intersect of linear plots at molar fraction of 0.50, indicating a 1:1 ligand-to-metal stoichiometry.

4.4 Applications in Biological Systems

4.4.1 Detection of Al^{3+} in Different Water Samples

At a constant concentration of $H_3\mathbf{L}^{III}$ (20 µM), water samples of tap and Hawkesbury River water were spiked with varying concentrations (0 - 200 µM) of Al^{3+}. $H_3\mathbf{L}^{III}$ indicated strong fluorescent enhancement responses for Al^{3+} in tap water as well as Hawkesbury river water, in particularly beyond 200 µM (Fig. 4.7).

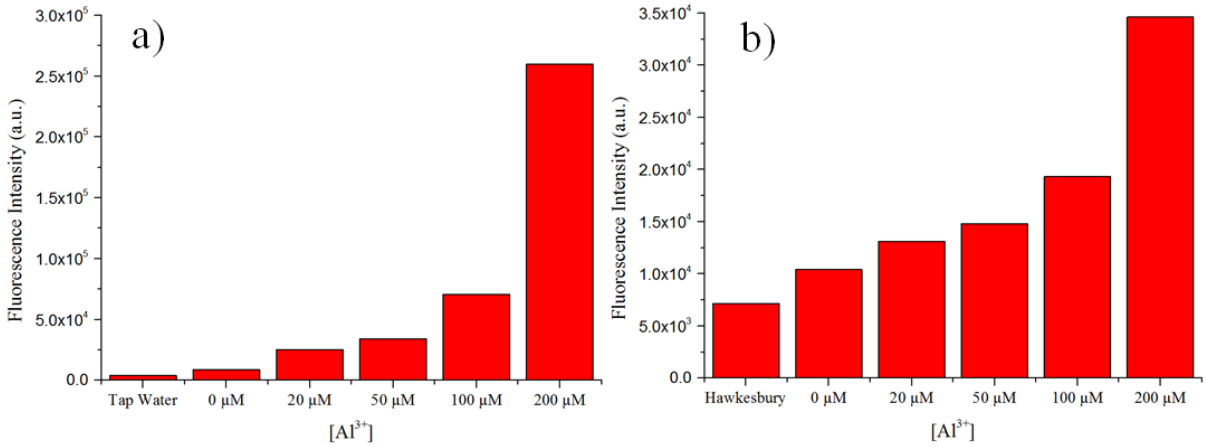

Figure 4.7 Fluorescent response of $H_3\mathbf{L}^{III}$ (20 µM) in the presence of different concentrations (0-200 µM) of spiked Al^{3+} in tap water (a.) and Hawkesbury river water (b.) as well as the fluorescence of the respective water samples with no treatment. The samples were excited at 395 nm and fluorescent intensities were taken at 437 nm.

4.4.2 Cell Viability Assay

A cell viability assay of $H_3\mathbf{L}^{III}$ was carried out using the MTT method at varying concentrations in 1321N1 astrocyte cells which implied the suitability of $H_3\mathbf{L}^{III}$ for biological applications. Results indicated that up to 500 µM, $H_3\mathbf{L}^{III}$ had no effect on cell viability indicating the potential suitability of $H_3\mathbf{L}^{III}$ to sense Al^{3+} in biological systems. Minor variations in cell viability are likely due to varying rates of cell growth and/ or pipetting error (Fig. 4.8).

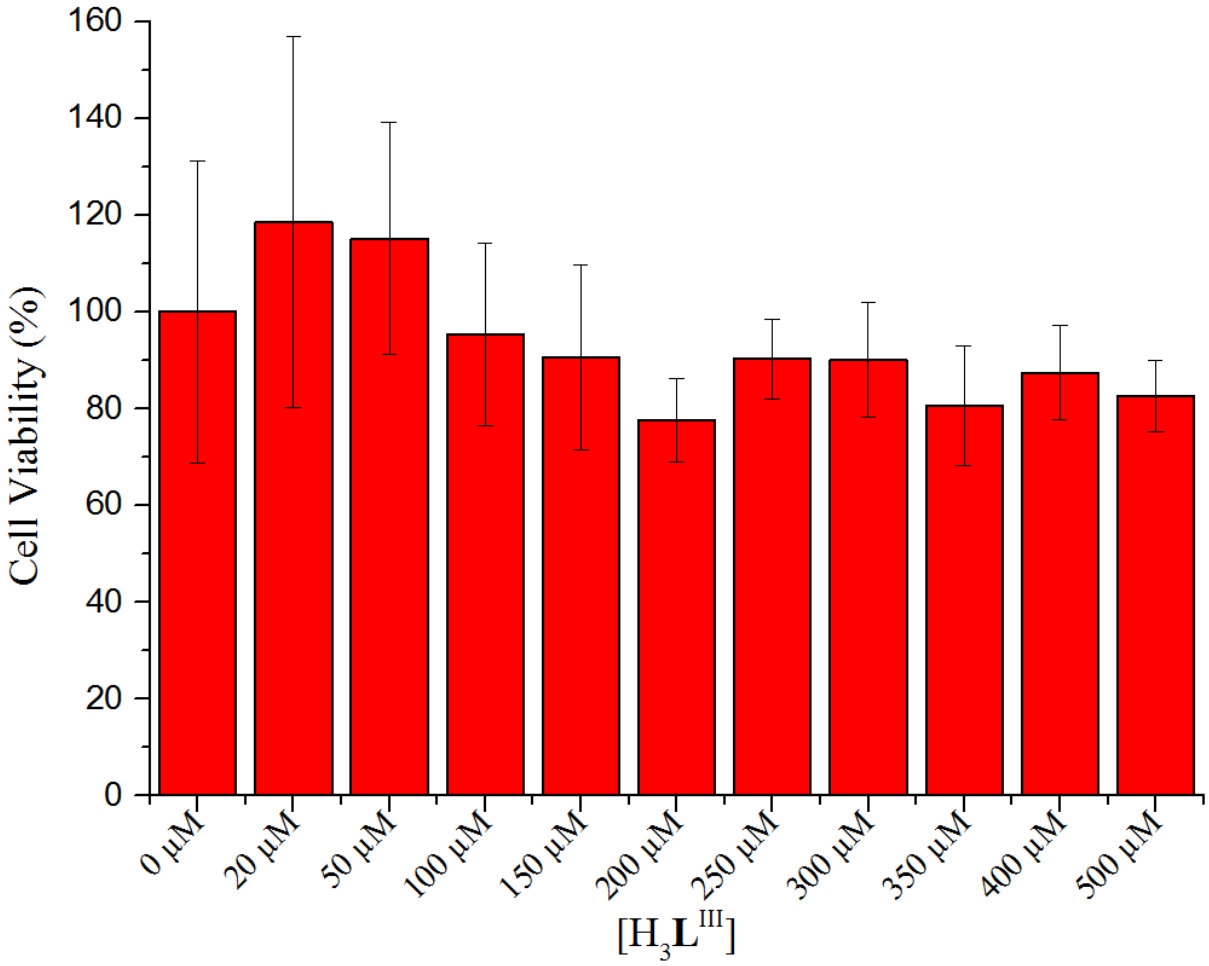

Figure 4.8 Percentage (%) of cell viability of 1321N1 astrocyte cells treated with different concentrations (0–500 µM) of $H_3\mathbf{L}^{III}$ for a 24 h incubation period, determined by an MTT reduction assay. Error bars = STD (n = 5).

4.4.3 Cellular Imaging

Confocal microscopy studies displayed the ability of $H_3\mathbf{L}^{III}$ to detect Al^{3+} in 1321N1 astrocyte cells (Fig. 4.9). Upon addition of $H_3\mathbf{L}^{III}$ (40 µM), fluorescence enhancement occurs within the cell lines. It can be assumed that the binding of Al^{3+} to $H_3\mathbf{L}^{III}$ is inducing such response based upon preliminary *in vitro* experiments. Further, more advanced, experimentation may confirm that no other interaction is inducing a similar fluorescent response upon addition of $H_3\mathbf{L}^{III}$ to 1321N1 cell lines.

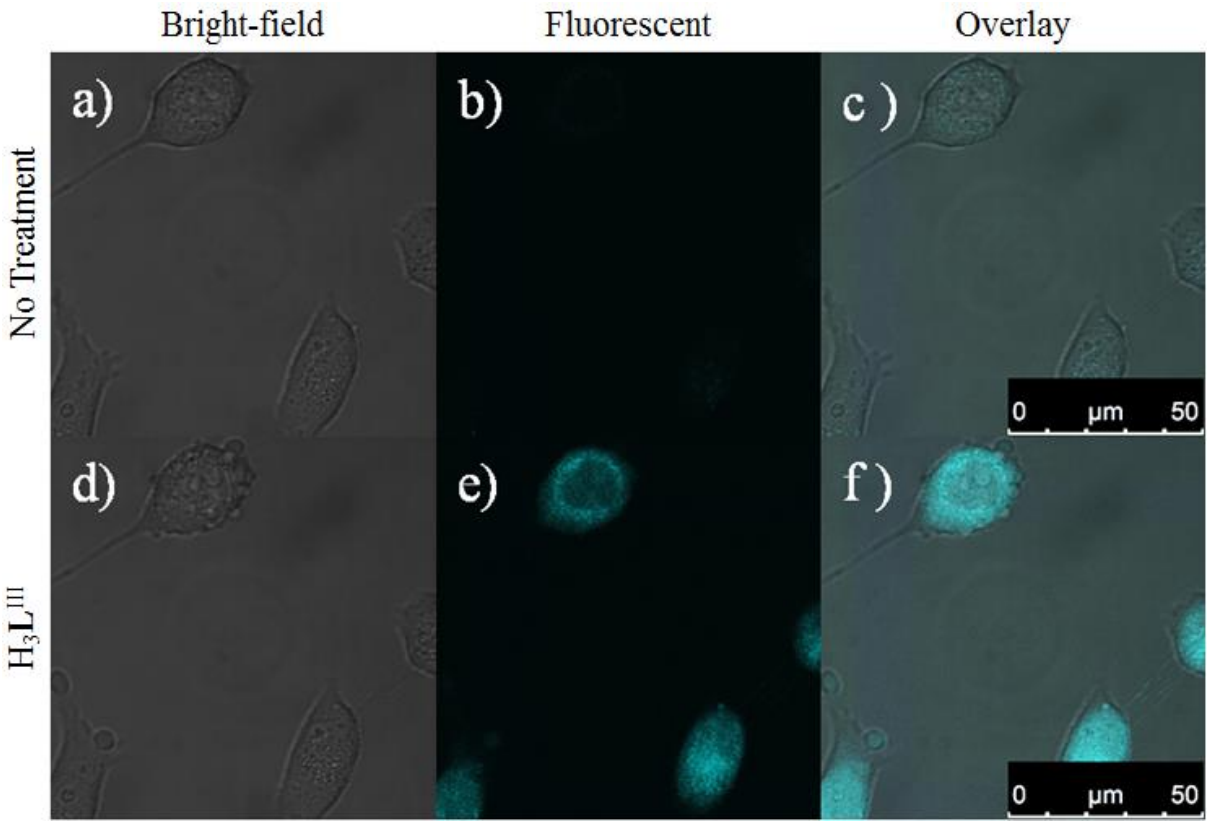

Figure 4.9 Confocal microscope images of 1321N1 astrocyte cells. a), b), c) indicate bright-field, fluorescent and overlay images, respectively, of the cells upon in Phosphate buffered saline (PBS) buffer with no treatment. Images d), e) and f) indicate bright-field, fluorescent and overlay images, respectively, of the cells treated with $H_3\mathbf{L}^{III}$ (40 µM) in PBS buffer. All experiments were conducted under 100 x magnification, excited with a 405 nm laser. Scale bars represent 50 µm.

4.5 Conclusion

$H_3\mathbf{L}^{III}$ was synthesised, characterised and displays a significant, selective, fluorescent enhancement response to Al^{3+} at 437 nm. A stoichiometry of 1:1 ligand-to-metal ratio was indicated using metal titration, Job's plot as well as MS. The affinity of $H_3\mathbf{L}^{III}$ to Al^{3+} was tested in the coexistence of other metals and in different water samples indicating that $H_3\mathbf{L}^{III}$ can sense for Al^{3+} in various environments. Cell viability assays indicate that $H_3\mathbf{L}^{III}$ has no effect on cell viability and thus is suitable for cellular studies. $H_3\mathbf{L}^{III}$ was thereby tested for its potential fluorescent sensing capabilities in cellular conditions, using a confocal microscope. Here, $H_3\mathbf{L}^{III}$ indicated that it can sense intracellular Al^{3+} at low concentration.

$H_3\mathbf{L}^{III}$ appears to, however, be two separate products. This is easily identified in the STA, ^{1}HNMR and ^{13}NMR data. Purification, isolation and identification of the active compound is essential for future research.

4.6 Experimental

4.6.1 Chemicals and Reagents

All chemicals, solvents and cell lines were purchased from commercial sources of commercial grade and used without further purification. All aqueous solutions were prepared with type I water from a Milli-Q water purification system. Metal standards were prepared from chloride (Na^+ , Mg^{2+}, Al^{3+}, K^+ , Ca^{2+}, Cr^{3+}, Mn^{2+}, Fe^{3+}, Co^{2+}, Ni^{2+}, Cu^{2+}, Zn^{2+}, Cd^{2+}, Ba^{2+} and, Hg^{2+}) or nitrate (Pb^{2+}) salts of analytical grade, then standardised using literature complexometric titration methods with H_2Na_2EDTA.[24]

4.6.2 Instrumentations

Characterisation of $H_3\mathbf{L}^{III}$ was carried out using a range of techniques. ^{1}H and ^{13}C NMR spectra were measured on a Bruker DRX-300 NMR spectrometer. FT-IR measurements were conducted on a Bruker Vertex 70 spectrometer. Electrospray ionisation high resolution mass spectra (ESI-HRMS) were collected using a Waters Xevo QToF quadrupole mass spectrometer with samples dissolved in methanol. Simultaneous thermal analysis (STA) was undertaken on a Netzsch STA449 C Jupiter thermo-microbalance. An Edinburgh instruments FS5 Spectrofluorometer was used to conduct all fluorescent measurements. Agilent Cary 100 spectrophotometer was used to conduct the UV-vis experiments. Quartz cuvettes with a 1 cm optical path length were used for all fluorescent and colourmetric experiments. Fluorescent and colourimetric measurements, as well as cell viability assays, were graphed using Origin Pro 9.0. Scanning electron microscopy–electron dispersive spectroscopy (SEM-EDS) analysis was conducted on a Phenom XL instrument. Samples were run at 15 kV at medium vacuum without surface coating.

4.6.3 Synthesis of $H_3\mathbf{L}^{III}$

L-cysteine (440 mg, 3.63 mmol) and 2-hydroxy-1-naphthaldehyde (625 mg, 2.66 mmol) was dissolved in methanol (25 mL) into a conical flask. Five drops of glacial acetic acid then added to the mixture. The mixture was then stirred at room temperature (rt) for 24 h. The precipitate was collected using gravity filtration and washed thoroughly in methanol and then diethyl ether. The precipitate was left to dry overnight resulting was an off-white powder with a yield of ~90%. m.p. 154.3 °C, ^{1}HNMR: (300 MHz, DMSO-d_6 with TMS) δ 7.940-7.083 (m, ArH), δ 6.377 (s, 0.4H, N=CH), δ 4.030 (t, J = 8.22 Hz, 0.8H, SH), δ 3.466 (t, J = 8.2 Hz, 1H, CH), δ 3.171 (m, 0.8H, CH_2). ^{13}CNMR: (75 MHz, DMSO-d_6 with TMS) δ 172.64, δ 154.72, δ 131.93, δ 131.69, δ 129.63, δ 129.63, δ 128.48, δ 127.75, δ 126.63, δ 122.52, δ 121.50, δ 119.29, δ 113.44, δ 112.60, δ 65.5, δ 63.09, δ 37.09, δ 35.33. ESI-HRMS: 276.0577 *m/z* $[H_3\mathbf{L}^{III} + H]^+$. FT-IR: 3675.80 cm^{-1} (O-H, carboxylic acid), 2989.06 cm^{-1} (O-H, phenol), 2900.91 cm^{-1} (S-H), 1635.07 cm^{-1} (O=C, carboxylic acid), 1519.20 cm^{-1} (C=N). UV−vis (1 cm optical path length, Milli-Q H_2O, 5 mM glutathione (GSH), HEPES 20 mM, pH = 7.4): 20 μM $H_3\mathbf{L}^{III}$, λmax = 414 nm (abs = 0.1457, ε = 7 285).

4.6.4 Synthesis of $[Al\mathbf{L}^{III}]$

Potassium hydroxide (44.4 mg, 0.791 mmol) was dissolved in 10 mL methanol. $H_3\mathbf{L}^{III}$ (100 mg, 0.302 mmol) was completely dissolved in the mixture and filtered. The filtrate was then collected and stirred at rt for 5 min. Aluminium chloride (40.3 mg, 0.604 mmol) was dissolved in 10 mL methanol and added dropwise to the mixture. The mixture was then stirred for a further 2 h and filtered. The precipitate was then collected and dried overnight. The result was a yellow powder at ~40% yield. ESI-HRMS: 432.0497 *m/z* $[Al\mathbf{L}^{III}]$ $[Al\mathbf{L}^{III}H_3COH + H]^+$ FT-IR: 3675.79 cm^{-1} (O-H, carboxylic acid), 2969.00 cm^{-1} (O-H, phenol), 2900.90 cm^{-1} (S-H), 1620.07 cm^{-1} (O=C, carboxylic acid), 1543.98 cm^{-1} (C=N).

4.6.5 Fluorescent and UV−Vis Spectroscopy

A stock solution of $H_3\mathbf{L}^{III}$ (2 mM) was prepared in DMSO; this solution was used for all spectroscopic experiments. Metal interaction experiments were carried out by aliquoting appropriate volumes of $H_3\mathbf{L}^{III}$ stock solution to 20 μM and metal ions to 40 μM (2 eq.) in mimicked intracellular conditions of 20 mM glutathione (GSH), 5 mM HEPES buffer at 7.4

pH in Milli-Q water to a total cuvette volume of 3 mL.[25] $AlCl_3$ was added as 2 eq. (40 μM), with competing metal ions also as 2 eq. (40 μM). Job's plot measurements were undertaken based upon literature protocols,[26, 27] where $H_3\mathbf{L}^{III}$ and $AlCl_3$ were prepared in various molar ratios, with the combined concentration of both at 50 μM to a total cuvette volume of 3 mL. These molar ratio mixtures were prepared in a methanol to reduce external interactions with $H_3\mathbf{L}^{III}$ and $AlCl_3$. All fluorescent studies were excited at 395 nm and scanned from 405-700 nm. All fluorescent experiments were prepared ~ 12 h prior to running, where they were stored in a dark, dry environment at standard laboratory conditions. Mimicked intracellular solution studies were performed at slits of ex/em = 5/5 nm, whereas methanolic studies at ex/em = 2/2 nm.

4.6.6 Sensitivity Studies of $H_3\mathbf{L}^{III}$ with Al^{3+}

To determine the sensitivity of $H_3\mathbf{L}^{III}$ to Al^{3+} a metal titration approach was used in methanol, where samples of $H_3\mathbf{L}^{III}$ (20 μM) was prepared with a various equivalents of $AlCl_3$. The samples were left to incubate in a dark, dry environment at standard laboratory conditions for ~ 12 h prior to run time. The limit of detection (LoD) and limit of quantification (LoQ) were calculated using 3σ/m and 10σ/m, respectively, where σ is the standard deviation of a blank solution and m is the slope of the linear plot obtained.[28] For the standard deviation (σ) determination, we took 10 repeated spectra measurements of a blank solution ($H_3\mathbf{L}^{III}$ solution in the same conditions used for measurements but without any addition of $AlCl_3$) and calculated the standard deviation for the fluorescent values at 437 nm, obtaining a value of σ = 90.30311.

4.6.7 Cell Culturing

Human 1321N1 cell line (1321N1 astrocytoma; purchased from Sigma-Aldrich/ ATCC) were grown in Dulbecco's modified eagle medium (DMEM) supplemented with 10% fetal bovine serum (FBS) and antibiotics (penicillin-100 μg ml^{-1}; streptomycin-50 μg ml^{-1}). Cells were cultured at 37 °C in a 95% air, 5% CO_2 incubator.

4.6.8 Cell Viability Assay

1321N1 astrocytoma cells were seeded into a 96-well plate and filled with complete DMEM to a total volume of 195 µL containing 10,000 cells each and then incubated (37 °C, CO_2 5%) for 24 h. Stock solutions of $H_3\mathbf{L}^{III}$ (20 mM, 10 mM, 2.5 mM) were prepared in sterile DMSO. 5 µL of pentet concentration of 0, 20, 50, 100, 150, 200, 300, 350, 400 and 500 µM of $H_3\mathbf{L}^{III}$ were prepared into the 96 well plates and incubated for 24 h. 50 µL of 5 mg/mL 3-(4,5-dimethylthiazol-2-yl)-2,5-diphenyltetrazolium bromide (MTT) was added into each well and the cells were then left to incubate (37 °C, CO_2 5%) for a further 2 h. The media was decanted from each well and 100 µL of DMSO was added into each well to solubilise the formazan crystals. The 96 plate well was gently agitated before optical absorbance was measured at 595 nm using the BMG FLUOstar OPTIMA microplate reader. The values were then calculated as the mean ± standard deviation errors of six independent experiments. The cell viability was expressed as the optical density ratio of the treatment compared to control samples.

4.6.9 Detection of Al^{3+} in Different Water Samples

Tap water sample was taken from Parramatta Council, Sydney, NSW, Australia. Hawkesbury River water samples were collected from still river water samples from Bobbin Head, Hornsby Shire Council, Sydney, NSW, Australia. Blank water samples were initially measured as controls. $H_3\mathbf{L}^{III}$ (20 µM) was added into varying spiked samples of $AlCl_3$ (0, 10, 20, 50, 100 and 200 µM) to a total volume of 3 mL in each of the water samples. All water samples were excited at 395 nm and data was collected at 437 nm with slit sizes of ex/em = 5/5 nm.

4.6.10 Cell Imaging

1321N1 astrocytoma cells were viewed under the Inverted Leica TCS SP5 laser scanning confocal microscope at the confocal bio-imaging facility WSU, with all parameters according to table 4.1. A fluorodish of 1321N1 cells was prepared and incubated (37 °C, CO_2 5%) 24 h prior to experimentation. The cells were then viewed with no added treatment in PBS buffer. $H_3\mathbf{L}^{III}$ (40 µM; in DMSO) was then added to the fluorodish and incubated for 10

min where it was then washed three times with PBS. All images captured were processed using LAS AF software.

Table 4.1 Parameters used for all cell imaging studies of 1321N1 astrocytoma.

Dimension	**Logical Size**	**Physical Length**	**Physical Origin**
X	1024	98.41 µm	0.00 µm
Y	1024	98.41 µm	0.00 µm
LUT Name	**Objective**	**Aperture**	**em Bandwidth**
Laser 405 Diode, UV	HC DL APO C52 63.0x1.20 WATER UV	1.20	458-500 nm

4.7 Acknowledgments

The authors thank the Western Sydney University (WSU) Advance Material Characterisation Facility and the WSU Mass Spectrometry Facility for instrumental access. Acknowledgments also go to the Confocal Bio-imaging facility at WSU for the use of their confocal microscope. D.J.W. also thanks WSU for their postgraduate research funding.

4.8 Conflicts of Interest

There are no conflicts to declare.

4.9 Reference List

1. K. Mal *et al.* Dihydroindeno[1,2-b]pyrroles: new Al3+ selective off–on chemosensors for bio-imaging in living HepG2 cells. *Org Biomol Chem* **16,** 5920–5931 (2018).
2. C. Exley. A biogeochemical cycle for aluminium? *J. Inorg. Biochem.* **97,** Journal of Inorganic Biochemistry (2003).
3. K. Tennakone, S. Wickramanayake & C. A. N. Fernando. Aluminium contamination from fluoride assisted dissolution of metallic aluminium. *Environ. Pollut.* **49,** 133–143 (1988).
4. X. Shi-Gang, S. Li-Xin, Z. Rong-Gen & H. Xing-Fang. Properties of aluminium oxide coating on aluminium alloy produced by micro-arc oxidation. *Surf. Coat. Technol.* **199,** 184–188 (2005).
5. K. R. Koch, M. A. Pougnet, S. de Villiers & F. Monteagudo. Increased urinary excretion of Al after drinking tea. *Nature* **12,** 122 (1988).
6. B. O. Rosseland, T. D. Eldhuset & M. Staurnes. Environmental effects of aluminium. *Environ. Geochem. Health* **12,** 17–27 (1990).
7. S. J. Zheng. Crop production on acidic soils: overcoming aluminium toxicity and phosphorus deficiency. *Ann. Bot.* **106,** 183–184 (2010).
8. S. J. Carr, G. S. P. Ritchie & W. M. Porter. A soil test for aluminium toxicity in acidic subsoils of yellow earths in Western Australia. *Aust. J. Agric. Res.* **42,** 875–892 (1991).
9. V. B. Gupta *et al.* Aluminium in Alzheimer's disease: are we still at a crossroad? *Cell. Mol. Life Sci.* **62,** 143–158 (2005).
10. A. Campbell. The potential role of aluminium in Alzheimer's disease. *Nephrol. Dial. Transplant.* **17,** 17–20 (2002).
11. J. P. Landsberg, B. McDonald & F. Watt. Absence of aluminium in neuritic plaque cores in Alzheimer's disease. *Nature* **360,** 65–68 (1992).
12. T. P. Flaten. Aluminium as a risk factor in Alzheimer's disease, with emphasis on drinking water. *Brain Res. Bull.* **55,** 187–196 (2001).
13. S. Kim *et al.* Salicylimine-Based Fluorescent Chemosensor for Aluminum Ions and Application to Bioimaging. *Inorg. Chem.* **51**, 3597–3602 (2012).
14. D. Maity & T. Govindaraju. Naphthaldehyde–Urea/Thiourea Conjugates as Turn-On Fluorescent Probes for Al3+ Based on Restricted C=N Isomerization. *Eur. J. Inorg. Chem.* **2011**, 5479–5485 (2011).
15. N. M. Giles *et al.* Metal and Redox Modulation Review of Cysteine Protein Function. *Chemistry and Biology* **10**, 677–693 (2003).
16. N. J. Pace & E. Weerapana. Zinc-Binding Cysteines: Diverse Functions and Structural Motifs. *Biomolecules* **4**, 419–434 (2013).
17. R. Spezia, G. Tournois, T. Cartailler, J. Tortajada & Y. Jeanvoine. Co2+ Binding Cysteine and Selenocysteine: A DFT Study. *J. Phys. Chem. A.* **110**, (2006).
18. R. B. Singh, S. Mahanta, S. Kar & N. Guchhait. Photo-physical properties of 1-hydroxy-2-naphthaldehyde: A combined fluorescence spectroscopy and quantum chemical calculations. *Chemical Physics* **331**, 373–384 (2007).
19. J.-C. Qin, X.-Y. Cheng, R. Fang, M.-F. Wang, Z.-Y. Yang, T.-R. Li, et al. Two Schiff base fluorescent sensors for selective sensing of aluminum (III): Experimental and computational studies. *Spectrochim. Acta, Part A.* **2016**;152:352–7.
20. D. Escudero. Revising Intramolecular Photoinduced Electron Transfer (PET) from First-Principles. *Acc Chem Res* **49,** 1816−1824 (2016).
21. L. D. Lavis & R. T. Raines. Bright Ideas for Chemical Biology. *ACS Chem Biol* **3,** 142–155 (2018).
22. D. Escudero. Revising Intramolecular Photoinduced Electron Transfer (PET) from First-Principles. *Acc Chem Res* **49,** 1816−1824 (2016).

23. L. D. Lavis & R. T. Raines. Bright Ideas for Chemical Biology. *ACS Chem Biol* **3,** 142–155 (2018).
24. G. Schwarzenbach & H. Flaschka. *Complexometric Titrations*. (H. M. N. H, 1969).
25. H. Y. Au-Yeung, E. J. New & C. J. Chang. A selective reaction-based fluorescent probe for detecting cobalt in living cells. *Chem. Commun.* **48**, 5268–5270 (2012).
26. P. Job. Formation and Stability of Inorganic Complexes in Solution. *Ann. Chim.* **9**, (1928).
27. J. S. Renny, L. L. Tomasevich, E. H. Tallmadge & D. B. Collum. Applications of Job Plots to the Study of Molecular Associations in Organometallic Chemistry. *Angew. Chem., Int. Ed.* **52**, 11998−12013 (2013).
28. B. Magnusson. The Fitness for Purpose of Analytical Methods: A Laboratory Guide to Method Validation and Related Topics; Eurachem, 2014. in (Eurachem, 2014).

4.10 Supplementary Information

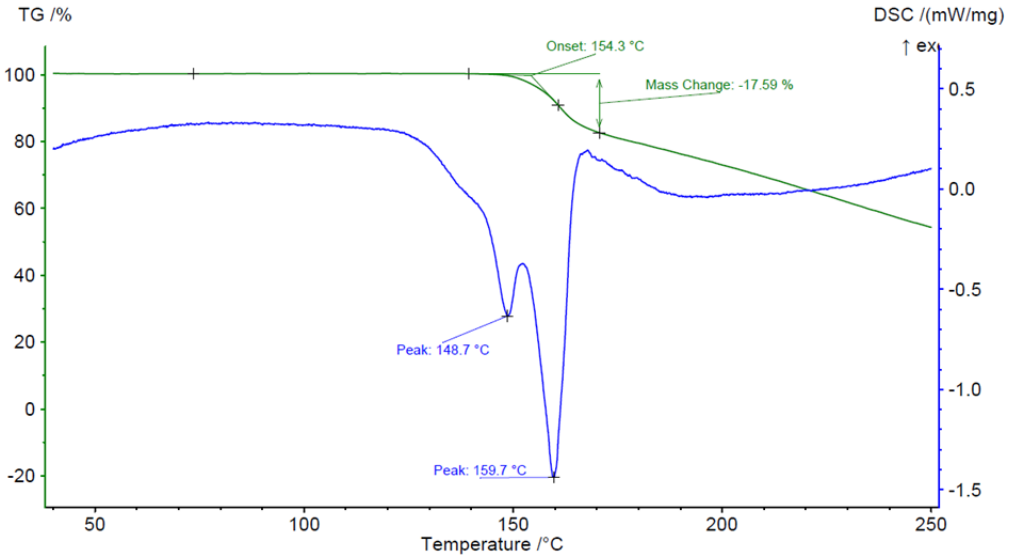

Figure S4.1 The STA data of $H_3\mathbf{L}^{III}$ (40-250 °C).

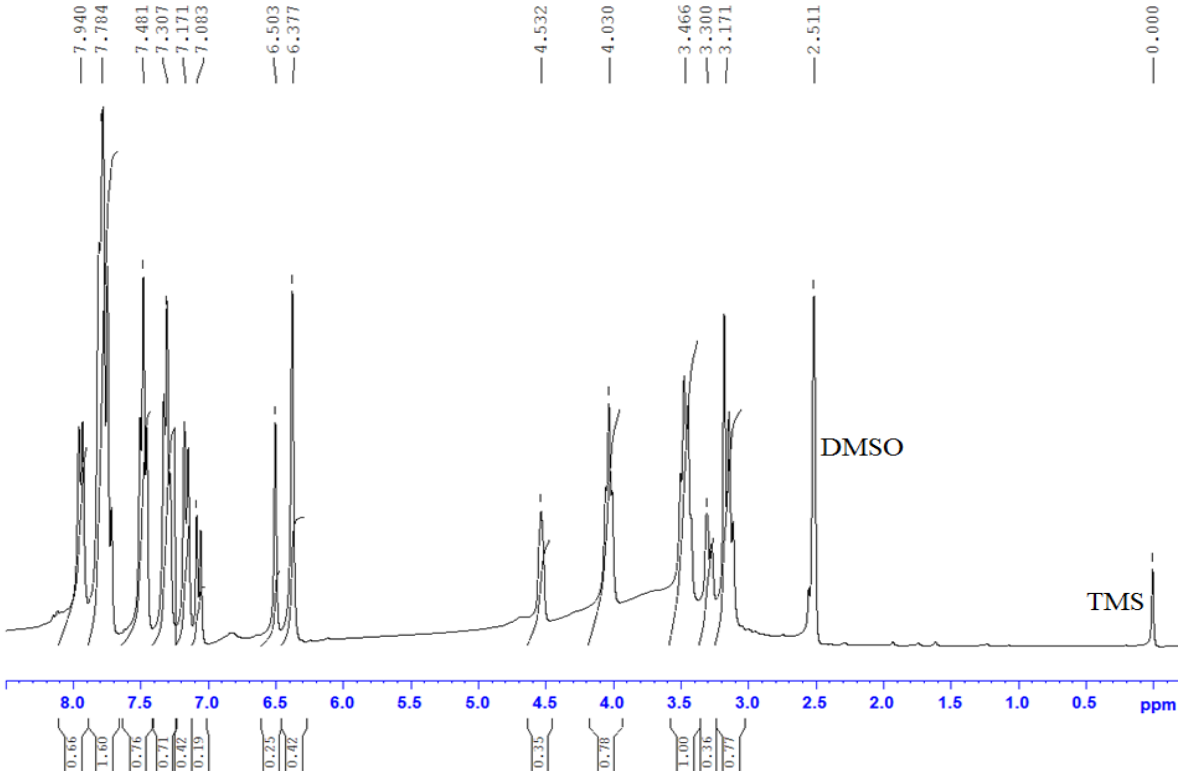

Figure S4.2 The ^{1}HNMR spectrum of $H_3\mathbf{L}^{III}$ in DMSO-d_6**.**

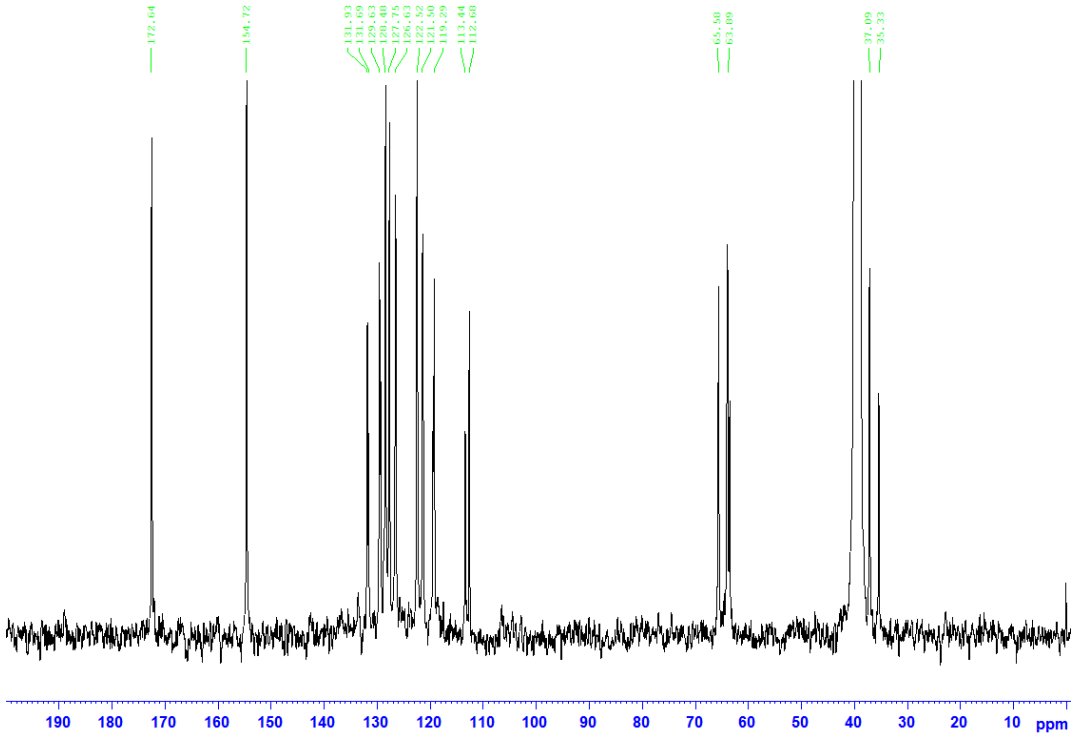

Figure S4.3 The ^{13}CNMR spectrum of $H_3\mathbf{L}^{III}$ in DMSO-d_6

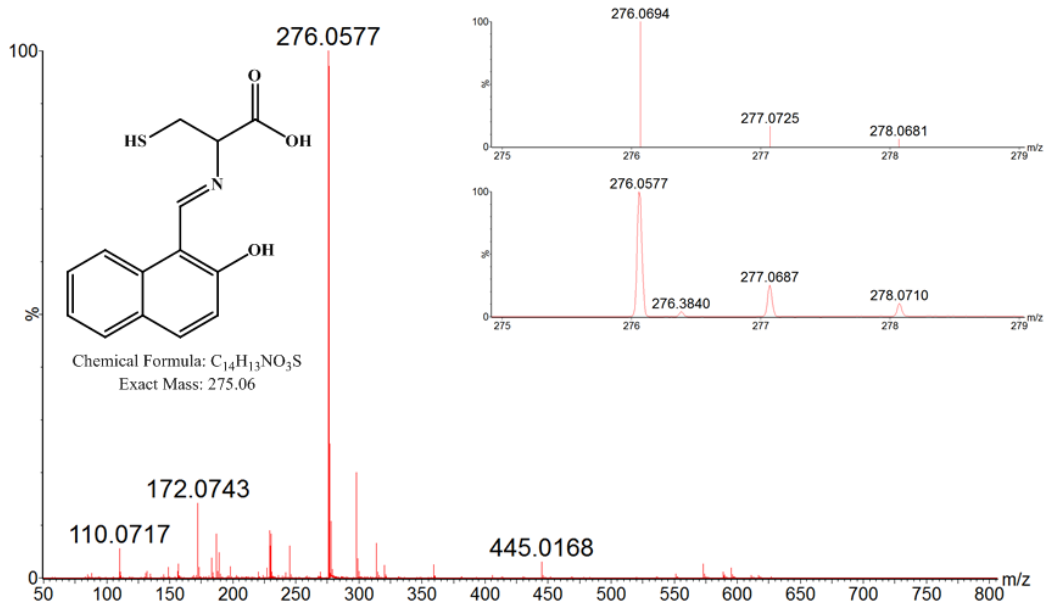

Figure S4.4 ESI-HRMS of $H_3\mathbf{L}^{III}$;$[H_3\mathbf{L}^{III} + H]^+$ in methanol from 50 – 800 *m/z*. Inset: On the left, the structure and molar mass of $H_3\mathbf{L}^{III}$. On the right, the predicted (above) and experimental (bellow) isotopic patterns of $[H_3\mathbf{L}^{III} + H]^+$.

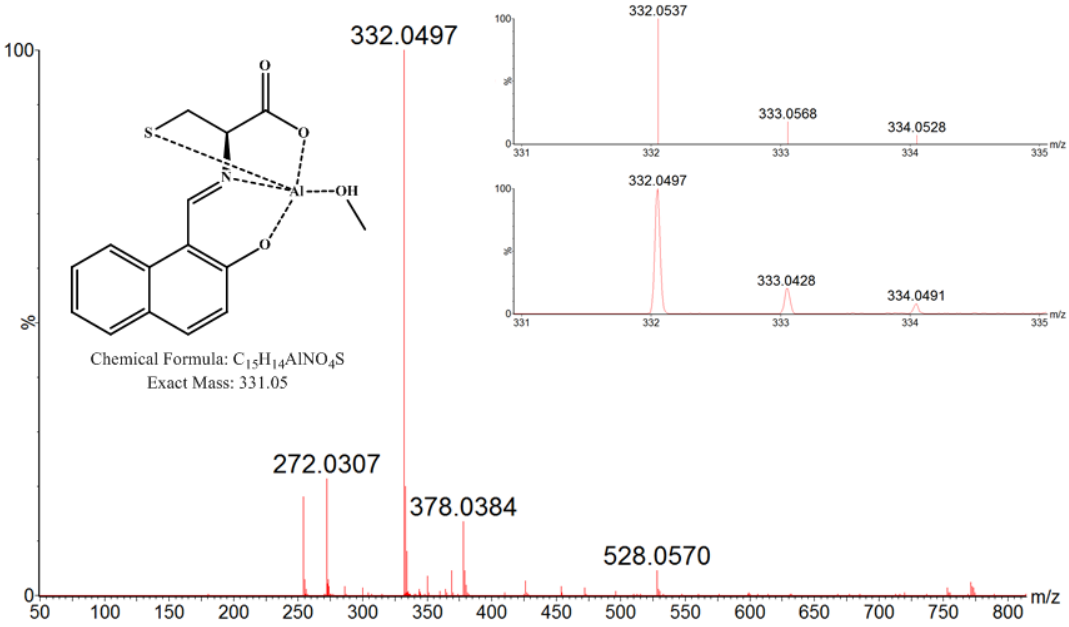

Figure S4.5 ESI-HRMS of $[Al\mathbf{L}^{III}]$ $[Al\mathbf{L}^{III}H_3COH + H]^+$ in methanol from 50 – 800 *m/z*. Inset: On the left, the predicted structure and molar mass of $[Al\mathbf{L}^{III}H_3COH]$. On the right, the predicted (above) and experimental (bellow) isotopic patterns of $[Al\mathbf{L}^{III}H_3COH+ H]^+$.

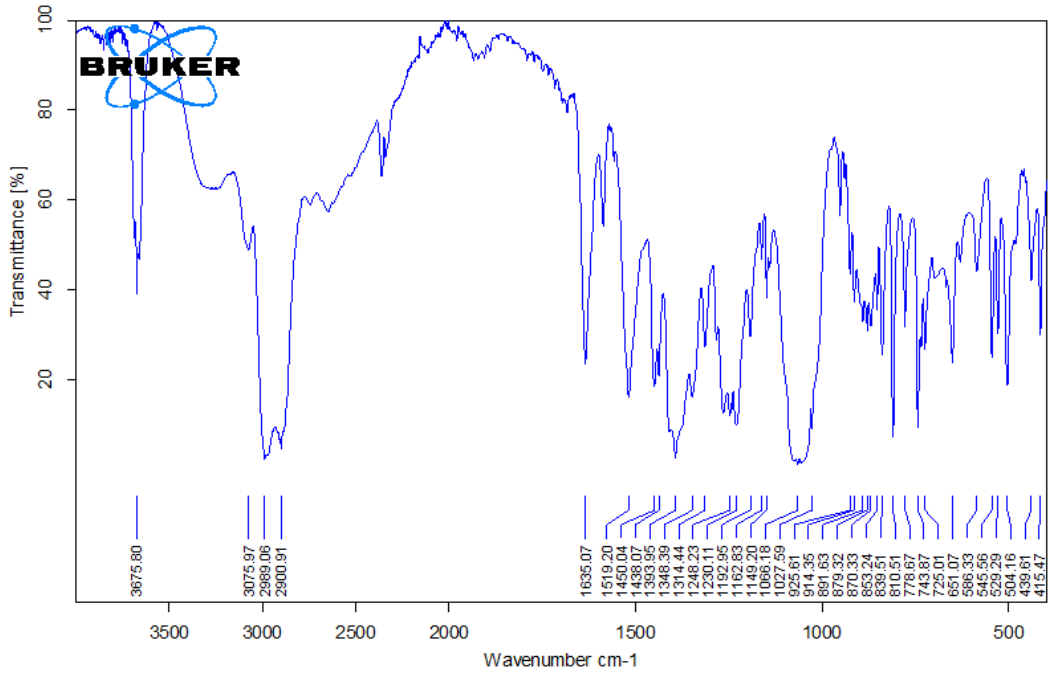

Figure S4.6 FT-IR spectrum of $H_3\mathbf{L}^{III}$.

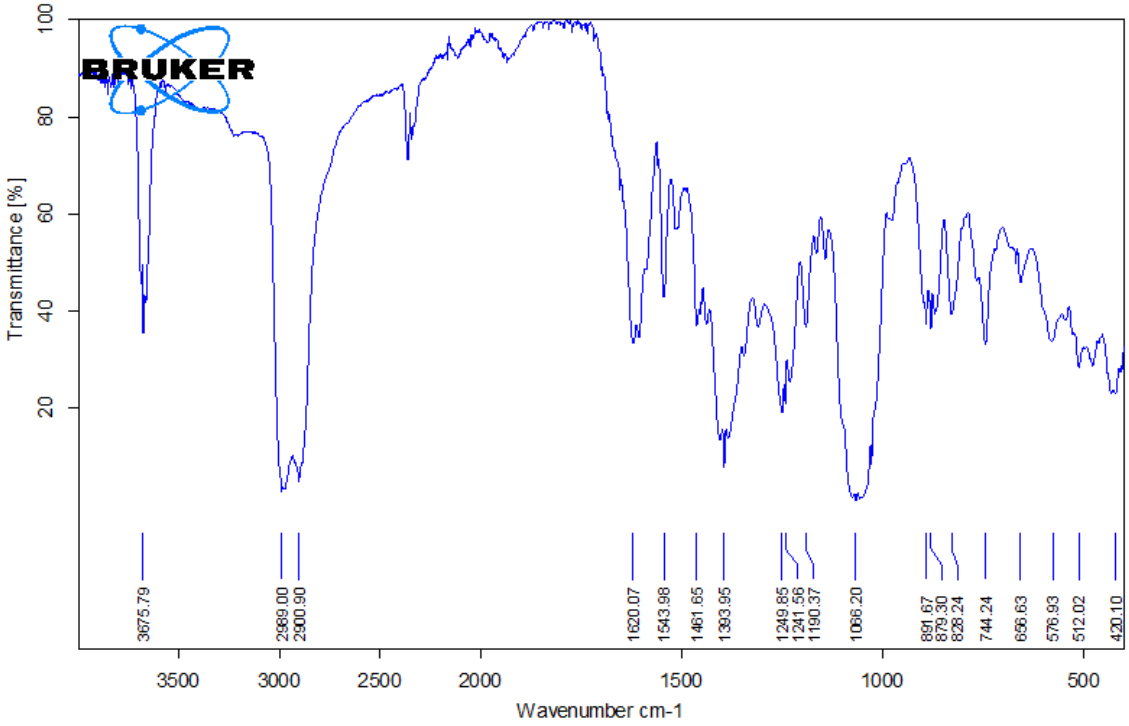

Figure S4.7 FT-IR spectrum of [Al$\mathbf{L}^{III}$].

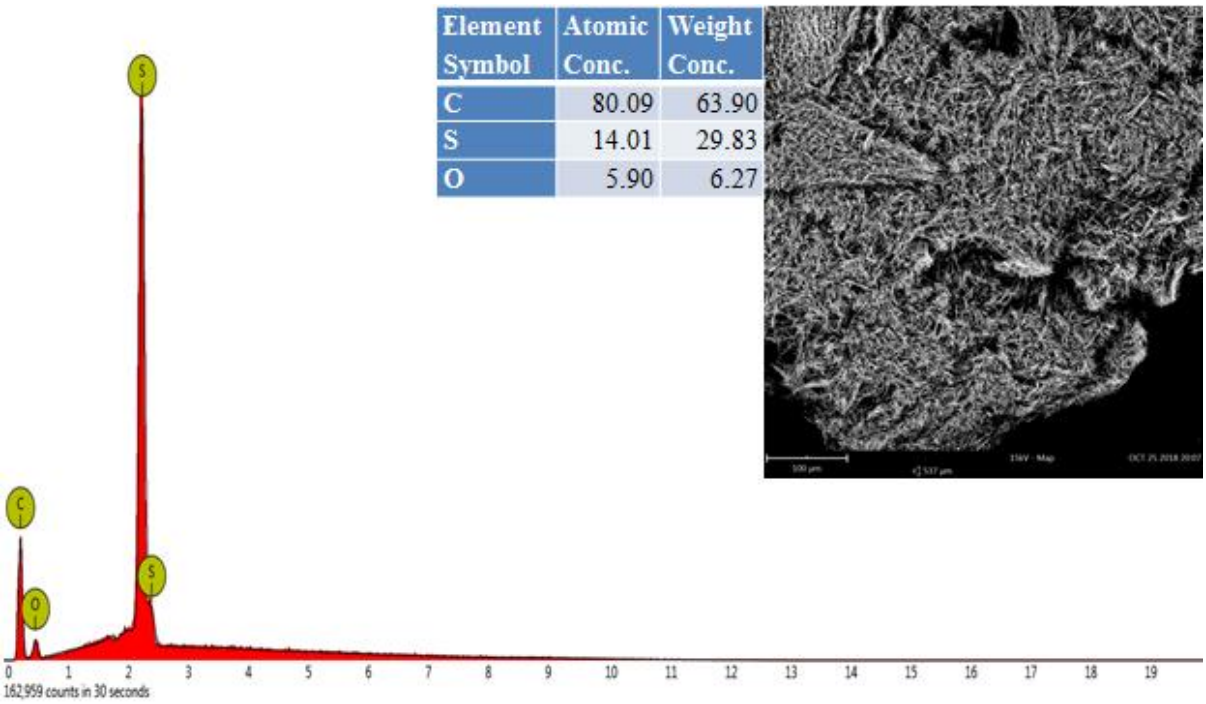

Figure S4.8 EDS spectrum of $H_3\mathbf{L}^{III}$. Inset: At the top, the elemental composition of $H_3\mathbf{L}^{III}$ and on the right, backscattered SEM micrograph of $H_3\mathbf{L}^{III}$ at 500 x magnification.

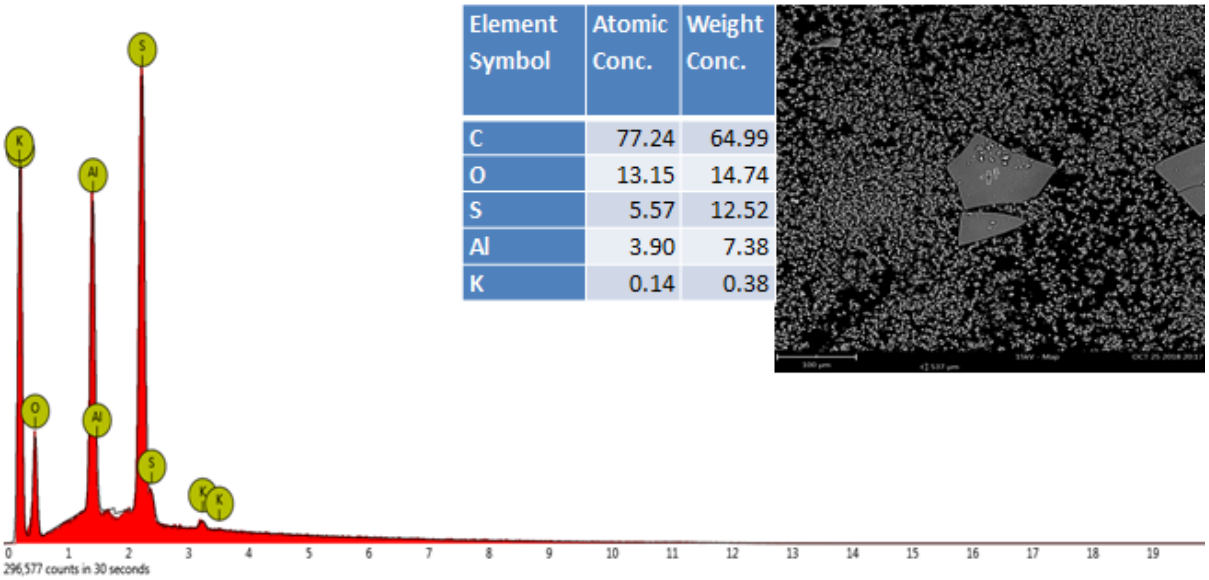

Figure S4.9 EDS spectrum of [Al$\mathbf{L}^{III}$]. Inset: At the top, the elemental composition of [Al$\mathbf{L}^{III}$] and on the right, backscattered SEM micrograph of [Al$\mathbf{L}^{III}$] at 500 x magnification.

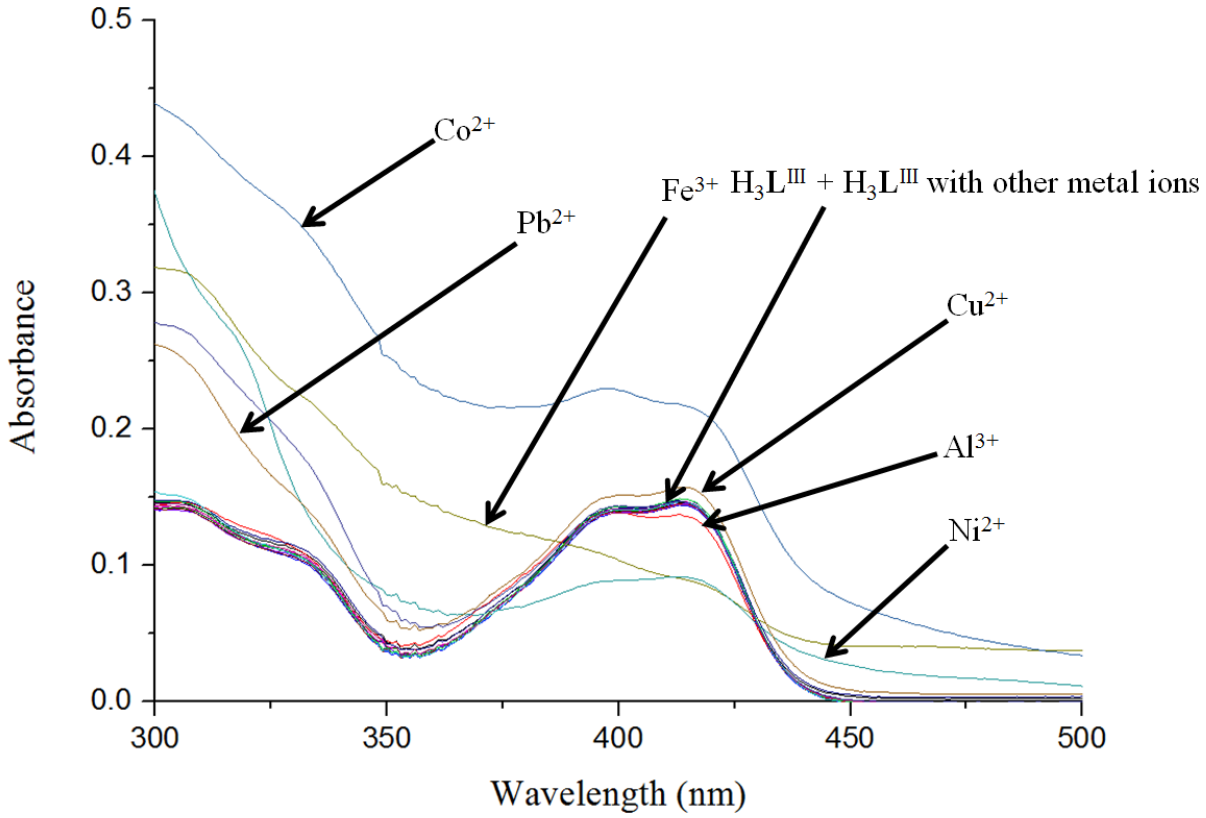

Figure S4.10 The UV-vis spectrum (300-500 nm) of the metal scan of $H_3\mathbf{L}^{III}$ and $H_3\mathbf{L}^{III}$ in the presence of various metal ions.

Chapter 5 – Conclusion and Future Work

5.1 Conclusion

Within this thesis report, three amino acid-derived Schiff base ligands were designed and synthesised. An array of characterisation techniques were employed such as ^{1}HNMR, ^{13}CNMR, FT-IR, HR MS-ESI, SEM-EDS, STA, P-XRD and SC-XRD upon the ligands and their respective metal complexes. Spectral analysis was conducted using a UV-vis and fluorescent spectrofluorometer to evaluate the metal binding affinity and examine the potential role of the three Schiff bases as chemosensors for metal ions. Cell viability assays determined the biocompatibility of the molecules. Fluorescent microscopy, as well as water sample studies, were conducted upon the Schiff bases that exhibited no effects on cell viability. This demonstrated the ability of the Schiff bases to selectively detect their desired metal analyte within biological and aqueous environments. Molecules deemed cytotoxic were coordinated to lanthanide ions (Eu^{3+}, Gd^{3+}, Dy^{3+}) and analysed using spectral DNA binding studies, as well as cell viability assays, on myoblast, astrocytoma and carcinoma cell lines. Two fluorescent Al^{3+} sensors and four anticancer agents resulted from these studies as well as an enhanced knowledge of the roles of lanthanide complexes as potential anticancer agents.

In regards to chapter 1, an introduction was given which orchestrated the general concepts of supramolecular, bioinorganic, and fluorescent chemistry. Guidelines for designing ideal fluorescent sensors were evaluated and the general aims and scope of the thesis report were projected.

Concerning chapter 2, an ideal fluorescent sensor ($H_2\mathbf{L}^{I}$) for Al^{3+} was successfully designed and synthesised from the Schiff base condensation reaction between L-tryptophan and 4-diethylamino salicylaldehyde. Spectral analysis explored the metal binding properties of $H_2\mathbf{L}^{I}$ with an array of metal ion. The results indicated a blue-shift; 24-fold fluorescent enhancement of $H_2\mathbf{L}^{I}$, selective for Al^{3+}. Its binding affinity for Al^{3+} was strong enough to evoke a detectable fluorescent response, in the presence of other competing metal ions. Limited detection analysis determined a LoD of 61.5 nM and the ligand-to-metal stoichiometry was determined as 1:2, which supported the data indicated by a Job's plot and MS. Cell viability assays determined that $H_2\mathbf{L}^{I}$ had no effect on cell viability. $H_2\mathbf{L}^{I}$ was then

able to detect Al^{3+} within AD relevant, 1321N1 astrocytoma cells. $H_2\mathbf{L}^{I}$ was compared to a vast array of recent Al^{3+} fluorescent sensors, presenting its superiority, in particularly, for biological studies. $H_2\mathbf{L}^{I}$ is therefore appropriate to be used as a fluorescence sensor in different aqueous and cellular environments.

Within chapter 3, the Schiff base ligand ($H_3\mathbf{L}^{II}$) was successfully designed, synthesised and characterised. $H_3\mathbf{L}^{II}$ displayed some potential as a selective Zn^{2+} fluorescent chemosensory, however, was toxic towards specific cell lines. $H_3\mathbf{L}^{II}$ was therefore coordinated to lanthanides and its complexes ($[Eu\mathbf{L}^{II}_2]^{3-}$, $[Gd\mathbf{L}^{II}_2]^{3-}$, and $[Dy\mathbf{L}^{II}_2]^{3-}$) were characterised. In 1321N1 astrocytoma cells, the lanthanide complexes exhibited lower EC_{50} 67.5%, 51.5% and 47.9% for $[Eu\mathbf{L}^{II}_2]^{3-}$, $[Gd\mathbf{L}^{II}_2]^{3-}$, and $[Dy\mathbf{L}^{II}_2]^{3-}$ respectively, in regards to $H_3\mathbf{L}^{II}$. Coordinated lanthanides had little effect upon the cell viability of $H_3\mathbf{L}^{II}$ within L6 myoblast cells. In A2780 carcinoma cells, $H_3\mathbf{L}^{II}$ and its lanthanide complexes displayed EC_{50} values of 12.96 µM, 12.41 µM, 14.06 µM and 6.998 µM for $H_3\mathbf{L}^{II}$, $[Eu\mathbf{L}^{II}_2]^{3-}$, $[Gd\mathbf{L}^{II}_2]^{3-}$, and $[Dy\mathbf{L}^{II}_2]^{3-}$ respectively. This was significantly less than cisplatin and so DNA binding studies were conducted using spectral methods to determine the possible mechanism of $H_3\mathbf{L}^{II}$ and its complexes for inducing low EC values. $H_3\mathbf{L}^{II}$ and its lanthanide complexes were, therefore, determined to be potentially used as anticancer agents specific to ovarian carcinomas. Additionally, upon complexation, lanthanides enhanced cell toxicity specifically towards neuronal cells.

Lastly, in chapter 4, an Al^{3+} fluorescent sensor ($H_3\mathbf{L}^{III}$) was synthesised and characterised. Fluorescent spectroscopy established that the binding of Al^{3+} to $H_3\mathbf{L}^{III}$ induces a 17-fold fluorescent enhancement response, which was not significantly deterred in the coexistence of other metal ions. The LoD of $H_3\mathbf{L}^{III}$ was determined to be an exceptionally low 3.46 nM and the ligand-to-metal stoichiometry was determined as 1:1. $H_3\mathbf{L}^{III}$ displayed no effect on cell viability. Confocal microscopy displayed the ability of $H_3\mathbf{L}^{III}$ to fluorescently sense Al^{3+} without any additional treatment of Al^{3+}. $H_3\mathbf{L}^{III}$ was determined to be an appropriate Al^{3+} sensor; however, its synthesis yielded two products.

5.2 Future Research

To expand upon chapter 2, the development of fluorescent sensors that are selective to

different cations including Fe^{2+}, Fe^{3+}, Cu^{+}, Cu^{2+}, Zn^{2+}, Hg^{2+} and even anions such as CN^{-} (most of which are intriguing due to their effects upon neurodegeneration) can be designed.[1-4] The development of sensors with fluorophores such as coumarin, fluorescein and naphthalimide, can be designed as these fluorophores exhibit ratiometric responses inducted by FRET and emit at low energy wavelengths.[5-7] Both characteristics are ideal for fluorescent imaging in cellular environments. Quantum yield experiments may also assist with determining the effectivity of such ion chemosensors.

To develop chapter 3 to a publishable state, $H_3\mathbf{L}^{II}$ can be coordinated to form platinum and ruthenium complexes and observed for the effects on cell viability comparatively to that of the lanthanide complexes. These molecules may then undergo further characterisation using circular dichroism (CD) and gel electrophoresis, to enhance the understanding of the mechanism in which these potential anticancer drugs function.

In chapter 4, further isolation (using chromatography) and characterisation of the active molecule is required to evaluate the possible real-world use of $H_3\mathbf{L}^{III}$ as an Al^{3+} fluorescent sensor. Once isolated, the active molecule will be re-examined for its metal binding and fluorescent characteristics to potentially be applied as a fluorescent sensor in aqueous and biological environments.

5.3 Reference List

1. F. Zahir, S. J. Rizwi, S. K. Haq & R. H. Khan. Low dose mercury toxicity and human health. *Environmental Toxicology and Pharmacology* **20**, 351–360 (2005).
2. W.-J. Huang, X. Zhang & W.-W. Chen. Role of oxidative stress in Alzheimer's disease (Review). *Biomed. Rep.* **4,** 519–522 (2016).
3. A. S. Prasad. *Biochemistry of Zinc*. (Springer Science & Business Media, 2013).
4. M. P. Cuajungco & G. J. Lees. Zinc Metabolism in the Brain: Relevance to Human Neurodegenerative Disorders. *Neurobiol. Dis.* **4,** 137–169 (1997).
5. R. Parkesh, T. C. Lee & T. Gunnlaugsson. Highly selective 4-amino-1,8-naphthalimide based fluorescent photoinduced electron transfer (PET) chemosensors for Zn(II) under physiological pH conditions. *Org. Biomol. Chem.* **5**, 310–317 (2007).
6. X. Zhou *et al.* An FRET-based ratiometric chemosensor for in vitro cellular fluorescence analyses of pH. *Biomaterials* **33**, 171–180 (2012).
7. J.-S. Wu *et al.* Fluorescence Turn On of Coumarin Derivatives by Metal Cations: A New Signaling Mechanism Based on C=N Isomerization. *Org. Lett.* **9**, 33–36 (2007).